A Quantum Repeater Sandbox with Warm Atomic Memories and Quantum Dot Photon Sources

by

Michael Li

A thesis
presented to the University of Waterloo
in fulfillment of the
thesis requirement for the degree of
Master of Applied Science
in
Electrical and Computer Engineering (Quantum Information)

Waterloo, Ontario, Canada, 2024

© Michael Li 2024

Author's Declaration

This thesis consists of material all of which I authored or co-authored: see Statement of Contributions included in the thesis. This is a true copy of the thesis, including any required final revisions, as accepted by my examiners.

I understand that my thesis may be made electronically available to the public.

Statement of Contributions

I am the sole author of all the chapters in this thesis, although the conducted experiments and results would not have been possible without the effort and guidance of various members of the Nano-Photonics and Quantum Optics Group. The results of Chapters 3 and 5 were not written for publication, however samples of Chapters 2 and 4 were published in the SPIE conference proceedings for Photonics North 2023 and Photonics West 2024 respectively.

In Chapter 2, I received this project at the start of my degree as it was nearing its first prototype stage. The concept of the digital EOM bias modulator was first proposed by Paul Anderson, and the first PCB was designed by Kassandra Hawes. The pico-second pulse generator was created with the help of Roberto Romero. My responsibilities included soldering the PCB, debugging, programming the bias controller and implementing it for the EOMs in our lab. I was also responsible for testing the picosecond-pulse generator and characterizing the quantum dot (QD) source when excited by the newly stabilized EOM and pico-pulse generator. The QD setup and spectrometer were built by Rubayet Al Maruf and former students before I arrived. The nanowire QDs were fabricated by Philip J. Poole and Dan Dalacu from the National Research Council.

In Chapter 3, the setup and technique of gas deposition were developed by Rubayet. I was responsible for conducting the analysis of the data from measurements of the fine structure splitting. This included performing the gas deposition and measuring the fine structure splitting at various stages of gas deposition and polarization. The script for post analysis and plotting were written by Rubayet.

Chapter 4 does not describe the first implementation of a DAVLL in our lab; many alumni and existing members have already built free-space setups. However, I independently designed and set up the miniaturized 3D-printed opto-mechanical mount, with guidance and suggestions from senior members of the lab such as Katie McDonnell, Paul Anderson, Sai Sreesh Venuturumilli, and Nikolay Videnov.

In Chapter 5, The measurements and setup for the warm cell memory were accomplished by myself; however, I must again appreciate and acknowledge the support I received from fellow lab members. Our co-op student Dejan Latkovic made the heater for the etalon, and Corey Mullin helped make the magnetically shielded oven. Sai Sreesh Venuturumilli, Paul Anderson, and Pratik Adhikary provided many meaningful insights and discussions on how to improve the setup.

Abstract

Quantum communication is known to offer many advantages, including opportunities for distributed quantum computing and more secure information transfer through quantum key distribution. This thesis provides background on how a quantum communication network can be achieved using quantum repeaters and how these components can be constructed with a hybrid system involving a quantum dot source and warm atomic memory. It also presents three experimental projects to realize critical components to the repeater: (1) The quantum dot photon source characterizations and tuning. (2) A compact 3D printed opto-mechanical laser locking board. (3) Optical memory observed in room temperature Cs vapor cells with an EIT memory scheme. These projects have built the basic foundation to create a repeater node using room temperature vapor cells and open the doors to future investigations of warm cell experiments.

Acknowledgements

First, I'd like to thank my supervisor, Prof. Michal Bajcsy, who has supported and mentored my professional development since my undergraduate studies. I appreciate the numerous learning opportunities and insightful conversations that were made possible by the chance to work in his research lab. I'd also like to extend my gratitude to Prof. Michael Reimer and Prof. Simar Saini for their efforts in evaluating my thesis.

I would like to express my gratitude to all the members of the Nano-Photonic and Quantum Optics lab who have imparted practical lab skills and the insights of a graduate student throughout my degree. I am especially grateful to Sai Sreesh Venuturumilli, Dr. Paul Anderson, Dr. Rubayet Al Maruf, Dr. Katie Mcdonnell, Dr. Pratik Adhikary and Nikolay Videnov for their patience in training me and for sharing their profound knowledge in various aspects of the quantum repeater project. Without their guidance, the projects accomplished in this thesis wouldn't have been possible. I also extend my thanks to the co-op students, Jackie Treacy, Dejan Latkovic and Corey Mullin. Their efforts have certainly lightened my load, especially with tasks related to the electro-optic modulator bias controller and etalon filters.

I must also express my appreciation and love for my family members, who have always supported me and hoped for the best in my education. To my sister, thank you for gifting me a 3D printer for my birthday, which has made contributions to the various projects in our lab. And most importantly, thank you for always being my role model and pushing me to become the best version of myself. I would also like to thank my dog, Moji, for offering me the most unconditional love during some of the most challenging times.

Table of Contents

Author's Declaration ii

Statement of Contributions iii

Abstract iv

Acknowledgements v

List of Figures ix

List of Tables xviii

1 Introduction 1

1.1 The Quantum Repeater 2

1.1.1 Quantum Repeater Hardware 4

1.1.2 The Hybrid Quantum Repeater 10

1.2 Electromagnetically Induced Transparency 11

1.2.1 The Dark State 11

1.2.2 The Transparency Window and Slow Light 14

2 QD Photon Source 18

2.1 Nanowire QDs 18

2.1.1 Excitation Protocols . . . 20
2.1.2 Gas Tuning . . . 22
2.2 QD Experimental Setup . . . 23
2.3 Excitation Pulse Generation . . . 25
2.3.1 The Digital Bias Controller . . . 28
2.3.2 The Picosecond Pulse Generator . . . 31
2.4 Results . . . 32

3 Measurements of Fine Structure Splitting in Nanowire Quantum Dots 35
3.1 Fine Structure Splitting . . . 35
3.2 FSS Measurement of 16 QDs . . . 36

4 Miniaturized Laser Locking 43
4.1 Principle and Design . . . 45
4.2 Lock Stability . . . 46
4.3 Conclusion . . . 48

5 Warm Atomic Memory 51
5.1 EIT Memory Protocol . . . 52
5.2 Experimental Setup for EIT Memory . . . 52
5.2.1 Magnetically Shielded Oven . . . 54
5.3 EIT Linewidth . . . 55
5.4 Storage Time . . . 56
5.5 Memory Efficiency . . . 58
5.6 Summary of EIT Memory Results . . . 61
5.7 Further Experiments with Warm Atoms . . . 61
5.7.1 EIT-based single-photon generation . . . 62
5.7.2 Lasing without inversion . . . 63

6 Conclusion **64**

References **66**

APPENDICES **75**

A Gas Tuning **76**

A.1 Gas tuning procedure 77

B EOM Bias Controller Circuit and Code **78**

B.1 The Bias Controller Circuit 78

B.1.1 Symmetry Testing 78

B.1.2 The Arduino and DAC Circuit 79

B.1.3 The Enclosure 80

B.2 Arduino Control Code 82

C Picosecond Pulse Generator **86**

D Fine Structure Splitting Data of 16 Quantum Dots **89**

E DAVLL Push-fit Baord Design **93**

E.1 DAVLL Board CAD Drawings 93

E.1.1 Push-fit Slots 97

E.2 Beam Focusing 97

F Filters for Cs Hyperfine Transitions **99**

List of Figures

1.1 Example of a quantum repeater network to extend entanglement to end points Alice and Bob. 3

1.2 Examples of BSM setups using linear optics. The projected Bell states depend on which detectors click. a) BSM for polarization encoded qubits. H and V indicate the detector responsive to horizontal and vertical polarizations. b) BSM for Fock-encoded qubits. 4

1.3 (a) The Hanbury-Brown-Twiss setup to measure $g^{(2)}(\tau)$: the second-order correlation function. Photons from the source are sent to a 50:50 beam splitter. After the beam splitter, they can either strike the bottom detector to start the timer or the right-side detector to stop the timer. The time between detector strikes is logged to calculate $g^{(2)}(\tau)$. (b) The Hong–Ou–Mandel effect to measure photon indistinguishability. When two identical photons enter a beam splitter, destructive interference ensures they leave through the same output port. Thus, if the output ports are monitored, only one detector should click, indicating truly indistinguishable photon inputs. . . . 6

1.4 Three level energy Lambda system, where two ground states $|1\rangle$ and $|2\rangle$ are coupled to an excited state $|3\rangle$. ν_i is the applied monochromatic plane-wave frequency from $|i\rangle$, and Δ_i is the one-photon detuning. 12

1.5 Phase index and absorption as a function of probe detuning with the control field on (blue) and off (red). Plots are calculated from Eq. 1.16 and Eq. 1.17 with test values of $N = 4 \times 10^{11}$ cm^{-3}, $\mu_{13} = 4 \times 10^{11}$ Cm, $\gamma_{12} = 3$ kHz, $\gamma_{13} = 5$ MHz, $\Delta_2 = 0$ Hz, and $\Omega_c = 4$ MHz. a) The normalized absorption profile originating from Im$[\tilde{n}]$. b) The dispersion profile from Re$[\tilde{n}]$. 17

2.1 Energy level diagram of an InAsP QD embedded in an InP environment. . 19

2.2 (a) Energy levels for a biexciton-exciton cascade, showing the polarization entangled-emission. (b) Spectrum of a QD showing the X, XX and X^- emissions of a QD. 20

2.3 The optical excitation schemes for QDs. Blue (red) circles indicate an electron (hole), with dashed lines illustrating their respective transition paths. The excitation pump is denoted in green, and non-radiative relaxation processes, such as phonons, are depicted in purple. (a) Above band excitation. (b) Quasi-resonant excitation. (c) Resonant excitation. 21

2.4 Frequency shift of X, XX and X^- by nitrogen gas deposition. For 0 min (blue), 3 min (red) and 6 min (orange) at 0.7 mln/min injection rate. Inset: a magnified view of the X frequency shift. 23

2.5 The experimental setup for the QD. The labeled optics are DM: dichroic mirror. 90:10BS: 10% beam sampler. ND: neutral density filter. HWP: Half-wave plate. LP: Linear polarizer. f: focal length of the lens. Collimate: a pair of lenses, along with a long focal length lens of 1 meter, expand and collimate the beams of excitons, biexcitons, and charged excitons before fiber coupling. 24

2.6 The spectrometer/monochromator setup. The spectrometer was built based on a Czerny-Turner setup. Note the schematic lines depicting the optics path do not fully represent the actual divergence and focusing of frequencies typical in a Czerny-Turner spectrometer. In reality, there is a more intricate process of collimation and divergence following the diffraction grating. However, for clarity, the diagram illustrates primarily the spatial separation of different frequency components subsequent to the grating. 26

2.7 (a) The typical setup for a Mach-Zehnder interferometer. (b) Diagram of EOM as just one output arm of the Mach-Zehnder interferometer. By applying a modulated voltage to one path, an electric field is induced in the non-linear crystal, modulating the phase difference between the two paths. This modulation results in intensity variations due to destructive interference. (c) Intensity modulation of output beam as a function of applied voltage. The half-wave voltage V_π is the voltage required to change from the minimum intensity to maximum intensity. The dotted line illustrates the intensity function's variation with voltage due to fluctuations in the EOM's surrounding conditions. 27

2.8 The EOM and it's supporting electrical equipment to convert a continuous laser input into a stabilized and amplitude-modulated output. The EOM stabilizer circuit is used at the DC input to the EOM, while the pulse generator circuit is triggered by a step voltage from a Siglent SDG6022x function generator. The repetition rate of the step-voltage determines the repetition rate of the pulses. The signal is then amplified by a iXblue NIR-MX800 amplifier to create the electronic pulses and fed into the RF input to the EOM. The fiber splitter and Thorlabs PDA100A2 photodetector (PD) are used to pick-off the EOM output for the bias controller. 29

2.9 (a) Block diagram of the circuit. A known square wave dither is applied to the DC port of the EOM. The dither is then compared against the output of the EOM to determine whether the output is symmetric (in-phase) or antisymmetric (180° out of phase). Symmetry testing is done using a series of NMOS and PMOS transistors, along with AND and XOR logic gates. (b) The effect of a small dither on the EOM response curve. If we are to the right of the minimum, the system response will be in-phase with the dither due to the positive slope. If we are to the left of the minimum, the system response will be out of phase with the dither due to the negative slope. (c) A logic table summarizing the adjustments to DC correction based on symmetry testing logic. 30

2.10 (a) Fully assembled EOM bias controller. (b) Drift in EOM output intensity for an 895 nm CW laser at 10 mW with no pulse trigger. Comparison between when the bias controller is turned off (blue) vs. on (red). 31

2.11 Pulse generation circuit designed by Zou et al. [1]. D1: PIN diode. SRD1, SRD2: step recovery diodes. SBD1: Schottky diode. R_L: Load resistor for output. Table: indicates the state of each SRD upon application of a step voltage V_{in}. Timing is with respect to an arbitrary time t. The references t_i denote each diode's phase change during its transition from forward to reverse bias. 32

2.12 (a) Short optical pulse characterization of EOM with the custom-made bias controller and picosecond pulse generator. As the SNSPDs measurements (orange) also introduce an electronic time jitter of about 70 ns, the same pulse was measured on a 12 GHz fast photodetector (blue) to more accurately gauge the pulse widths. (b) $g^{(2)}$ of the QD biexciton emissions excited by the EOM. 33

3.1 Energy levels for a biexciton-exciton cascade, the separation of the excition energy levels are known as the FSS energy(δ). 36

3.2 Same diagram as Figure 2.5, but with an arrow to help identify the fiber coupler to the spectrometer, the HWP, and the polarizer. 37

3.3 Frequency shift of XX (a) and X (b) due to FSS. The vertical (blue) and horizontal (yellow) polarizations indicate the energy difference between the two paths in the cascaded energy levels. 38

3.4 (a) Energy of XX (green) and X (blue) peak centers as the HWP is rotated to switch between the H and V paths of the energy cascade. (b) The centered energy level difference between the X and XX, creating a sinusoidal function with an amplitude of δ. 39

3.5 Frequency shift induced by gas deposition vs. FSS of 16 QDs. Raw data can be found in Table D.1 and Table D.2. A more detailed view of QD (88,1) and QD (78,6) is also provided in Figure 3.6. 40

3.6 Detailed FSS data of QD(88,1) and QD(78,6) illustrating both the exact FSS change and ΔFSS from it's initial value as gas is deposited. 41

3.7 Positions of the melting beam on the NWQD, represented by the gray circles at 8 positions based on NEWS co-ordinates. 42

4.1 (a) Three energy levels of the Cs atom forming a ladder system. (b) Experimental diagram of the T-P DAVLL. By monitoring the transmission of the 895 nm probe, an error signal is created to lock the 761 nm laser. 44

4.2 Typical error signals for the T-P DAVLL signal (Left) and compact saturation spectroscopy setup (Right). As seen on the Toptica DLC Pro control box. 45

4.3 (a) Laboratory setup of the 3D printed push-fit board. Laser inputs are directed to the board using PM fibers. The Cs cell used in the setup is a standard 75mm length cell with no buffer gas. The board dimensions are 26cm × 7cm, and it is securely bolted onto an optics table with fasteners underneath the Cs cell. (b) Top view of the push-fit slot renders for the photodetector side. Components are provided with additional open space in sensitive locations, such as the active area and edges, to prevent damage. (c) Angled view of the render, highlighting the intermediate test points for sliding in IR cards and the apertures printed on the board to aid in alignment. The two apertures on the back of the balanced photodetector side align perfectly with the detectors. 47

4.4 (a) Hyperfine splitting of the energy levels used in the T-P DAVLL lock. Here we use a probe locked between the $6S_{1/2}, F = 4$ to $6P_{1/2}, F = 3$ transition with the CoSy module. The T-P DAVLL locks the $6P_{1/2}, F = 3$ to $8S_{1/2}, F = 3$ transition. (b) In the stability test, the probe is frequency offset-locked to scan across the $6S_{1/2}, F = 3$ to $6P_{1/2}, F = 3$ transition. (c) Experimental diagram of the stability test. By monitoring the drift of the EIT signal from the scanning 895 probe, we obtain an estimate on the 761 nm lock stability. 48

4.5 Resulting probe scans of EIT spectrum. (a) Probe transmission of the $6S_{1/2}, F = 3$ to $6P_{1/2}, F = 3$ transition as measured on SNSPDs. Probe detuning is centered to 0 by a 9.192 GHz offset corresponding to the fine structure splitting of the $6S_{1/2}, F = 3$ and $6S_{1/2}, F = 4$ ground states. (b) The same probe is now under the influence of a counterpropagating control beam at 761 nm, locked by the T-P DAVLL. 49

4.6 EIT peak drift monitored over the duration of 14 hours. The drift is centered around the average value of the EIT peak. 50

5.1 (a) Cs energy levels and hyperfine states used for Lambda EIT Memory. The strong control beam is resonant on $6S_{1/2}, F = 3$ to $6P_{1/2}, F' = 4$ transition, and the weak probe is resonant on $6S_{1/2}, F = 4$ to $6P_{1/2}, F' = 4$. (b) A typical pulse sequence for EIT storage that is aligned in time. The top two traces represent the pulses sent from their respective laser sources, while the bottom trace indicates the expected signal detected after storage, filtered to isolate the probe (i.e. the strong control beam is completely eliminated). . 53

5.2 The experimental setup used for warm cell EIT memory. Broadly speaking separated into 3 main sections of laser pulse preparation, the atomic memory, and the filtering. These are all fiber coupled to each other through single-mode PM fibers. The pulse preparation is perhaps an oversimplification of the pick-offs after the laser head. It is just meant to indicate which tools are used to create pulses. 54

5.3 Diagram and assembly of magnetically shielded oven. (a) Cross-section of the magnetically shielded oven. (b) 1.5" tube with buffer gas cell mounted within by two brass screws. Two circular rings of insulating rubber are wrapped just beside the fasteners. (c) First layer of mu-metal shielding, and second insulating layer. (d) Second layer of mu-metal and metal zip-ties to secure all layers underneath. (e) 2.5" tube with heating tape wrapped around. The 1.5" tube with mu-metal and cell are inserted within. 56

5.4 EIT 895 nm F=4 to F'=4 probe frequency scans with a resonant control beam. (a) Comparison of a Cs cell without buffer gas (blue) and a Cs cell with 3 Torr Neon buffer gas (Orange). (b) Transmission window changes with increasing control power in the buffer gas cell. 57

5.5 The typical EIT memory input pulse sequence as detected on an APD. (a) The input pulse sequence for a given experimental cycle: Two 1 μs, 2.5 mW peak power control pulses (orange) are separated by 50 ns. The 50 ns write signal (blue), with a peak power of 3 μW, is sent along with the first control pulse to store the signal. (b) Plot demonstrates the same experiment repeated at increasing delay times represented by the different colors, showing the characteristic decrease in retrieved pulse area as the storage time increases. 58

5.6 EIT storage total retrieved signal vs. storage delay time to obtain storage time τ. Each plot represents an improvement to the experimental setup. (a) Storage observed in vapor cell without buffer gas, optical pumping, or magnetic shielding. (b) Storage observed in vapor cell with 3 Torr Ne buffer gas and 100 μs optical pumping, but no magnetic shielding. (c) Storage observed in vapor cell with 3 Torr Ne buffer gas, 100 μs optical pumping, and only one layer of magnetic shielding. (d) Storage observed in vapor cell with 3 Torr Ne buffer gas, 100 μs optical pumping, and two layers of magnetic shielding. 59

5.7 Probe signals detected on the APD in different configurations to measure storage efficiency. The blue curve, obtained by removing the Cs cell, provides a transmission reference for the probe and the total photon number sent into the memory. The orange curve represents typical probe absorption without the influence of EIT, from which the storage efficiency is determined. The green curve shows the EIT memory signal, and the retrieved pulse is used to calculate the retrieval efficiency and overall memory efficiency. Inset: a magnified view of the retrieval pulse. 60

5.8 The protocol for a heralded memory based on EIT using the hyperfine ground states of Cs. 62

A.1 Diagram of nitrogen gas flow setup. 76

B.1 Peak splitting. 78

B.2 Symmetry testing logic 79

B.3 PCB for symmetry testing, initially designed by Kassandra Hawes, then modified to fix some connections at the logic gates. (a) Schematic Diagram. (b) Resulting Board. 79

B.4 Circuit to combine square wave dither and DAC. 80

B.5 Layout of front and backside electrical ports for the bias controller circuit. 81

C.1 Effects of changing R2 in Figure 2.11 on pulse widths: $R_2 = 50\ \Omega$ (a), 750 Ω (b), 1.5k Ω (c), resulting in pulse widths of 260 ps, 200 ps, and 100 ps, respectively. Panels (a) and (b) only show the electrical pulse from the pulse generator (yellow), whereas panel (c) also includes the derived optical pulse from the EOM (green). 87

D.1 FSS data of 16 Quantum Dots measured before gas tuning. 90

E.1 Slot dimensions for balanced photodetector, polarizing beam splitter, prism mirror and focusing lens. 94

E.2 Dimensions for QWP mount. 94

E.3 Dimensions for dichroic mirror mount. 95

E.4 Dimensions for Cs cell holder. 95

E.5 Dimensions for fiber adapter mount. 96
E.6 The Koheron Photodetector module, QWP module, DM module and Cs cell holder module mated together by the optical axis (yellow line) and by their edges. 96
E.7 Illustration of push-fit mechanism. These parts are meant to be secured by the 3D printed board itself. 97
E.8 (a) Illustration showing the current incorrect lens position and focal length, with the lens's focal point midway between the PBS and the prism mirror. (b) Proposed corrected setup using a 49.8 mm lens, with the focal point positioned 10 mm before and after the respective photodetectors. Note: beam sizes are not to scale. 98

F.1 Setup for 852 nm etalons. (a) Beam diagram showing signal passing through two Vitawave etalons at 852 nm. Etalon 1 has a finesse of F = 15 at 852 nm, while Etalon 2 has a specification of F = 17 at 852 nm. (b) Experimental setup in the lab. 100
F.2 Noise from monochromator. (a) A typical absorption spectrum of the $6S_{1/2}$, F=4 to $6P_{1/2}$, F'=3 transition. Directly measured on the SNSPDs after the Cs vapor cell. Also see the beginning of the $6S_{1/2}$, F=4 to $6P_{1/2}$, F=4 absorption dip. (b) The same absorption spectrum but now sent through the monochromator before SNSPDs. 101
F.3 Setup used for the optically pumped cell filter. The IR card shows the beam size difference of the pump (less intense, ∼1 cm diameter beam) and signal (bright, ∼mm yellow spot). During experiments, both lasers were frequency off-set locked to their respective transitions and pulsed by AOMs. 102
F.4 Result of probe transmission after optical pumping. The first large peak of 25 μs is the pump pulse, and the second short 1 μs pulse is the signal. The blue curve represents a transmission reference for just the probe signal without the Cs cell in the beam path. The orange curve is the absorption profile of the probe signal without any optical pumping. The green curve is the resulting transmission after the cell has been pumped into the F=3 ground state. In the green curves, we also observe a characteristic "bleaching effect", where the transmission of the pump slowly increases over time as more and more of the atomic population is pumped to the other ground state. (a) For a probe signal on the $6S_{1/2}$, F=4 to $6P_{1/2}$, F=4 transition. (b) For a probe signal on the $6S_{1/2}$, F=3 to $6P_{1/2}$, F=4 transition. 103

F.5 The newly setup 895 etalons used as a narrow bandpass filter to control beam. (a) The mounted 895 nm etalon in a custom made heater. The temperature is stabilized with a temperature controller. Located on the side of the mount is a hole designed to house a temperature probe, which provides feedback to the temperature controller. (b) Normalized transmission profiles of the etalon filter. Blue represents the filtering when used in a double-pass configuration as shown in Figure 5.2, where the polarization in the first pass and second pass are both linear but orthogonal. The orange and green curves show the exact transmission frequencies for the two orthogonal polarizations indicated by a 45 degree difference in HWP setting. (c) Schematic of the double-pass configuration, using a Thorlabs PBS121 PBS, Foctek WPC212H HWP, and Foctek WPC212Q QWP. 105

List of Tables

5.1 Summary of filter performances for the various setups to separate the two Cs hyperfine ground state transitions. F corresponds to the finesse of the Vitawave planar etalons as defined by their spec sheets at 852 nm. 55

C.1 Pico pulse generator characterization with a sine wave input. 88

C.2 Pico pulse generator characterization with a square wave input. 88

D.1 FSS data from Figure 3.5 over all 6 stages of gas injection for 16 QDs. All data presented in μeV. 91

D.2 Detuning data from Figure 3.5 over all 6 stages of gas injection for 16 QDs. All data presented in GHz. 92

Chapter 1

Introduction

The significance of communication can be traced throughout history, starting with early forms like smoke signals and carrier pigeons. Reliable communication has enabled the exchange of information, ideas, and emotions, fostering collaboration and understanding. The journey to today's advanced telecommunication systems has been marked by significant milestones: the invention of the telegraph and telephone in the 19th century, which allowed instant communication over long distances; the development of radio and television in the early 20th century, which brought real-time audio and visual content to mass audiences; and the advent of the internet in the latter part of the 20th century, revolutionizing data exchange and connectivity. This evolution paved the way for mobile telecommunications and wireless technologies, creating our current global communication network. These advancements have collectively transformed how we live, work, and interact, making telecommunication an indispensable component of daily life.

Quantum networks are posed to be the next frontier in communication technology [2, 3, 4], taking advantage of quantum mechanics to enable ultra-secure data transmission and potentially unrivalled computational capabilities. Unlike classical networks that rely on bits, quantum networks use qubits, which can exist in multiple states in the form of superposition and entanglement. The practical implementation of quantum networks faces significant challenges similar to that of it's classical counterpart, particularly due to signal loss over long distances. This is where quantum repeaters become crucial. Initial proposals of quantum repeaters based on heralded entanglement generation behave much like classical repeaters [5]. They act as intermediate nodes, and extend the range of quantum communication by extending range of entangled states, thereby mitigating signal degradation and enabling the creation of large-scale, reliable quantum networks. While many frameworks for quantum repeaters and extending the range of quantum information have

been proposed [4, 6, 7], this thesis will focus on the main experimental effort of the NPQO lab to realize a hybrid quantum repeater node with a quantum dot (QD) photon source interfaced with atomic memories.

The thesis is outlined as follows: the requirements of a ground based quantum repeater and some key quantum phenomena such as electromagnetically induced transparency (EIT) are introduced in Chapter 1. The thesis will then break into three projects, each contributing to an essential aspect of the quantum repeater. Chapter 2 will discuss the characterization of photons from a quantum dot photon source excited by an electro-optic modulator. The following Chapter 3 will investigate the tunability of both wavelength and fine-structure splitting of quantum dots by nitrogen gas deposition. Chapter 4 presents a 3D printed laser locking board used to frequency lock lasers to upper atomic transitions, followed by a discussion on the design process and frequency stability. Chapter 5 introduces warm Cs vapor as the memory component. It discusses the new setup and experimentally observed lifetimes in a lambda EIT memory protocol using the hyperfine states of Cs. Finally, chapter 6 will summarize the thesis and discuss next steps for these projects.

1.1 The Quantum Repeater

The main purpose of the quantum repeater is to enable the practical sharing of quantum information over large distances. This would allow functional applications such as quantum key distribution or quantum entanglement distribution [8, 9]. As light remains one of the most popular quantum information carriers due to its high speed and minimal interaction with the environment [10], it is tempting to directly integrate these qubits into our existing telecommunication infrastructure. However, quantum information cannot be integrated in such a way due to the no-cloning theorem [11, 12]. In telecommunication, when light is sent through channels such optical fibers, they suffer from attenuation in the fiber leading to loss and a lower transmission efficiency. The transmission efficiency (η) of a single-mode fiber at 1550 nm can be approximately modeled as $\eta = e^{-L/L_{att}}$, with an attenuation length $L_{att} = 22$ km [13]. This predicts that the transmission probability is just 1% after 100 km. In classical telecommunication systems, attenuation is overcome by classical repeaters, which are distributed throughout the network to read and send amplified copies of the signal in order to maintain its integrity until it reaches its destination. However on the quantum side, the no-cloning theorem, while a useful feature for security protocols, strictly prevents the duplication of a quantum state, making it impossible to integrate with repeaters as they exist today. Therefore, there must be a new way to combat the attenuation and decoherence quantum states experience as they are sent through channels

such as optical fibers.

An entanglement swapping based quantum repeater follows a similar but fundamentally different strategy than classical repeaters to share quantum information [5]. They are also distributed throughout the network at positions where propagation losses are manageable but extend the overall range of the signal through the technique of entanglement swapping [14]. Entanglement swapping works by creating long-distance entanglement through the consumption of many shorter-range entanglements using Bell state measurements (BSM). A diagram of a potential repeater network is shown in Figure 1.1. To begin, a source of entangled photons stores one qubit in memory[1] while the other is sent to an intermediate point between sources where propagation losses are insignificant. Upon receiving two qubits from two adjacent sources, the intermediate location performs a BSM. The BSM consumes the two qubits but gives information about local operations in order to entangle the two qubits stored in memory, which can be relayed via classical communication to the memory location. Afterwards, the BSM is repeated at each intermediate location to extend the entanglement over even longer distances until the two end points each have a qubit from an entangled state.

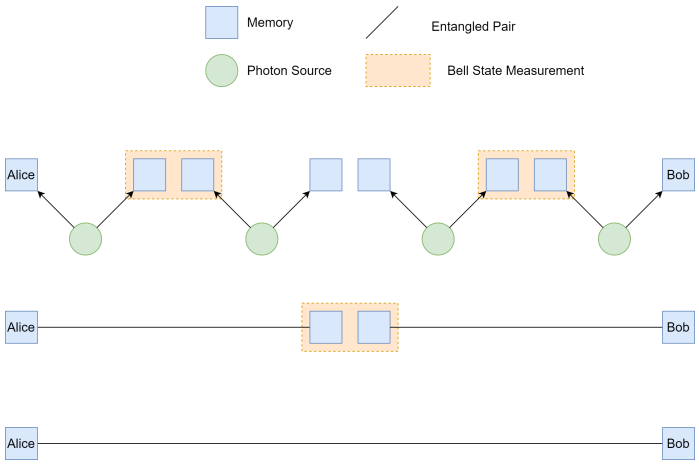


Figure 1.1: Example of a quantum repeater network to extend entanglement to end points Alice and Bob.

From the procedure described above, there are two main components to a quantum repeater: an entangled photon source and a quantum memory (there is also a need for

[1] A quantum memory is a physical setup where a quantum state is locally stored and can be read out ideally on demand at a later point in time. This storage and retrieval process must preserve the quantum properties of the state, such as superposition and entanglement.

high-performance single photon detectors but that is beyond the scope of this thesis). The need for the photon source is intuitive as it is the source of our quantum information and qubits, however the quantum memory is mutli-purpose. For example, a typical BSM involves a Hong-Ou-Mandel interferometer scheme where two photons interfere at a 50:50 beam splitter (BS) at the same time [15]. Afterward, they are sent through additional optics depending on the encoding method and finally strike a detector, indicating their Bell state with a non-unity success probability [16, 17]. Such a setup is shown in Figure 1.2. To perform this measurement, the quantum memory not only stores one qubit but also synchronizes the arrival of photons to the BSM and enables higher efficiency as now the entire chain of BSM do not need to succeed in a single shot. By using a heralded entanglement swapping approach, only the failed segments must be repeated [13, 16, 18].

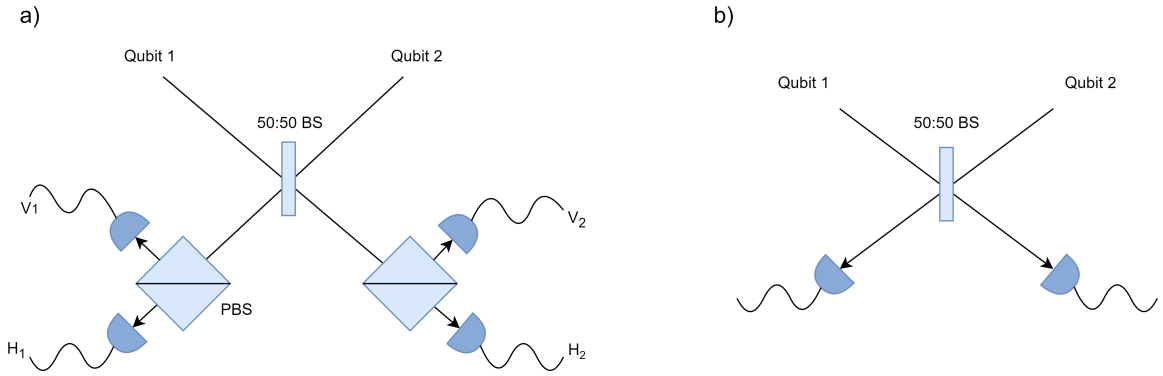


Figure 1.2: Examples of BSM setups using linear optics. The projected Bell states depend on which detectors click. a) BSM for polarization encoded qubits. H and V indicate the detector responsive to horizontal and vertical polarizations. b) BSM for Fock-encoded qubits.

1.1.1 Quantum Repeater Hardware

This section aims to clarify the specifications required for the photon source and memory component to achieve a functional quantum repeater. Many efforts at ground-based quantum repeaters often use the same hardware for it's photon source and memory. Such a setup guarantees the compatibility of the two systems, but very often sacrifices one key performance metric for another [13, 19, 20, 21]. For this reason, we will also discuss some traditional hardware choices and provide background on why a QD photon source was chosen to interface with atomic memories in our lab.

Some characteristics an ideal photon source should have are:

1. **Single-photon emission**: The source only emits a single photon at a time, with zero probability of emitting multiple photons. This is characterized by the second-order correlation function $g^{(2)}(\tau)$:

$$g^{(2)}(\tau) = \frac{\langle \hat{a}^\dagger(t)\hat{a}^\dagger(t+\tau)\hat{a}(t+\tau)\hat{a}(t)\rangle}{\langle \hat{a}^\dagger(t)\hat{a}(t)\rangle^2} \tag{1.1}$$

   where $\hat{a}^\dagger(t)$ is the photon creation operator, $\hat{a}(t)$ is the annihilation operator, $\langle\rangle$ is the time averaged value and τ is the time delay between two photon detection events. In a physical sense, the function describes the probability of detecting a second photon at a time $t+\tau$ after a first photon is detected at time t. When $\tau = 0$, we are measuring the likelihood of detecting two photons at the same time, so an ideal photon source would have a $g^{(2)}(0) = 0$. Experimentally, this is accomplished by the well known Hanbury-Brown-Twist setup as shown in Figure 1.3(a) [22].

2. **Deterministic**: The timing of the single-photon emission should be triggered on-demand by the user. The trigger typically describes some electrical or optical excitation of the system in order to obtain an emitted signal. Truly on-demand single-photon sources would require a high efficiency and photon pair generation probability of near unity, while also maintaining the requirement of only generating a single photon-pair at a time.

3. **Repetition rate**: Often called the "brightness" of the source. A high repetition rate is required to enable fast information transfer. For QKD protocols speeds on the order of Gbps are desirable but perhaps ambitious [22]. Lower speeds are usable for proof of concept and information processing applications [7].

4. **Indistinguishable**: The emitted single photons should be of the same known physical properties every time. These properties include polarization, frequency, temporal and spatial profiles. Indistinguishably is quantified by a Hong-Ou-Mandel (HOM) measurement shown in Figure 1.3(b). Note that this effect is also used for the BSM described previously in Figure 1.2.

5. **Frequency compatibility**: The emission wavelength of the photon must be compatible with the remainder of the system. This includes the channel used to transfer the single-photons, the detectors used and the memory. The source to memory interface can be achieved either by choosing the same system for both, or by developing a method to tune the frequency of the source to match the memory. Ideally, the memory should also have a larger bandwidth than the source for efficient interfacing.

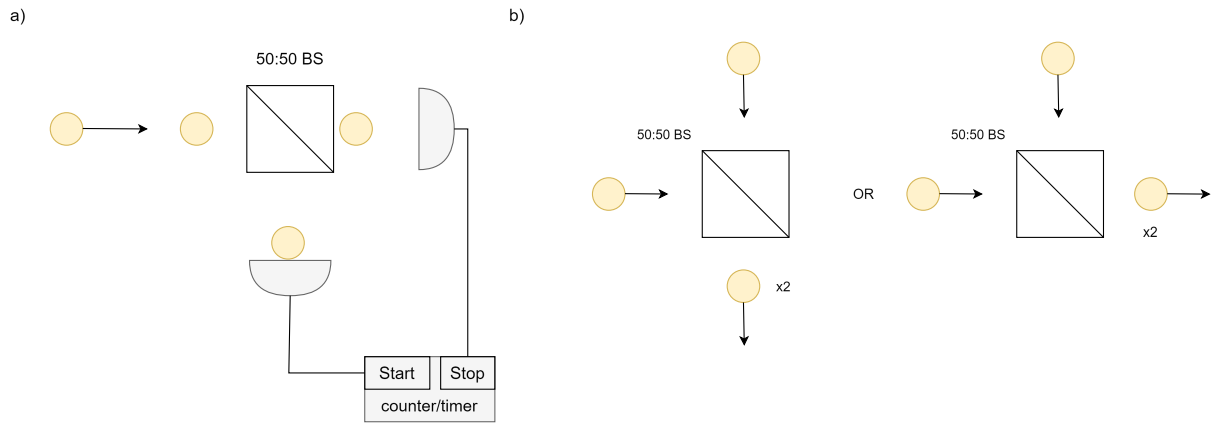


Figure 1.3: (a) The Hanbury-Brown-Twiss setup to measure $g^{(2)}(\tau)$: the second-order correlation function. Photons from the source are sent to a 50:50 beam splitter. After the beam splitter, they can either strike the bottom detector to start the timer or the right-side detector to stop the timer. The time between detector strikes is logged to calculate $g^{(2)}(\tau)$. (b) The Hong–Ou–Mandel effect to measure photon indistinguishability. When two identical photons enter a beam splitter, destructive interference ensures they leave through the same output port. Thus, if the output ports are monitored, only one detector should click, indicating truly indistinguishable photon inputs.

Practically, the above characteristics for on-demand single-photon sources are difficult to achieve but many groups have used high performance sources to demonstrate key milestones for quantum repeaters [21, 23, 24].

Non-deterministic sources such as non-linear crystals or some atomic emitters are easy to implement but suffer from low efficiencies and rely on non-linear phenomena such as spontaneous parametric down-conversion (SPDC) or spontaneous four-wave mixing (FWM), which are probabilistic sources [21, 25]. Although the arrival time is unknown, these probabilistic sources produce two photons, and the detection of one of the photons can guarantee (herald) the emission of the other. To increase the rate of entangled photons, one may increase the pump power, but this also comes with a trade-off of a higher probability of producing multiple photon pairs.

Options for on-demand sources are often based on isolated quantum systems with distinct energy levels; single photons are emitted from a radiative decay from the upper to lower energy levels. Some common choices include single atoms [26], NV-centers [27], and quantum dots [28]. Single atoms and ions are challenging to work with as it can be difficult to isolate them. They also often suffer from poor detection efficiency and a low repetition

rate from their long excited state lifetimes [7, 29]. In comparison, solid-state detectors are attractive for their scalability and brightness. While NV-centers have been proposed due to their potential at room temperatures, we will focus on QD single-photon sources. QD sources can be thought of as artificial atoms carefully engineered from semiconductors. By controlling the size and material of the QD, we can design its emission wavelength to match a selection of memory options. These QD sources have shown potential for high clock rates approaching ∼GHz while also maintaining a low $g^{(2)}(0)$ [24]. Compared to other sources, such as SPDC, FWM, and atomic emitters, which have been shown to only reach the range of 1-100 MHz repetition rate [7]. Furthermore, by placing the QD in cavities, we can promote their emissions into specific, more controlled modes. The details of the QD source are described further in chapter 2.

Now that there is some intuitive understanding of the source, let us move to the memory component. The characteristics of an ideal quantum memory share many similarities with photon sources. Some (but not all) of the important criteria we investigate for the memory are:

1. **On-demand**: The memory can be accessed at specific times chosen by the user, rather than at predefined intervals, enabling more practical and versatile applications. This also allows high precision timing of the photon for synchronization applications in quantum computing and networks. There are even schemes using a quantum memory to convert a heralded photon source based on SPDC into a deterministic source [25].

2. **Memory efficiency (η)**: How effectively the memory can store and retrieve quantum information. Precisely speaking, it is the integrated intensity ratio of light retrieved from storage vs. the light sent into storage [30]. The total memory efficiency η can be further broken down into storage efficiency (η_{sto}) and retrieval efficiency (η_{ret}), where $\eta = \eta_{sto}\eta_{ret}$. The storage efficiency is the fraction of the input information that is successfully stored in the quantum memory. The retrieval efficiency is the fraction of the stored quantum information that is successfully retrieved from the quantum memory.

3. **Lifetime (τ)**: The duration for which the information can be stored. This, along with attenuation, sets an upper bound on the distance between quantum repeater nodes. It is measured by the time it takes for the retrieved photon population to reach 1/e of its maximum value. Many models predict that storage times for long-distance quantum repeaters' round trip should be roughly in the 100-1000 μs regime [5, 30].

4. **Bandwidth**: The range of frequencies over which the memory can effectively store and retrieve quantum information is typically defined by the full width at half maximum (FWHM) of the retrieved pulse intensity in a frequency scan. Short pulses in time are desirable for high-speed operations. However, according to the Fourier transform, a short pulse in the time domain corresponds to a wide range of frequencies in the frequency domain. Therefore, bandwidth is also a crucial parameter that impacts the rate at which quantum information can be processed and transferred.

5. **Fidelity (F)**: How accurately the quantum memory can store and retrieve quantum states without changing it's information through losses or decoherence. High fidelity is crucial for practical applications in quantum computing and communication. It is traditionally defined as $F(\rho, \sigma) = \mathrm{Tr}\left(\sqrt{\sqrt{\rho}\sigma\sqrt{\rho}}\right)^2$, where ρ and σ are two quantum states in their density matrix form.

6. **Frequency compatibility**: The memory should operate within the frequency range necessary to accept photons emitted by the entangled photon source, and its bandwidth should be similar to or larger than that of the photon source for efficient interfacing [21]. If the photon is not initially within an ideal frequency range for long-distance communication (e.g., around 1550 nm for telecom or around 785 nm for satellite [31]), ideally, the photon should be capable of converting to these wavelengths.

7. **Scalability**: The size, weight, and power (SWaP) of the memory should be minimized to enable its scalability. If a large scale quantum network were to be realized, large amounts of memory nodes would have to be implemented throughout the entire fiber optic network, similar to classical repeaters. To enable such widespread distribution, the complexity of the setup must also be reduced, as each additional part can potentially be a source of failure.

A traditional choice for optical memories is fiber optic delay lines, where the storage of information is accomplished fairly easily by guiding the signal through extremely long optical fibers and increasing the optical path length. These are among the highest-performing broadband memories in terms of efficiency and lifetimes [30]. However, they suffer from a fixed delay time, dispersion, propagation losses, and a limited wavelength range in the telecom band, which makes them unable to directly interface with many single-photon sources.

Currently, most investigated quantum memories rely on converting the optical qubit into a stationary qubit through some storage medium. These methods provide an on-demand memory, and the storage time is typically limited by the decoherence of the

medium. Neutral atoms, ions, NV-centers, or even quantum dots are some common choices; alkali atoms are particularly attractive due to their long-lived coherences and memories [16]. In this case, the coherence of the optical signal is transferred to and retrieved from a collective ground state excitation of atomic ensembles. Furthermore, Cs atoms are of interest as the D1 transition of 895 nm is in the region of InAsP QD emissions, allowing us to interface the two at least in terms of frequency. While this wavelength isn't necessarily efficient for long-distance communication, cesium's upper transitions from the $6P_{1/2,3/2}$ hyperfine states to $7S_{1/2}$ state give access to telecommunication wavelengths at 1310/1469 nm, and upper transitions to $8S_{1/2}$ offer opportunities for satellite communication, providing access to wavelengths at 761/794 nm [31]. So although the common D-line wavelengths used to communicate with atoms are inefficient for long-distance communications, they can be converted to efficient communication frequencies through four-wave mixing.

Both warm and cold atomic memories have been extensively studied and deployed in the past. The most significant difference between the two systems is the trade-off between their experimental complexity and performance. Cold atom systems require laser cooling and trapping inside a vacuum. Often, the atoms are placed in optical cavities to further enhance their interactions [32]. While this makes scaling cold atom setups difficult, we observe much longer storage times because we have more control over the positioning of the atoms and there are fewer collision-dependent losses due to reduced thermal motion. The atomic energy levels are also more precise, as there is almost no Doppler broadening.

Warm atomic setups are much easier to implement and access, thanks to the commercial availability of atomic vapor cells. However, these systems are more prone to decoherence due to the thermal motion of atoms[2], atomic collisions, and stray magnetic fields. Most experiments use finite beam sizes, causing atoms to move in and out of the interaction region, leading to efficiency losses and reduced storage times. Additionally, inelastic collisions with other atoms or the cell wall cause collision-induced dephasing, thereby limiting memory lifetime further [33].

Despite these challenges to memory lifetime, warm atomic vapors have demonstrated storage times in the microseconds to seconds regime [34, 35]. A notable example is the 160 μs storage and retrieval of light in existing fiber networks with 95% fidelity, as shown by Wang et al. [36]. In terms of equipment, warm atomic memories only require a magnetic shield, heating, and often a specialized vapor cell with a polymer coating or buffer gas. The magnetic shield reduces stray magnetic fields that lead to undesirable Zeeman splitting and dephasing [36]. Heating controls the optical depth (OD) of the medium by controlling

[2]The atoms in a vapor cell move randomly; their velocity depends on the temperature of the atoms, and the velocity distribution can be modeled by a Maxwell-Boltzmann distribution.

the cell's vapor pressure. A high OD is desired as it often sets an upper bound on the interaction strength between atoms and the signal light. Heating the vapor cell comes with the trade-off of increased atomic motion, which can dominate at high temperatures. To mitigate collision-induced losses, a polymer wall coating or buffer gas can be used. Paraffin-coated walls reduce atom-wall collision dephasing, and other specialized polymers have been studied to further improve storage times [37]. Finally, an inert buffer gas such as neon aims to reduce atomic motion by acting as a non-interacting buffer between alkali atoms, keeping atoms in the active region to enhance memory efficiency and minimize collisions, thereby improving storage time. While collisions with the buffer gas do not affect coherence times, they can cause measurable fidelity loss of the quantum state at readout when higher concentrations of buffer gas are used [38, 39]. Like many practical systems, optimizing the various parameters of a vapor cell is crucial to achieving a high-quality memory.

1.1.2 The Hybrid Quantum Repeater

Broadly speaking, the hardware mentioned above such as atoms, ions, molecules, QDs, and NV centers can function both as memories and photon sources, but each has inherent and complex trade-offs in performance when used as a photon source versus a quantum memory [13]. It is tempting, therefore, to combine the best characteristics of two different base systems to create a functional hybrid quantum repeater. In our approach, we aim to combine the advantages of a tunable, on-demand, bright, and stationary QD solid-state emitter with the long-lived memory observed in cold atoms, enabling wavelength conversion to classical telecom compatibility. Previously, cold atoms have been the main focus of our lab; however, we have also started to build and investigate light-matter interactions in warm atomic vapors. Ultimately, it would be interesting to interface the QD with both setups and use warm atoms as a sandbox or benchmark to evaluate the performance of cold atoms in various frequency conversion or memory schemes, as new experiments can be more easily integrated into warm atomic setups due to their reduced complexity.

One drawback of such a hybrid system is the mismatch between the large bandwidth of QD photons, on the order of GHz, and the narrow atomic transition linewidths, typically on the order of MHz. The narrow linewidths of atoms are often desirable for observing long-lived memories, but this also makes storing light with large bandwidths or short pulses difficult. This problem is known as the linewidth-bandwidth mismatch, resulting in decreased memory efficiency as photon bandwidth increases [30]. To address this issue in cold atomic setups, we aim to achieve a high optical depth (OD) and enhance light-matter interactions by confining atoms and photons in a hollow-core photonic crystal fiber [40, 41].

Conversely, warm atomic setups may explore methods such as increasing temperature or adopting larger bandwidth protocols like stimulated-Raman memories [38].

Another issue is the difficulty in manufacturing quantum dots to precisely match the frequency of atomic transitions. Even with top-of-the-line QD manufacturing techniques, emission wavelengths typically have standard deviations on the order of THz [42]. One solution is to manufacture thousands of QDs and select those with emission wavelengths close to Cs transitions at 894 nm. Then, to precisely match the frequency to the atomic transition, a custom in-situ tuning method involves depositing nitrogen gas onto the QD cryostat [42]. The deposited nitrogen ice applies stress to the underlying QD, causing a blue shift in its emission wavelength. Later, this process can be reversed by applying a high-intensity laser to vaporize the deposited ice.

1.2 Electromagnetically Induced Transparency

Electromagnetically induced transparency (EIT) is a coherent phenomena arising from the interaction of a three-level energy system coupled by a weak probe and a strong control beam. In the absence of the control beam, the probe light is absorbed by the medium as a typical two-level system, however when the strong coupling beam is applied a transparency window opens up such that the probe light is transmitted [43, 44]. This effect serves as the basis for many interesting applications with applications to quantum communication such as slow light [45, 46, 47], precision spectroscopy [48, 49] and laser cooling [50, 51]. This section will discuss it's fundamental mechanism to provide background for it's application in laser frequency locking [52] and photonic memories [30, 53, 34, 38, 54] which are discussed further in chapter 4 and chapter 5 respectively.

1.2.1 The Dark State

EIT can be realized in a three-level energy system, where two of the energy levels are not directly coupled. We will consider a Lambda system such as that in Figure 1.4, but the same concept can be applied to ladder and V-type systems as well since the difference between the three systems is only the sign of the detuning. The analysis of transmission and slow light phenomena of EIT can be understood by analyzing it's complex refractive index $\tilde{n}$, but the general idea can also be derived by solving for the eigenstates of the Hamiltonian [44]. To begin, let us analyze the total Hamiltonian H while ignoring the decays for now:

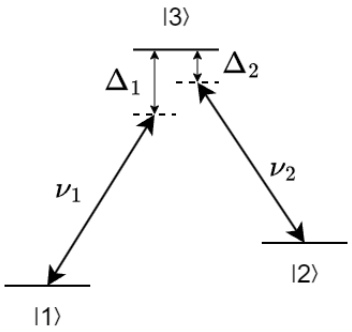


Figure 1.4: Three level energy Lambda system, where two ground states $|1\rangle$ and $|2\rangle$ are coupled to an excited state $|3\rangle$. ν_i is the applied monochromatic plane-wave frequency from $|i\rangle$, and Δ_i is the one-photon detuning.

$$H = H_A + H_{AF} \tag{1.2}$$

where H_A is the free atomic Hamiltonian and H_{AF} is the atom-field interaction Hamiltonian from the laser fields coupling to the atomic energy levels. First we will define a basis from the energy levels as:

$$|1\rangle = \begin{pmatrix} 1 \\ 0 \\ 0 \end{pmatrix}, \quad |2\rangle = \begin{pmatrix} 0 \\ 1 \\ 0 \end{pmatrix}, \quad |3\rangle = \begin{pmatrix} 0 \\ 0 \\ 1 \end{pmatrix} \tag{1.3}$$

By setting the energy level of $|3\rangle$ to 0, where ω_{13} and ω_{23} are the corresponding resonant frequencies to the excited state $|3\rangle$, the free atomic Hamiltonian can be represented as:

$$H_A = \begin{pmatrix} -\hbar\omega_{13} & 0 & 0 \\ 0 & -\hbar\omega_{23} & 0 \\ 0 & 0 & 0 \end{pmatrix} \tag{1.4}$$

Under the dipole approximation, we can ignore the variations in the electric field over the atom because the wavelength is much larger than the size of the atom. The electric field of the lasers can be described as $E_i = \hat{\epsilon}_i \mathcal{E}_i \exp(-i\nu_i t) + c.c.$, where $\hat{\epsilon}_i$ is the polarization unit vector, $\mathcal{E}_i$ is the electric field amplitude, and ν_i is the monochromatic plane-wave frequency.

The interaction Hamiltonian can then be described by the potential energy of a dipole in an electric field:

$$H_{AF} = \begin{pmatrix} 0 & 0 & -\mu_{13}E_1 \\ 0 & 0 & -\mu_{23}E_2 \\ -\mu_{13}E_1 & -\mu_{23}E_2 & 0 \end{pmatrix} \tag{1.5}$$

where μ_{ij} is the dipole moment of the atomic transition from $|i\rangle$ to $|j\rangle$. By substituting Eq. 1.4 and Eq. 1.5 back into Eq. 1.2, we obtain the total Hamiltonian as:

$$H = \begin{pmatrix} -\hbar\omega_{13} & 0 & -\mu_{13}E_1 \\ 0 & -\hbar\omega_{23} & -\mu_{23}E_2 \\ -\mu_{13}E_1 & -\mu_{23}E_2 & 0 \end{pmatrix} \tag{1.6}$$

To calculate the evolution, we apply the Schrödinger equation $i\hbar\frac{d}{dt}|\psi\rangle = H|\psi\rangle$ to Eq. 1.6. As we are interested in slow dynamics and steady-state solutions, we can further simplify the Hamiltonian by using the rotating-wave approximation and moving to a rotating frame. Under the condition of weak near-resonant fields, these operations together completely eliminate the time dependency in the Hamiltonian [55, 56]. The rotating-wave approximation allows us to remove the fast oscillating terms originating from the expansion of the interaction Hamiltonian. When near-resonant fields are present, these terms oscillate at approximately twice the resonant frequency and average to zero over the detector response time, as measurements occur at a much lower frequency. Simultaneously, moving to a rotating frame allows us to shift our frame of reference to the field's frequency, effectively eliminating the remaining oscillating terms.

The resulting Hamiltonian in the rotating frame $\tilde{H}$ is then:

$$\tilde{H} = \begin{pmatrix} -\hbar\Delta_1 & 0 & -\mu_{13}\mathcal{E}_1 \\ 0 & -\hbar\Delta_2 & -\mu_{23}\mathcal{E}_2 \\ -\mu_{13}\mathcal{E}_1^* & -\mu_{23}\mathcal{E}_2^* & 0 \end{pmatrix} \tag{1.7}$$

with Δ_i being the single-photon detuning of each laser from their transitions, it is also convenient now to define $\delta = \Delta_1 - \Delta_2$ as the two-photon detuning. On two-photon resonance ($\delta = 0$), one of the new eigenstates from Eq. 1.7 is a state fundamental to the behavior of EIT known as the dark state $|D\rangle$,

$$|D\rangle = \frac{\Omega_c|1\rangle - \Omega_p|2\rangle}{\Omega} \tag{1.8}$$

where $\Omega_c = \mu_{23}\mathcal{E}_2/\hbar$ and $\Omega_p = \mu_{13}\mathcal{E}_1/\hbar$ are the individual Rabi frequencies which we will term the control and probe fields respectively, and $\Omega = \sqrt{\Omega_c^2 + \Omega_p^2}$ is a generalized Rabi frequency. The significance of the dark state is the lack of coupling to $|3\rangle$, meaning if the atoms were prepared in this state, even a strong resonant laser will not induce a transition to $|3\rangle$ and therefore the beam will simply transmit through the medium. Under the typical EIT conditions of a strong control and weak probe ($\Omega_c \gg \Omega_p$), the dark state is approximately the same as the ground state $|1\rangle$. While the single-photon detuning of Δ_1 and Δ_2 can be non-zero, it is critical to maintain a two-photon detuning of $\delta = 0$ in order to avoid changes in the dark state phase, which effect the coherence times [56]. The dark state with a non-zero δ becomes:

$$|D\rangle = \frac{\Omega_c |1\rangle - e^{-i\delta t}\Omega_p |2\rangle}{\Omega} \tag{1.9}$$

To prepare the dark state, one can first perform an optical pumping stage with a strong control [46]. An atom in $|2\rangle$ will excite to $|3\rangle$ and potentially fall into $|1\rangle$ where it remains or fall back into $|2\rangle$ where the excitation repeats. This process continues until the atomic population is transferred to $|1\rangle$. At this point, introduction of a weak probe beam will not effect the atomic populations, and leads to the main phenomena of EIT, where the atoms are now transparent to an otherwise resonant light field.

1.2.2 The Transparency Window and Slow Light

Previous analysis of the dark state provides some intuition of EIT, but to fully grasp the transparency window, slow light and the effect of decays, it's necessary to solve the complex refractive index. This is easier to solve in the density matrix form. Given a state in the form of density matrix ρ, the diagonals of the density matrix (ρ_{ii}) contains information of populations, while the off-diagonal elements ($\rho_{ij}, i \neq j$) contains information about the coherences.

$$\rho = \begin{pmatrix} \rho_{11} & \rho_{12} & \rho_{13} \\ \rho_{21} & \rho_{22} & \rho_{23} \\ \rho_{31} & \rho_{32} & \rho_{33} \end{pmatrix} \tag{1.10}$$

The time-evolution of the state can be modelled by the Shrödinger-von Neumann equation in the rotating frame [55]:

$$\partial_t \rho = \frac{-i}{\hbar}[\tilde{H}, \rho] \tag{1.11}$$

The equations of motion from the density matrix become:

$$\begin{aligned}
\partial_t \rho_{11} &= -i\Omega_p \rho_{13} + i\Omega_p^* \rho_{31} \\
\partial_t \rho_{22} &= -i\Omega_c \rho_{23} + i\Omega_c^* \rho_{32} \\
\rho_{33} &= 1 - \rho_{11} - \rho_{22} \\
\partial_t \rho_{21} &= i\delta \rho_{21} - i\Omega_p \rho_{23} + i\Omega_c^* \rho_{31} \\
\partial_t \rho_{31} &= i\Delta_1 \rho_{31} + i\Omega_c \rho_{21} + i\Omega_p^* (\rho_{11} - \rho_{33}) \\
\partial_t \rho_{32} &= i\Delta_2 \rho_{32} + i\Omega_p \rho_{12} + i\Omega_c^* (\rho_{22} - \rho_{33})
\end{aligned} \tag{1.12}$$

Now we include the decay terms as Γ_i: population decay out of $|i\rangle$, γ_{ij}: decoherence rate of ρ_{ij}, and r_{ij}: decay branching ratio from $|i\rangle \, to \, |j\rangle$.

$$\begin{aligned}
\partial_t \rho_{11} &= r_{31}\Gamma_3 - i\Omega_p \rho_{13} + i\Omega_p^* \rho_{31} \\
\partial_t \rho_{22} &= r_{32}\Gamma_3 - i\Omega_c \rho_{23} + i\Omega_c^* \rho_{32} \\
\rho_{33} &= 1 - \rho_{11} - \rho_{22} \\
\partial_t \rho_{21} &= -(\gamma_{12} - i\delta)\rho_{21} - i\Omega_p \rho_{23} + i\Omega_c^* \rho_{31} \\
\partial_t \rho_{31} &= -(\gamma_{13} - i\Delta_1)\rho_{31} + i\Omega_c \rho_{21} + i\Omega_p (\rho_{11} - \rho_{33}) \\
\partial_t \rho_{32} &= -(\gamma_{23} - i\Delta_2)\rho_{32} + i\Omega_p \rho_{12} + i\Omega_c (\rho_{22} - \rho_{33})
\end{aligned} \tag{1.13}$$

If we consider the steady-state solution in the weak probe regime ($\Omega_p \ll \Omega_c$) and assume the initial population is in $|1\rangle$ i.e. $\rho_{11} = 1$ and $\rho_{22} = \rho_{33} = 0$, then Eq. 1.13 simplifies to:

$$\begin{aligned}
0 &= -(\gamma_{12} - i\delta)\rho_{21} + i\Omega_c^* \rho_{31} \\
0 &= -(\gamma_{13} - i\Delta_1)\rho_{31} + i\Omega_c \rho_{21} + i\Omega_p
\end{aligned} \tag{1.14}$$

Note that the coherence term $\rho_{23} = 0$, as this is a coherence between two empty states.

Solving for ρ_{31} and ρ_{21} yields:

$$\begin{aligned}
\rho_{21} &= \frac{-\Omega_p \Omega_c^*}{(\gamma_{12} - i\delta)(\gamma_{13} - i\Delta_1) + |\Omega_c|^2} \\
\rho_{31} &= \frac{i\Omega_p (\gamma_{12} - i\delta)}{(\gamma_{12} - i\delta)(\gamma_{13} - i\Delta_1) + |\Omega_c|^2}
\end{aligned} \tag{1.15}$$

The susceptibility χ is given by the density matrix element corresponding to the optical coherence of the transition [46, 55]. For the probe in a medium of atomic density N:

$$\chi = \frac{N\mu_{31}^2}{\hbar\epsilon_0\Omega_p}\rho_{31} = i\frac{N\mu_{13}^2}{\hbar\epsilon_0}\frac{(\gamma_{12} - i\delta)}{(\gamma_{12} - i\delta)(\gamma_{13} - i\Delta_1) + |\Omega_c|^2} \tag{1.16}$$

This allows us to calculate the complex refractive index $\tilde{n}$, phase index n and absorption coefficient a for the probe beam [55].

$$\begin{aligned} \tilde{n}(\omega) &= \sqrt{1+\chi} \\ n(\omega) &= \mathrm{Re}[\tilde{n}(\omega)] \\ a(\omega) &= 2k_0\,\mathrm{Im}[\tilde{n}(\omega)] \end{aligned} \tag{1.17}$$

As shown from Figure 1.5, the strong control field opens a transparency window for the resonant probe such that it can transmit through the atomic medium with minimal absorption. From the dispersion profile we also observe a steep slope around resonance, resulting in a reduction in group velocity of the probe beam[3]. These two significant characteristic of EIT are the basis for the laser frequency locking in Chapter 4 and photonic memory in Chapter 5, which will be discussed in more detail in their respective chapters.

[3]Recall group velocity is inversely proportional to the first derivative of refractive index with respect to frequency, $v_g = \frac{c}{n+\omega\frac{\partial n}{\partial\omega}}$

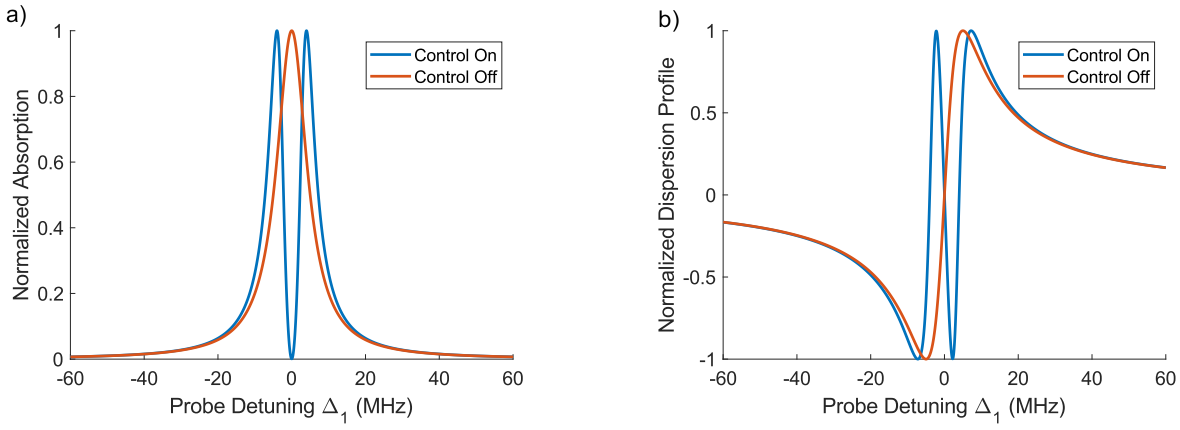


Figure 1.5: Phase index and absorption as a function of probe detuning with the control field on (blue) and off (red). Plots are calculated from Eq. 1.16 and Eq. 1.17 with test values of $N = 4 \times 10^{11}$ cm^{-3}, $\mu_{13} = 4 \times 10^{11}$ Cm, $\gamma_{12} = 3$ kHz, $\gamma_{13} = 5$ MHz, $\Delta_2 = 0$ Hz, and $\Omega_c = 4$ MHz. a) The normalized absorption profile originating from Im$[\tilde{n}]$. b) The dispersion profile from Re$[\tilde{n}]$.

Chapter 2

QD Photon Source

This chapter aims to describe the QD photon source we have in the laboratory and explores excitation of the QD with an electro-optic modulator (EOM). We begin by discussing the working principle of QDs and how they could be tuned to interface with the atomic transitions. Next, we present the current setup in detail. Finally, we demonstrate a modular EOM setup along with the supporting electronics, such as pulse generators and EOM bias controllers.

2.1 Nanowire QDs

The electrical properties of semiconductors are understood through their valence band and conduction band. The valence band is the range of electron energies where electrons are still bound to atoms in the crystal lattice and do not have enough energy to move freely and conduct current. The conduction band is a higher range of energies where electrons can move freely within the lattice, allowing them to conduct current. The energy gap between these bands is known as the band gap and determines the material's conductivity. As the name suggests these two energy regions are bands, and allow a continuous range of available energies. However, when a small $\sim$nm piece of a smaller band gap material is placed within a larger band gap material, quantum confinement effects causes the energy levels of the electrons to become quantized, much like the quantization of a finite quantum well [22]. By adjusting the size of the QD and selecting suitable semiconductor materials, the specific energy levels can be precisely engineered. However, the precision has a limit and the state of the art QD has a standard deviation of $\sim$5nm [57]. In our lab, we use an

InAsP QD embedded in a InP nanowire waveguide. The schematic energy level diagram for a QD is illustrated in Figure 2.1.

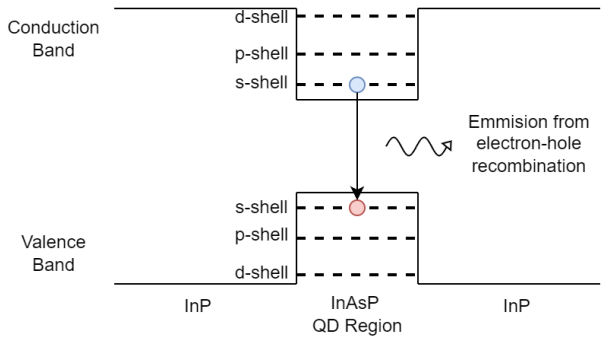


Figure 2.1: Energy level diagram of an InAsP QD embedded in an InP environment.

The discrete energy levels of QDs closely resemble the orbitals of atoms, following a similar naming convention where the first energy level is denoted as "s", the second as "p", etc. This resemblance has led to QDs being referred to as "artificial atoms". From these atomic-like energy levels, the excitation and decay processes of QDs can be treated analogously to those of atomic systems. Specifically, when an electron in the QD is excited, it transitions to a higher energy state, leaving a hole in the valence band. Subsequently, the electron will decay back to the valence band, emitting a photon through the process of electron-hole recombination. The excited state of having a single electron-hole pair bounded to each other is known as an exciton (X). There also exists a state in which two electron-hole pairs with opposite spins are excited, known as a bi-exciton (XX). The X and XX states are the energy levels used to create polarization entangled photon pairs from QDs as they form a cascaded level system, such as in Figure 2.2(a) [58]. Due to additional binding energies, the energy difference between XX and X states is typically smaller than that between the X state and the ground state [59]. The decay path from the XX state depends on which spin decays first to an X state, and based on selection rules[1], the emission must be of a specific polarization. The subsequent emission from the exciton state then follows a similar requirement. The resulting XX-X emission forms one of the bell states for polarization entangled qubits $|\Phi^+\rangle = \frac{1}{\sqrt{2}}(|HH\rangle + |VV\rangle)$, where $|H\rangle$ and $|V\rangle$ are the horizontal and vertical polarizations, forming an orthonormal basis for the quantum state. In addition, we also commonly observe the emission of unequal electron-hole pair states

[1]One aspect of selection rules involves the conservation of angular momentum, where only specific transitions between states are permitted. The difference in angular momentum must be compensated for by the polarization component of the emitted or absorbed light.

known as a charged exciton (X^-), formed by an exciton and an extra singular electron. An example emission spectrum containing the X, XX and X^-, is shown in Figure 2.2(b).

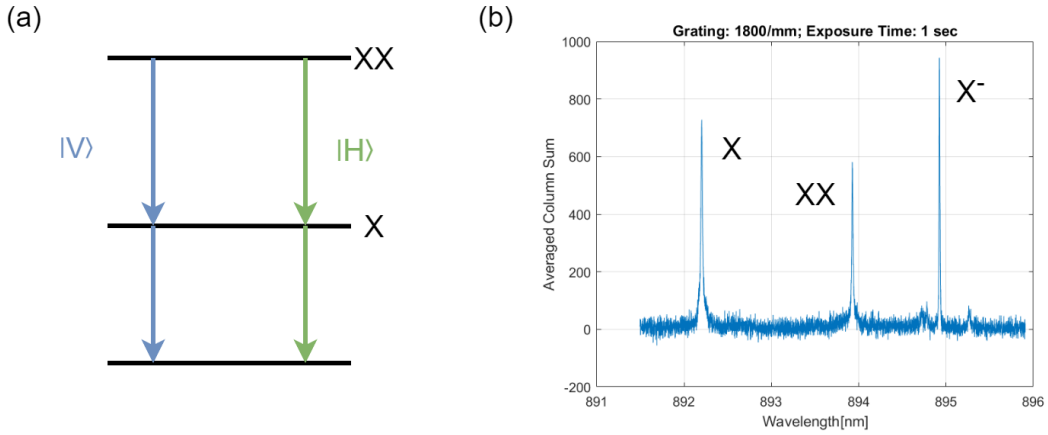


Figure 2.2: (a) Energy levels for a biexciton-exciton cascade, showing the polarization entangled-emission. (b) Spectrum of a QD showing the X, XX and X^- emissions of a QD.

Often, to enhance the emission and collection efficiency of QDs, they are integrated into an optical cavity [60]. Nanowire QDs (NWQD) are particularly interesting as they act like a waveguide such that the emissions are dominated along the waveguide propagation direction, and the emission is in a much more controlled mode. This enables efficient beam collimation and eventual coupling into a single-mode fiber. NWQDs have also demonstrated enhanced emission characteristics over a broader frequency range compared to alternatives such as high-Q cavities [22]. In our setup, InAsP QDs are embedded in InP tapered nanowires, which provide both the waveguide structure and the confinement effect. These nanowires are then placed in a 4K cryostat to improve their single-photon characteristics, as phonons are one of the dominant sources of dephasing and linewidth broadening [22].

2.1.1 Excitation Protocols

The emission of single photons depends on the excitation and decay of a two-level emitter. Therefore, the excitation trigger must be pulsed to ensure that only a single excitation occurs at any given moment. Typically, the pulse duration should be shorter than the lifetime of the QD, which is on the order of a nanosecond. Figure 2.3 demonstrates several

protocols for optically exciting the QD, each representing a trade-off between experimental complexity and performance.

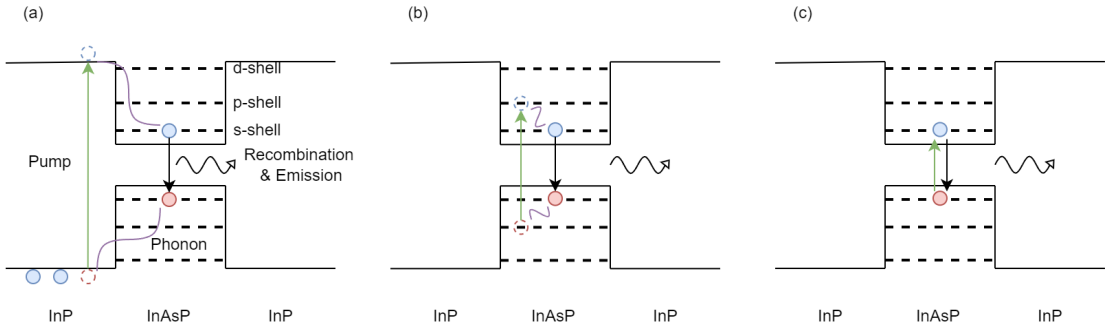


Figure 2.3: The optical excitation schemes for QDs. Blue (red) circles indicate an electron (hole), with dashed lines illustrating their respective transition paths. The excitation pump is denoted in green, and non-radiative relaxation processes, such as phonons, are depicted in purple. (a) Above band excitation. (b) Quasi-resonant excitation. (c) Resonant excitation.

Above-band excitation represents the simplest method, as the laser used to excite the QD can be of lower power, and the emission has a large frequency difference compared to the pump, facilitating easier filtering. The pump wavelength is selected to induce electron-hole pair generation in the surrounding semiconductor, which requires a wavelength below 830 nm in InP. These electron-hole pairs can migrate through the lattice via non-radiative processes (such as phonons) to reach the QD, where they recombine and emit photons. However, this simplicity comes at the cost of lower quality in almost every aspect of the single-photon emissions due to interference from the host material and a strong dependence on phonons, which often leads to dephasing [61].

Quasi-resonant excitation uses an excitation frequency that is lower in energy than the band gap of the surrounding material but higher than the energy required to reach the lowest excited level of the QD. For instance, the excitation might target the p-shell of the QD. Upon excitation, the QD quickly relaxes to the s-shell through phonons, facilitating the recombination of electron-hole pairs. This method mitigates some of the drawbacks associated with above-band excitation, as the charge carriers primarily interact within the QD region [22]. However, this approach requires higher excitation power, and filtering can be more challenging as the pump wavelength approaches the emission wavelength.

Resonant excitation takes it one step further by directly exciting the QDs into the s-shell. This technique yields the highest quality emission because it bypasses reliance on

phonon-assisted relaxation processes [61]. However, implementing this method is notably challenging compared to above-band and quasi-resonant excitation. It demands the highest pump power, and direct frequency filtering is not feasible.

In our lab we are still developing the QD single photon source in collaboration with Prof. M. E. Reimer and currently working with an above-band excitation scheme, as we still rely heavily on frequency filters to separate the excitation pump.

2.1.2 Gas Tuning

As discussed in Section 1.1.2, achieving an exact match between QD emissions and atomic transitions is nearly impossible. However, a viable approach involves initially finding a QD with emissions near the desired frequency and subsequently tuning these emissions to align with atomic resonance more precisely. An ideal tuning technique would be:

1. In-situ: Tunable without having to change the QD environment, such as removing the QD samples from the cryostat.
2. Precise: The tuning should be precise enough to interface with the atomic transitions, in the sub-GHz range.
3. Reversible: Ideally the wavelength can be tuned in both direction, or the process can be reversed such that the QD returns to it's original state.

Many options have been explored in the past for tuning QD emissions to align with atomic resonances. These include applying a magnetic field [62], thermal or laser annealing [63, 64], and employing stress-based mechanisms such as piezo-actuators or thin film deposition [65, 66, 67]. We use a custom tuning technique involving the controlled injection of nitrogen gas into the cryostat. More details on the setup can be found in Appendix A. In summary, the nitrogen gas deposits on the nanowires, and upon condensation, the lattice mismatch between nitrogen ice crystals and semiconductor materials induces stress on the QD, thereby shifting the emission wavelengths [68]. An example of the frequency shift from gas tuning is shown in Figure 2.4, where nitrogen gas was injected into the cryostat at a rate of 0.7 mln/min for up to 6 minutes. During the gas deposition, the frequency shift behaves linearly with respect to injected gas volume. As shown, this results in approximately a 9 pm/min shift across all three emission wavelengths for this QD, so by controlling the duration of the injection we can precisely control the frequency shift. The gas tuning effect can be reversed by heating and vaporizing the N2 ice on individual

QDs with a high-intensity focused laser. This technique is known as laser ablation. This process has also been demonstrated to be repeatable [42].

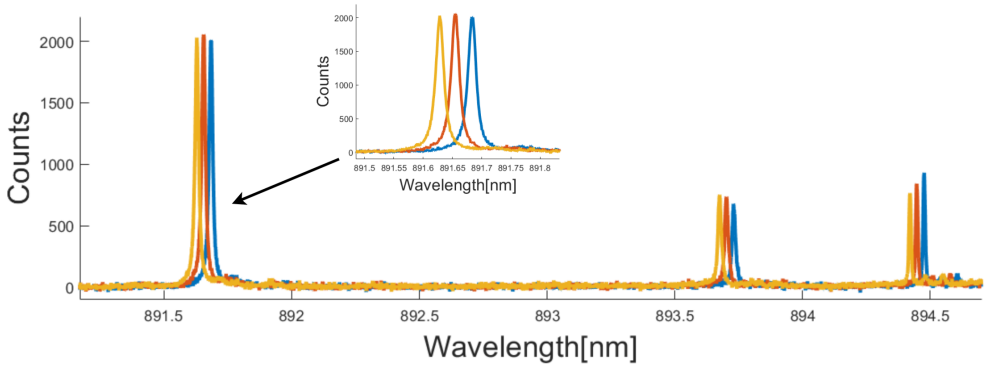


Figure 2.4: Frequency shift of X, XX and X^- by nitrogen gas deposition. For 0 min (blue), 3 min (red) and 6 min (orange) at 0.7 mln/min injection rate. Inset: a magnified view of the X frequency shift.

Another phenomenon of QD sources not yet mentioned is fine-structure splitting (FSS). So far, we have only considered an ideal scenario where there is no FSS. The energy levels depicted in Figure 2.2 also aren't entirely accurate for practical QDs. Due to inevitable asymmetries of the QD, the degeneracy of the the biexciton to exciton cascade can be lifted. This can be detrimental to the polarization entangled state as there is now also "which-path" information encoded in the emission frequency. This effect will be further explored in Chapter 3, but there are some potentially interesting interactions of FSS with the proposed gas deposition technique.

2.2 QD Experimental Setup

The experimental setup used to excite and couple the QD photons to single-mode fibers are shown in Figure 2.5. The QDs are held in a 4K closed-cycle cryostat by Montana Instruments, with the QD sample position adjustable via a piezo controller to focus on a single nanowire. There are two paths for light to reach the cryostat. Firstly, a larger continuous wave (CW) imaging light, typically from a Thorlabs SLS201 white light source, illuminates the sample to aid in visualizing movements between different QDs and alignment. This light is reflected off an Iridian FLD-708-DLP dichroic mirror (DM) before reaching the cryostat. Secondly, the beam used to excite the QD has a smaller beam waist and passes

through a neutral-density (ND) filter. It then reflects off a mirror and passes through the same DM used by the imaging light to reach the cryostat. The excitation beam is generated using either a PicoQuant PDL 800-B pulsed laser source or a continuous wave Titanium-sapphire laser (Ti:sapph), which can be modulated using an electro-optic modulator (EOM). Both beam powers are monitored continuously using a 90/10 beam sampler, ensuring the applied intensities on the dots are known at all times.

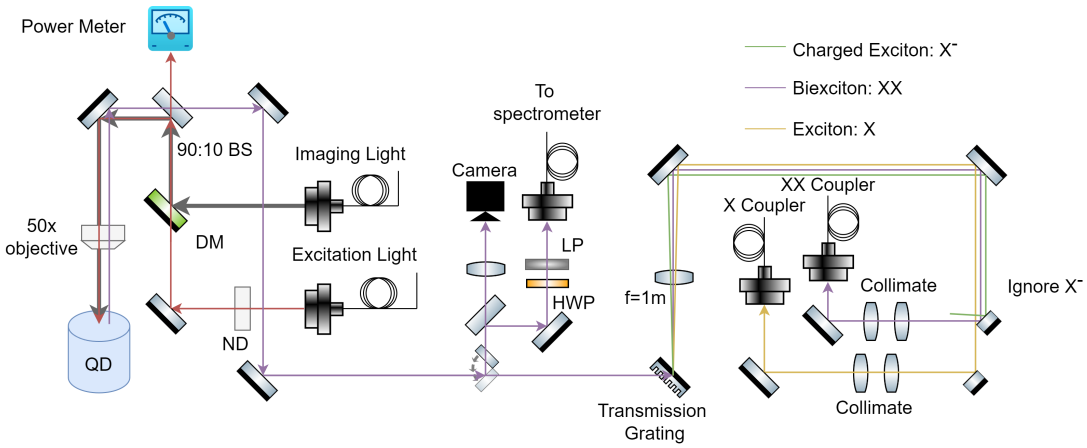


Figure 2.5: The experimental setup for the QD. The labeled optics are DM: dichroic mirror. 90:10BS: 10% beam sampler. ND: neutral density filter. HWP: Half-wave plate. LP: Linear polarizer. f: focal length of the lens. Collimate: a pair of lenses, along with a long focal length lens of 1 meter, expand and collimate the beams of excitons, biexcitons, and charged excitons before fiber coupling.

The reflection of the imaging beam and emission from the QD is directed back in the opposite direction, where most of the light passes through the beam sampler to the remaining optics used for characterizing and fiber-coupling QD emissions. A flip mount allows the beam to be directed towards a camera and a custom-made spectrometer. The camera assists in aligning the excitation beam onto the QD, providing visual feedback for alignment purposes. The spectrometer is used to characterize the emission spectrum from the QD and can be used in conjunction with the camera to optimize the coupling.

When the flip mount is removed from the beam path, the X, XX and X^- from the QD split on a LightSmyth T-1702-895 transmissive diffraction grating. These beams are then sent through a lens with a long focal length of 1 meter, allowing them to spatially separate further. Just before and after the 1-meter focal length, two small adjustable D-mirrors are positioned to reflect two out of the three emissions for fiber coupling. The exact position of

the focal length is about mid-way between the two adjustable mirrors, so two more lenses are placed to collimate and control the beams size. The two selected emissions are then fiber coupled into their respective fibers for further characterization or experiments. In the example shown in Figure 2.5, the emissions from the exciton and biexciton were chosen for coupling, while the emission from the charged exciton was discarded.

The custom-built spectrometer, based on the Czerny-Turner setup, is used to characterize the QD emissions, as shown in Figure 2.6. The input light is focused onto a slit and starts to diverge. It is then collimated by a concave mirror and strikes a diffraction grating, causing the frequency components of the beam to diverge. Our setup features a set of three gratings, each with a different groove number. By selecting different gratings, we can vary the resolution and total detection range of the spectrometer [69]. These gratings are mounted on a rotating base plate controlled by an Arduino, allowing for easy switching between gratings and adjustment of the angle of incidence. This flexibility enables precise tuning of the center wavelength measured by the spectrometer. After the grating, a second concave mirror focuses the different frequencies to specific spatial positions. The beams can then be directed either to a spectrometer, by reflecting off a removable mirror, or to a monochromator to serve as a frequency filter. The specifications and applications of the monochromator are discussed further in Appendix F, but for now, we will focus on the spectrometer function. The focal position on the camera is wavelength-dependent. By calibrating the spectrometer, the intensity profile of the spectral lines captured by the camera can be used to determine the frequency spectrum of the beam. With a high-resolution ZWO ASI 1600-MM camera and the 1800/mm grating, we achieve a resolution of about 0.6 GHz/pixel.

2.3 Excitation Pulse Generation

To achieve single photon emissions, it is essential to excite the QD with pulses shorter than its lifetime, typically on the order of nanoseconds. we set an initial target of around 100 picoseconds pulse widths and an extinction ratio of 30 dB. This can often and easily be achieved with a pulsed Ti:sapph laser, but we are not equipped with one in our lab and they can be a heavy investment for just this single purpose. Alternatively there are many commercially available pulsed lasers that can be used, but often do not have the wavelength range to switch between above-band and resonant excitation. An alternative approach we are exploring involves pulsing a CW laser using an EOM. EOMs are well known for their rapid switching speeds in telecommunications, and their broad bandwidth makes them suitable for our purposes as well. The modular nature of EOMs facilitates

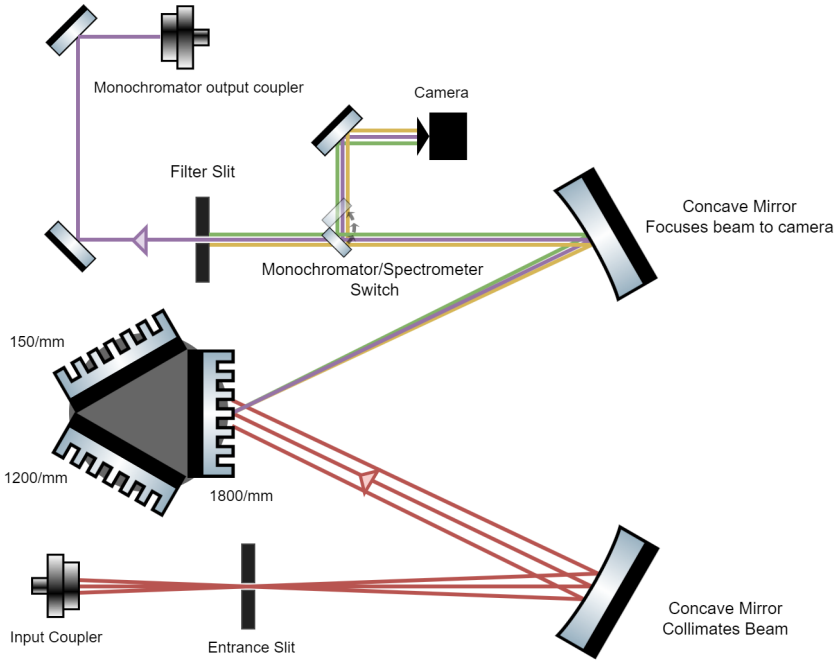


Figure 2.6: The spectrometer/monochromator setup. The spectrometer was built based on a Czerny-Turner setup. Note the schematic lines depicting the optics path do not fully represent the actual divergence and focusing of frequencies typical in a Czerny-Turner spectrometer. In reality, there is a more intricate process of collimation and divergence following the diffraction grating. However, for clarity, the diagram illustrates primarily the spatial separation of different frequency components subsequent to the grating.

their compatibility with a wide range of CW lasers, mimicking the tunability of a Ti:sapph. This versatility allows us to conduct both above-band and resonant excitations effectively. To gain a deeper understanding, let us delve into the operational principles of an EOM.

The EOM intensity modulator we use is similar to a Mach-Zehnder interferomter shown in Figure 2.7(a). To begin, an incident field is split into two paths, often referred to as "arms" by a 50:50 beam splitter. As the individual beams travel down their respective path, they accumulate phase based on their optical path length[2] and reflections. Eventually, the two beams recombine at another 50:50 beam splitter where they interfere. Based on the accumulated phase difference between the two arms, their interference can lead to constructive or destructive interference, leading to measurable power variations at the

[2]The optical path length (OPL) is defined by OPL = nL, where n is the refractive index and L is the geometric length of the medium.

photodetector outputs. The modulation of power entering a specific detector is achieved by adjusting the optical path length of one of the arms. This mechanism also forms the basis of a Mach-Zehnder based EOM as depicted in Figure 2.7(b). Here, an input beam is split into two paths within the EOM, which then recombine. By altering the optical path length of one arm, we can control the output power. The optical path length of EOMs can be electrically tuned due to their construction from nonlinear crystals such as lithium niobate, which possess a strong second-order susceptibility. This property makes the refractive index highly responsive to external electric fields. The resulting sinusoidal relationship between the applied voltage and output intensity of the EOM is shown in Figure 2.7(c). In realistic implementations of the EOM, it is nearly impossible to achieve perfect destructive interference and leads to some leakage of power at the minimum point. For instance, the iXblue NIR-MX800 EOM in our lab leaks about 1 μW when 20 mW is coupled in with just a DC input. The voltage required to shift between the minimum power and maximum power is known as the half-wave voltage V_π, which strictly defines the voltage required to induce a π phase shift between the two arms. We typically observe a 15-20% coupling efficiency. Here, the coupling efficiency is defined as the ratio of the maximum EOM output power to the fiber-coupled input power to the EOM.

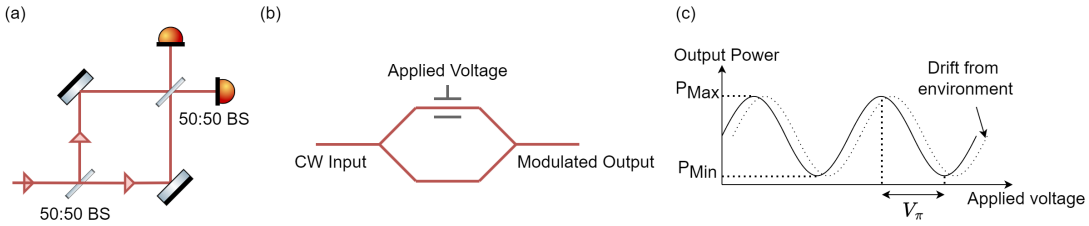


Figure 2.7: (a) The typical setup for a Mach-Zehnder interferometer. (b) Diagram of EOM as just one output arm of the Mach-Zehnder interferometer. By applying a modulated voltage to one path, an electric field is induced in the non-linear crystal, modulating the phase difference between the two paths. This modulation results in intensity variations due to destructive interference. (c) Intensity modulation of output beam as a function of applied voltage. The half-wave voltage V_π is the voltage required to change from the minimum intensity to maximum intensity. The dotted line illustrates the intensity function's variation with voltage due to fluctuations in the EOM's surrounding conditions.

To generate high-contrast pulses, EOMs feature a DC port for setting the bias voltage V_b to the voltage corresponding to minimum power, and an RF port for inputting modulated electrical pulses V_m. The total applied voltage is then the sum of the two signals $V = V_b + V_m$. One inevitable downside of using an optical modulator is that they are prone

to drifting over time due to variations in the input and surrounding environment, such as temperature [70]. In order to guarantee consistent, high-contrast pulses, it is essential to adjust the bias voltage to compensate for shifts in the intensity modulation curve, as depicted by the dotted plot in Figure 2.7(c). This adjustment is particularly critical for applications involving the excitation of single-photon sources. If initially the bias was set such that P_{min} was minimized, but over time the response curve of the EOM shifts, the EOM may now be consistently leaking $\sim \mu$W levels of light. Consequently, this results in low-power continuous excitation of the QD, leading to weak continuous fluorescence, which contradicts our goal of achieving a single-photon source. These devices that adjust V_b are known as bias controllers, and there are many commercially available options, although they are often expensive. We have built a custom bias controller and describe its operation more in Section 2.3.1. Another perhaps more obvious circuit required to create pulses are the electronic pulse generators that the EOM then transduces to optical pulses. While pulses on the order of ∼10 ns may be achieved on standard arbitrary function generators, pulses on the 10-100 ps scale require more custom electronics. To meet this need, we have create our own ps electronic pulse generator based on step recovery diodes (SRD) [1]. The implementation of the pulse generator is discussed in Section 2.3.2. Together, these two circuits create the stabilized and modulated laser pulses we use for the QD and other pulsed laser applications such as the EIT memory in Chapter 5. Such a modular setup for the EOM is shown in Figure 2.8.

2.3.1 The Digital Bias Controller

Bias controllers can be challenging to create and often rely on an inherently complex process based on signal mixing. Bias controllers based on signal mixing were also attempted in our lab but encountered some issues [71]. One major challenge was an offset in the mixer that proved difficult to control, resulting in imprecise stabilization. Additionally, the mixer filtered out significant information, making the process unnecessarily complex. To address these issues, we proposed a new bias controller that uses only DC signals to stabilize the drift from the EOM. A block diagram of the circuit is shown in Figure 2.9(a).

The circuit operates exclusively within the digital signals by comparing a square wave dither, incorporated into the DC correction, with the phase of the EOM response detected through a high-gain photodetector. When a square wave dither is applied to the DC signal at minimum bias voltage, the output intensity remains unchanged or shows minimal oscillation due to the dither's small amplitude. However, drifting to the right of the minimum bias causes the square dither to induce oscillations in the output intensity due to the increased slope of the power function. The response becomes in phase with the

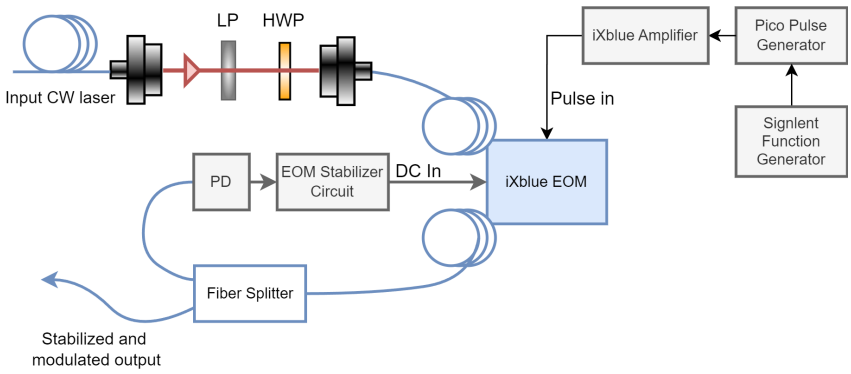
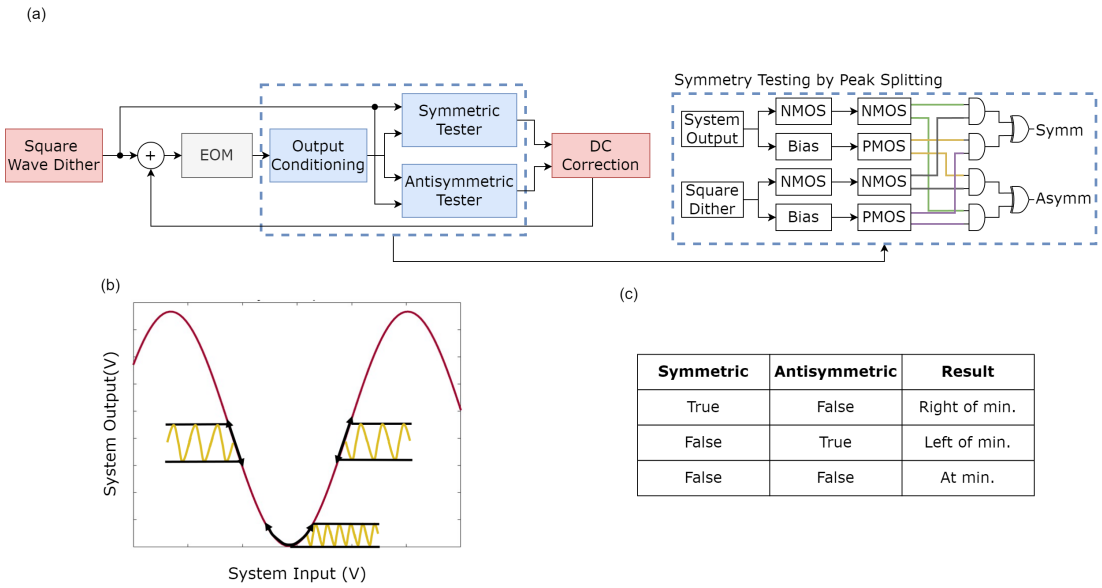


Figure 2.8: The EOM and it's supporting electrical equipment to convert a continuous laser input into a stabilized and amplitude-modulated output. The EOM stabilizer circuit is used at the DC input to the EOM, while the pulse generator circuit is triggered by a step voltage from a Siglent SDG6022x function generator. The repetition rate of the step-voltage determines the repetition rate of the pulses. The signal is then amplified by a iXblue NIR-MX800 amplifier to create the electronic pulses and fed into the RF input to the EOM. The fiber splitter and Thorlabs PDA100A2 photodetector (PD) are used to pick-off the EOM output for the bias controller.

dither because of the positive slope. Conversely, drifting to the left of the minimum bias results in output intensity oscillations perfectly out of phase with the dither due to the negative slope. Symmetric (in phase) or antisymmetric (out of phase) responses between the dither and the EOM output determine bias voltage correction. An Arduino processes the symmetry testing logic and adjusts the bias voltage using a digital-to-analog converter (DAC). The corrected bias voltage and dither are then applied to the EOM's DC input port through a summing amplifier. Figure 2.9(c) illustrates these responses along with their corresponding logic table.

This circuit was designed, soldered, and assembled into the small enclosure shown in Figure 2.10(a), which is the currently used setup for two EOMs in the lab. More documentation covering the circuitry, software code, and enclosure details can be found in Appendix B. The performance of the bias controller is demonstrated in Figure 2.10(b). When no bias controller is used for a 10 mW, 895 nm CW laser, the EOM steadily drifts from 296 nW to 1349 nW over the course of only 30 minutes. In comparison, with the bias controller turned on, the drift is limited to between 304 nW and 325 nW, significantly suppressing drift. Despite efforts to minimize drift, practical realizations of EOMs, such as trapped charges in the crystal and fabrication imperfections, prevent the minimum power



Symmetric	Antisymmetric	Result
True	False	Right of min.
False	True	Left of min.
False	False	At min.

Figure 2.9: (a) Block diagram of the circuit. A known square wave dither is applied to the DC port of the EOM. The dither is then compared against the output of the EOM to determine whether the output is symmetric (in-phase) or antisymmetric (180° out of phase). Symmetry testing is done using a series of NMOS and PMOS transistors, along with AND and XOR logic gates. (b) The effect of a small dither on the EOM response curve. If we are to the right of the minimum, the system response will be in-phase with the dither due to the positive slope. If we are to the left of the minimum, the system response will be out of phase with the dither due to the negative slope. (c) A logic table summarizing the adjustments to DC correction based on symmetry testing logic.

from perfectly reaching zero [70].

The true minimum power at about 290 nW was determined by manually adjusting the bias voltage using a DC power supply for the same input beam shown in Figure 2.10(b). Therefore, the minimum power of the bias-stabilized EOM is 5% higher than the true minimum, likely due to the added dither. Adjusting to a smaller dither could potentially reduce this discrepancy and bring the output power closer to the true minimum, but this often comes with a trade-off of lock stability, as the error signal is more difficult to detect.

This type of bias controller is specifically suitable for small duty-cycle pulses. Essentially, the Arduino's response time is slow enough that it primarily detects the EOM's off-state, enabling continuous correction towards the minimum power level. In compar-

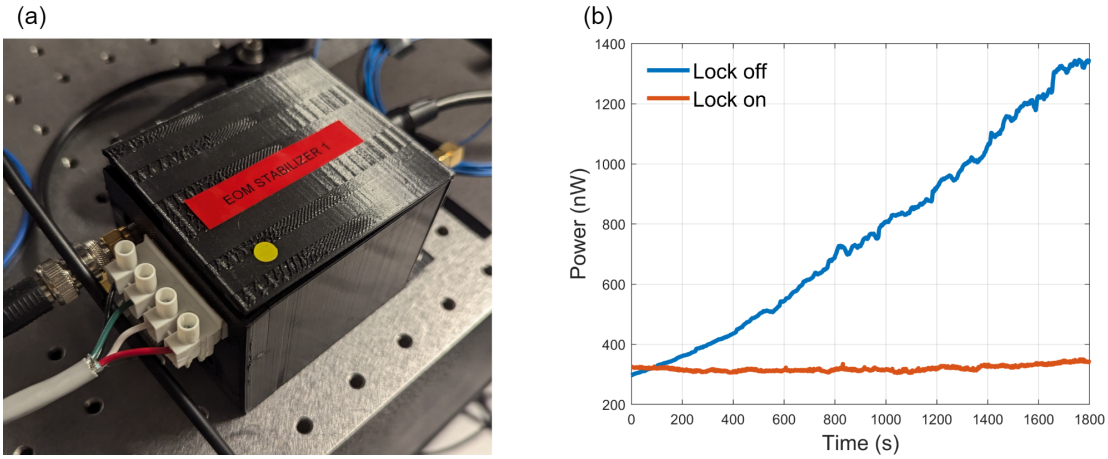


Figure 2.10: (a) Fully assembled EOM bias controller. (b) Drift in EOM output intensity for an 895 nm CW laser at 10 mW with no pulse trigger. Comparison between when the bias controller is turned off (blue) vs. on (red).

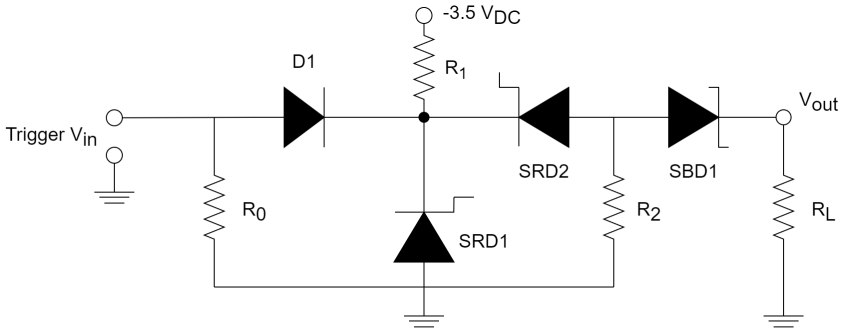
ison, our objective is to achieve 100 ps optical pulses within much longer experimental cycles.

2.3.2 The Picosecond Pulse Generator

The pulse generator we received and tested is an attempted replica of that from Zou et al. [1]. The circuit exploits the brief delay period during which PN junctions neutralize charges in the depletion region upon transitioning from forward to reverse bias. This interval, characterized by charge neutralization, is commonly referred to as the storage phase. During this phase, there is a significant influx of current, which researchers, including those in the work by Zou et al. [1], have found ways to harness for creating ultra-short pulses. Step recovery diodes (SRD) take this one step further, as they are diodes carefully designed to enhance this effect.

A copy of the circuit diagram is presented in Figure 2.11. D1 is a typical PIN diode that is always forward biased (ON) and protects the SRDs from a negative input voltage. SRD1 and SRD2 are the main components for triggering the pulse at the output, and SBD1 is a Schottky diode used for a pulse forming switch. Pulse formation is achieved by sending a step voltage at the input V_{in}, which causes the various SRDs in the circuit to switch biases at slightly delayed times due to the different resistances they have in their

paths. Specifically, due to the extra resistor $R2$, SRD2 enters the storage phase slightly delayed from SRD1. Later on, this causes an ultra-short period in time where SRD1 will be in the off-state, but SRD2 is still in the storage phase. SRD2 then induces a large influx of current and creates a pulse at V_{out}. By changing $R2$ to different resistances, the time delay between SRD1 and SRD2 entering the storage phase can be modified, and therefore the pulse length can also be modified. Tests of various resistor values and input pulses are summarized in Appendix C to create a reference table for the desired pulse outputs. The table underneath Figure 2.11 is used to indicate the various diode timings with respect to an input trigger.



Pulse!

	$t < t_1$	$t_1 < t < t_2$	$t_2 < t < t_3$	$t_3 < t < t_4$	$t > t_4$
V_{in}	~0 V	Increasing	Increasing	Slows down	At peak voltage
SRD1	Forward biased	Storage phase	Storage phase	Off	Off
SRD2	Forward biased	Forward biased	Storage phase	Storage phase	Off
SBD1	Off (V_{out}=0)	Off (V_{out}=0)	Off (V_{out}=0)	On	Off (V_{out}=0)

Figure 2.11: Pulse generation circuit designed by Zou et al. [1]. D1: PIN diode. SRD1, SRD2: step recovery diodes. SBD1: Schottky diode. R_L: Load resistor for output. Table: indicates the state of each SRD upon application of a step voltage V_{in}. Timing is with respect to an arbitrary time t. The references t_i denote each diode's phase change during its transition from forward to reverse bias.

2.4 Results

The resulting EOM pulses generated with the bias controller and pulse generator were first characterized on a Newport 1544 fast photodetector before being used to excite the

QD. One of the most optimized pulse shapes is shown in Figure 2.12(a). The 12 GHz fast photodetector enabled the observation of nearly 100 ps optical pulses, while measurements with superconducting nanowire single-photon detectors (SNSPD) indicated an extinction ratio of 31.5 dB.

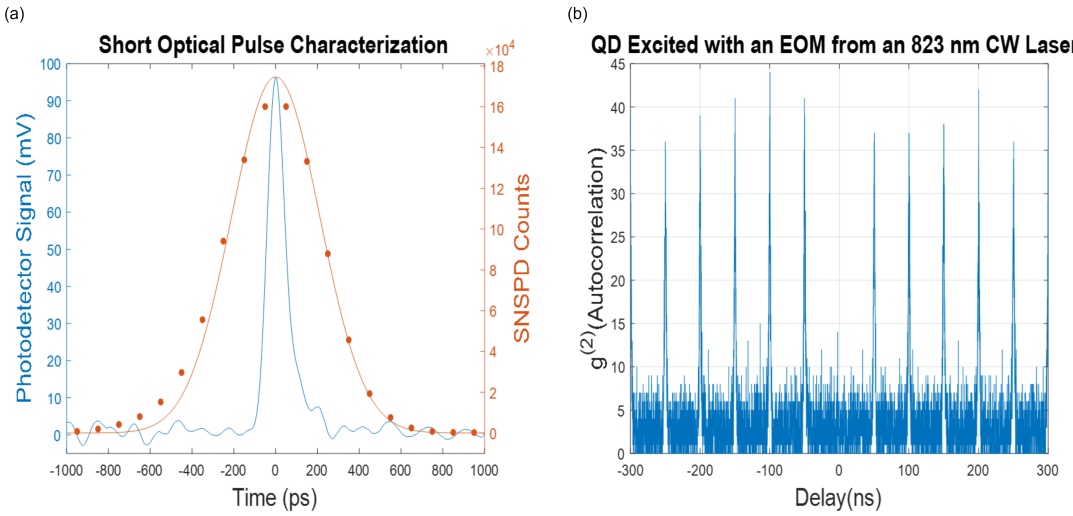


Figure 2.12: (a) Short optical pulse characterization of EOM with the custom-made bias controller and picosecond pulse generator. As the SNSPDs measurements (orange) also introduce an electronic time jitter of about 70 ns, the same pulse was measured on a 12 GHz fast photodetector (blue) to more accurately gauge the pulse widths. (b) $g^{(2)}$ of the QD biexciton emissions excited by the EOM.

As the pulses approach the initial target values in terms of both pulse length and extinction ratio, they were sent to the QDs, and the $g^{(2)}$ of the biexciton emission was characterized on SNSPDs. Initially, a 10 mW CW input was fed to the EOM, it was then attenuated and a pulsed beam with an average power on the order of nW was sent to the cryostat. As shown in Figure 2.12(b), we observe $g^{(2)}(0) = 0.095 \pm 0.0082$. While this value is about 1-1.5 orders of magnitude higher compared to some similar QD sources, we are performing above-band excitation, and 100 ps pulses are still relatively long and can excite the QD multiple times. In comparison, pulses on the order of $\sim$ 10 ps are often used in literature. To further reduce $g^{(2)}(0)$, we could also use even shorter pulses. The NIR-MX800-LN-20 EOM, with its 25 GHz max bandwidth, can achieve shorter pulses. However, the primary limitation remains the control electronics. Nevertheless, it meets a common minimum criterion of $g^{(2)}(0) < 0.1$ for a "good" single photon source.

In summary, we have demonstrated a simple bias controller circuit and pulse generator

that creates consistent short optical pulses using an EOM. The pulses derived from the EOM were able to generate single photons from QDs, as demonstrated by the second-order correlation measurement. The described setup achieves a cost-effective, modular, and scalable alternative to tunable pulsed lasers. The bias stabilizer is also used to create pulses in the EIT memory experiment in Chapter 5.

Chapter 3

Measurements of Fine Structure Splitting in Nanowire Quantum Dots

This chapter aims to further investigate the tuning of various QDs by gas injection. Of particular interest is determining whether the strain caused by gas injection can be regulated to control the FSS. In order to understand this hypothesis better, we will begin by providing a detailed description of FSS.

3.1 Fine Structure Splitting

As mentioned previously, the energy levels in Figure 2.2 describe a symmetric QD where there is no FSS present. However, in reality, the degeneracy of the intermediate X states is lifted due to asymmetry of the QDs, either geometrical or electrical [72]. A more realistic cascaded energy level diagram is shown in Figure 3.1.

The FSS energy difference leads to a phase change in the expected state output in the form of $\frac{1}{\sqrt{2}}(|HH\rangle + e^{i\tau\delta/\hbar}|VV\rangle)$, where δ is the FSS energy[1], and τ is the time between the XX and X decays. Based on the FSS, the resulting state can oscillate between two bell states $|\Phi^+\rangle = \frac{1}{\sqrt{2}}(|HH\rangle + |VV\rangle)$ and $|\Phi^-\rangle = \frac{1}{\sqrt{2}}(|HH\rangle - |VV\rangle)$, which makes it a much less ideal output for an entangled two-photon source [73].

[1]Specifically, $\delta = |H\rangle$ XX Energy $- |V\rangle$ XX Energy, so the energy of the horizontally polarized biexciton subtracted by the energy of the vertically polarized biexciton.

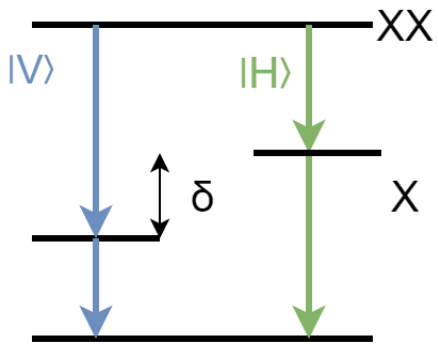


Figure 3.1: Energy levels for a biexciton-exciton cascade, the separation of the excition energy levels are known as the FSS energy(δ).

Many sources of FSS arise from a physical asymmetry during the fabrication process, such as differences in radial confinements from varying fabrication sizes, uneven alloy distributions, and strain [74]. Despite advancements in QD fabrication techniques, achieving a perfectly symmetrical QD to completely eliminate δ is nearly impossible in practical scenarios. Therefore, there must be a way to combat FSS post-fabrication, and one promising method of interest involves applying stress [75, 76]. As mentioned in section 2.1.2, the underlying mechanism for our wavelength tuning is by applying a stress to the QD. So it would be interesting if the same stress that induces a frequency shift in the QD emission can also influence FSS, and by unevenly melting parts of the deposited nitrogen, we aim to gain some sort of control over the asymmetry and FSS.

Another point of study is observed during gas tuning. The X, XX and X^- emission frequencies shift by the same amount within a single QD. But, different QDs exhibit varying rates of frequency change. This variation in frequency change could potentially indicate how responsive a QD is to applied strain, and by extension, how tunable its FSS is under strain. Such statistical measurements of 16 QDs are conducted and analyzed in the subsequent section of this chapter.

3.2 FSS Measurement of 16 QDs

The FSS of the QDs are measured by placing a Foctek WPC212H HWP and Thorlabs LPNIRE100-B polarizer before the fiber coupler to the spectrometer, this section is shown by the red arrow in Figure 3.2. By rotating the HWP by 45 degrees, we rotate the measured

polarization states of light emitted in the biexciton-exciton cascade between $|H\rangle$ and $|V\rangle$. Then the two polarizations are individually collected on the spectrometer, and a sample output of the non-degenerate energy levels of the XX and X are shown in Figure 3.3. The sign of the FSS can then be obtained by converting the peak frequencies of the XX and X in both $|H\rangle$ and $|V\rangle$ polarizations (as observed in Figure 3.3) into energy and subtracting them as described in section 3.1.

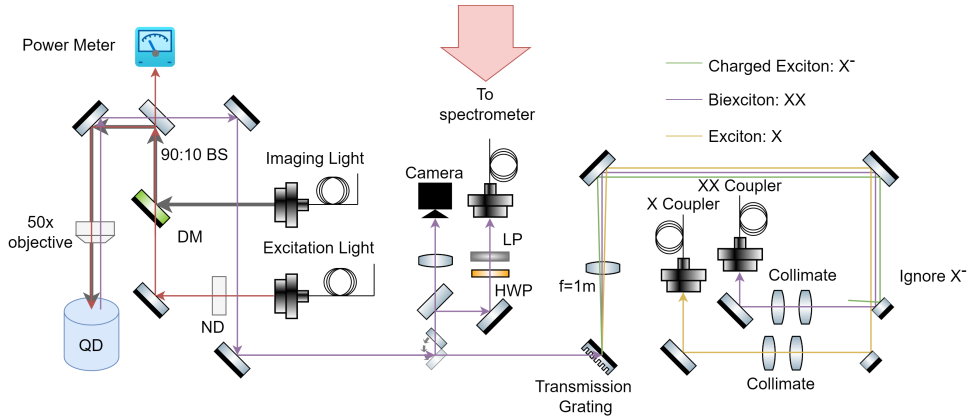


Figure 3.2: Same diagram as Figure 2.5, but with an arrow to help identify the fiber coupler to the spectrometer, the HWP, and the polarizer.

Instead of using the HWP at just two angles separated by 45 degrees to obtain the horizontal and vertical polarizations, we now rotate the HWP between 0 and 90 degrees. We expect to observe a single oscillation period in the peak frequency as the QD transitions between its two energy paths in the cascade. This process was automated by taking spectrum measurements at 5-degree intervals of HWP rotation with a Thorlabs ELL14 - rotation mount controlled by the spectrometer GUI. This automation was directly set up in the spectrometer GUI under the 'save spectrum' function, where the user can specify the number of images and the total rotation angle. The peak frequency was recorded for each polarization angle, resulting in a sinusoidal relationship as the system alternates between the two decay pathways. An example series of these measurements is illustrated in Figure 3.4(a). At each polarization angle, the energy differences were used to construct a sinusoidal curve, where the amplitude represents the fine-structure splitting (FSS) energy δ [58]. For the QD shown in Figure 3.3, it was seen to have $\delta \approx 5\mu eV$ as shown by Figure 3.4(b).

Such FSS measurements were performed over 16 QDs with emission wavelengths near the Cs D1 line. Each QD's FSS was measured at six stages of gas tuning, starting from

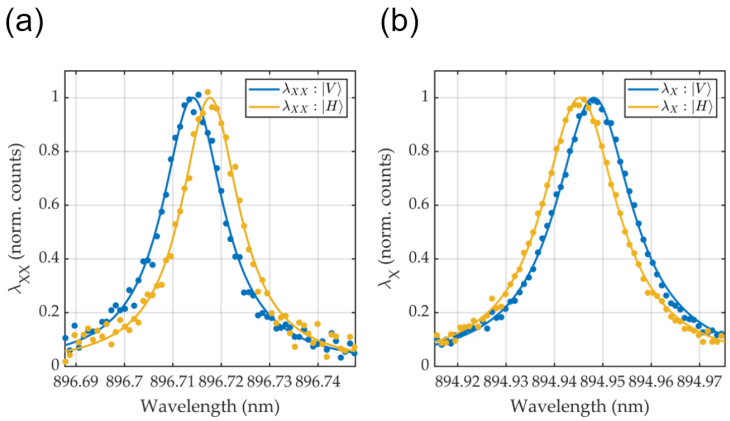


Figure 3.3: Frequency shift of XX (a) and X (b) due to FSS. The vertical (blue) and horizontal (yellow) polarizations indicate the energy difference between the two paths in the cascaded energy levels.

0 min (no deposition), and up to 30 min of deposition with six-minute increments at a nitrogen flow volume of 0.7 mln/min. The raw data for each QD's initial FSS is logged in Appendix D. As mentioned previously, our interest lies in understanding the relationship between gas tuning and changes in FSS under applied stress. The results of the frequency shift plotted against the FSS are depicted in Figure 3.5. From the data, for some QDs there is $\sim \mu eV$ change for more than 100 GHz of tuning. Although no clear relationship emerges between frequency shift and FSS, there exist NW QDs for which the gas tuning reduces FSS. Thus there is realistic potential that there may exist QDs for which FSS can be suppressed with the gas deposition. While this does not work for all QDs, one can just select a QD from the many in the chip that can have its FSS suppressed to near zero. Unfortunately, the spectrometer has a resolution of 0.6 GHz, so the noise of the measurement and FSS change are both on the order of $\sim \mu eV$. One particularly interesting quantum dot is QD(78,6) shown in more detail in Figure 3.6, as FSS appears to have been reduced by gas deposition from 3 μeV to about 1.5 μeV. This suggests that it may still be possible to find an ideal quantum dot with near-zero FSS, then the FSS can be further reduced by gas deposition.

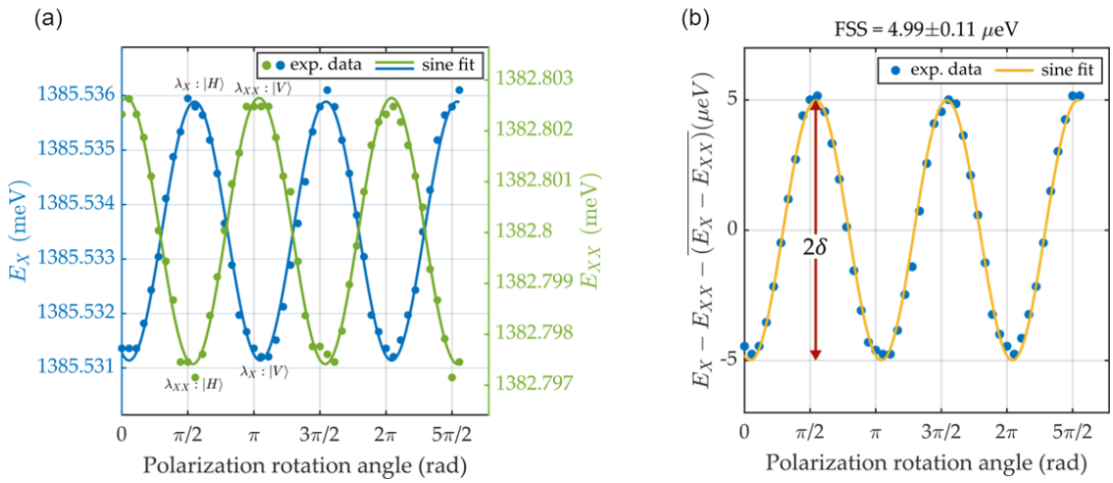


Figure 3.4: (a) Energy of XX (green) and X (blue) peak centers as the HWP is rotated to switch between the H and V paths of the energy cascade. (b) The centered energy level difference between the X and XX, creating a sinusoidal function with an amplitude of δ.

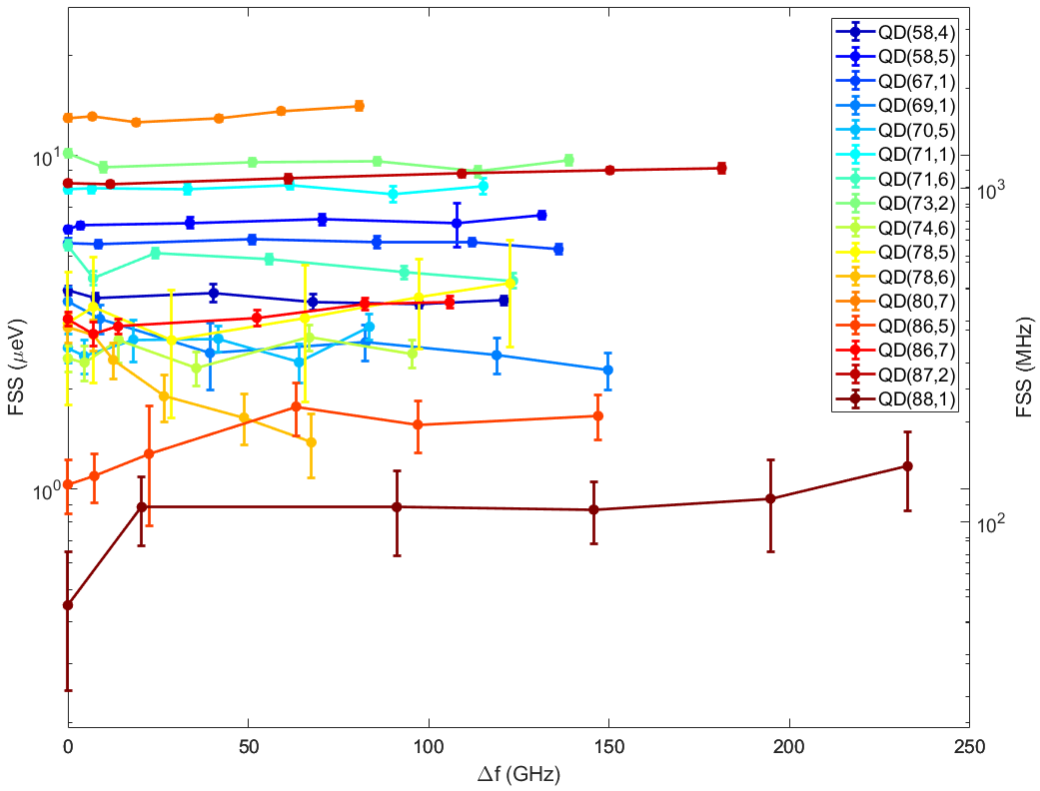


Figure 3.5: Frequency shift induced by gas deposition vs. FSS of 16 QDs. Raw data can be found in Table D.1 and Table D.2. A more detailed view of QD (88,1) and QD (78,6) is also provided in Figure 3.6.

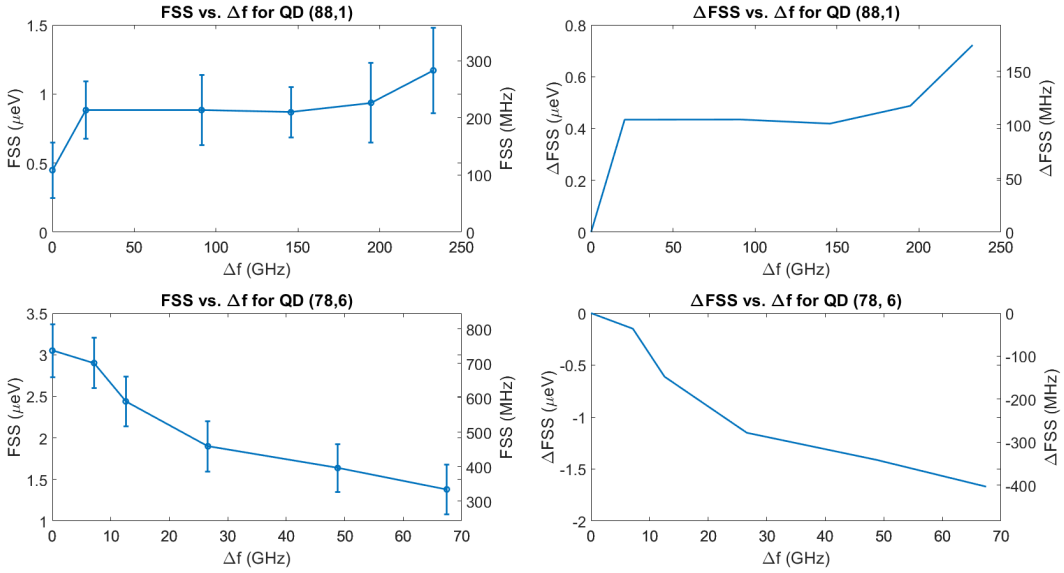


Figure 3.6: Detailed FSS data of QD(88,1) and QD(78,6) illustrating both the exact FSS change and ΔFSS from it's initial value as gas is deposited.

To investigate the control of FSS through asymmetric nitrogen deposition, we initially deposited nitrogen assumed to uniformly cover the nanowire. Subsequently, a 910 nm high-intensity melting beam was purposely positioned off-center of the nanowire, heating only one side. We conducted eight trials with varying beam positions for durations ranging from 1 to 5 minutes and powers up to 1 mW. The relative placements are illustrated in Figure 3.7. Despite cumulative exposures of up to 30 minutes at 1 mW, no observable change in FSS due to asymmetric melting was detected across any of the tested QDs.

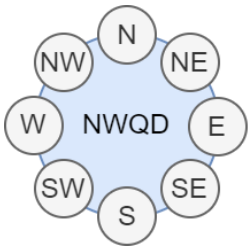


Figure 3.7: Positions of the melting beam on the NWQD, represented by the gray circles at 8 positions based on NEWS co-ordinates.

In summary, based on the study of 16 QDs, it may be possible to find a QD with a small FSS, such that gas tuning could reduce the FSS to zero.

Chapter 4

Miniaturized Laser Locking

A unique feature of lasers has always been the narrow linewidth achieved through stimulated emission. Through careful design, the emission wavelength can be engineered around a specific frequency with an external resonator or grating. However, without additional controls, the laser's central frequency is known to drift over time due to variations in temperature, current, and mechanical vibrations. In frequency-selective applications such as atomic physics, there must be a way to maintain the central frequency within the narrow MHz linewidths of atomic transitions. To achieve this frequency stability, the laser's emission is typically compared against an external reference to create an error signal used in the stabilizing feedback loop for the laser. Common frequency references include Fabry–Pérot cavities, frequency combs, or other stabilized lasers. Often, the atomic transitions observed in room-temperature vapor cells serve as the perfect frequency reference to lock lasers.

A common practice for locking lasers corresponding to ground state transitions is to measure the transmission of a probe through a vapor cell. Although the transmission dip is broadened by Doppler broadening, numerous techniques such as saturation absorption spectroscopy [55] or dichroic atomic vapor laser locks (DAVLL), have been developed to lock onto the precise atomic transition with high degrees of stability [52, 77]. Locking between two upper states, is more challenging as it involves attempting to lock onto an empty transition. Some methods involve observing the absorption after optical pumping, or more complex multi-photon interactions, such as two-photon absorption, EIT, or electromagnetically induced absorption (EIA) [78, 79]. In this project, we build upon the two-photon DAVLL (T-P DAVLL) technique developed by Becerra et al [52], which combines the dichroic atomic vapor laser lock and EIT signals to achieve a Doppler-free and low-power method to lock between two upper states of an atom.

For some atomic experiments such as FWM, one may need multiple lasers locked to different atomic transitions which has traditionally been implemented using free-space setups built directly on the optics table. The drawback of this is that the optical setups consume a significant amount of space and as such there has been a recent interest in miniaturizing laser locking setups. While a saturation absorption spectroscopy setup could be implemented on photonic chips [80], DAVLLs have not yet been implemented in this manner due to drawbacks related to efficiency and the complexity of the design and fabrication process. Miniaturization of free-space optics can also be achieved through custom machining of metallic boards, but managing modifications and revisions to these boards can become challenging, and mistakes may require hours of reworking. Another increasingly popular option, thanks to advancements in 3D printing technology, is to fully 3D print structures to replace traditionally bulky setups, such as the 3D printed cooling and locking optics designed by Madkhaly et al. [81].

In this chapter, we show the use of a 3D printed push-fit style board to mount optical components for a T-P DAVLL to stabilize laser frequencies between two excited atomic states using Cs vapor. The push-fit board is pre-aligned to directly mount optical components near their optimal positions to save costs on traditional mounting posts and decrease its overall footprint. Each slot on the push-fit board is carefully designed to maintain strong alignment while also not impeding too much stress on the active areas. The push-fit board is printed with PLA on an Anycubic 3D printer.

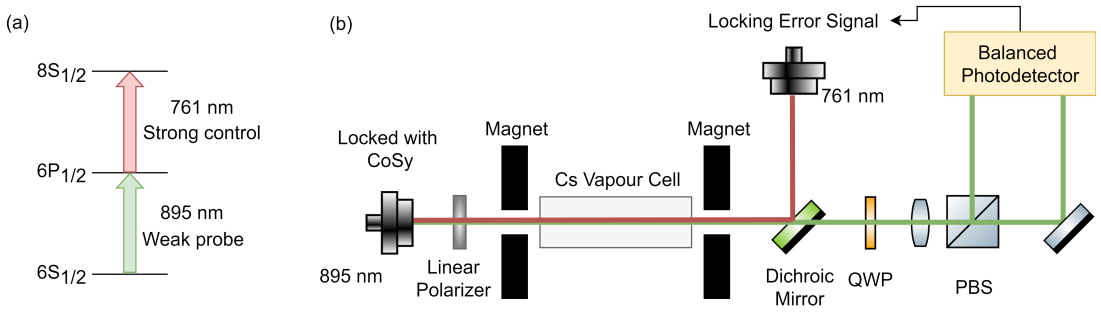


Figure 4.1: (a) Three energy levels of the Cs atom forming a ladder system. (b) Experimental diagram of the T-P DAVLL. By monitoring the transmission of the 895 nm probe, an error signal is created to lock the 761 nm laser.

4.1 Principle and Design

The error signal from the vapor cell is created by an EIT signal in a ladder scheme shown in Figure 4.1(a). In the presence of a magnetic field, a weak probe resonant between the $6S_{1/2}$ and $6P_{1/2}$ states of Cs is overlapped with a counter-propagating control beam between the $6P_{1/2}$ and $8S_{1/2}$ states. The absorption experienced by the probe's orthogonal polarizations are subtracted from each other to create the error signal. Finally, we discuss the lock stability of the push-fit board by monitoring the EIT signal over an extended duration of time. The proposed 3D printed push-fit board offers an inexpensive, scalable, and highly customizable approach to achieving a modulation-free locking scheme between two upper atomic transitions by the T-P DAVLL.

The basic optical setup of the T-P DAVLL using EIT is shown in Figure 4.1(b). The 895 nm laser is locked with a commercially available compact saturation spectroscopy module from Toptica known as the CoSy. A weak, locked 895 nm probe will experience an increase in transmission when in the presence of a strong, counter-propagating control at 761 nm. Due to the magnetic field generated by two permanent magnets, the degeneracy of the states is lifted, and the two orthogonal circular probe polarizations will experience a slightly shifted resonance based on the strength of the magnetic fields. The orthogonal probe polarizations are then split by a quarter-wave plate and polarizing beam splitter, and their amplitudes are subtracted on a Koheron PDX10B-80-DC-SI balanced photodiode to generate an error signal with a zero-crossing for side-of-fringe locking. Finally, a LA1289-B 30mm focal length lens from Thorlabs is used to focus the beam onto the small 0.6 mm diameter photodetectors. The typical error signal and lock points observed on the laser control boxes is shown in Figure 4.2.



Figure 4.2: Typical error signals for the T-P DAVLL signal (Left) and compact saturation spectroscopy setup (Right). As seen on the Toptica DLC Pro control box.

To save space, we use half-inch optics for all components. The fully mounted push-fit board is shown in Figure 4.3(a). As smaller beam diameters require less power, the 895 nm

and 761 nm beams pick off 0.8 mW with a 0.75 mm beam diameter and 7 mW with a 1.5 mm beam diameter respectively. Two small permanent magnets, each with a 12 mm diameter and a center opening, were placed before and after the Cs cell to create the magnetic field. All the components on the board were designed to have the beam pass through the center of the active area. The goal is to place as many components in pre-aligned slots as possible, such as the beam splitter and waveplates. This is achieved by designing small push-fit slots with a 0.01" tolerance on each side to maintain a secure grip on the components without imposing too much stress on the parts. The active areas and edges are given extra space to prevent damage to the optical components as shown in Figure 4.3(b) and Figure 4.3(c). The Thorlabs KM05 mirror mounts and Focktek WPO212Q quarter waveplates have the base height and position of their fasteners adjusted to center the beam. The beam path is guided by a semi-circular groove. Intermediate test points, such as slots for IR cards and small circular openings to mimic apertures are shown in Figure 4.3(c), these help guide the alignment of the 895 nm beam. Only the fiber inputs and Thorlabs DMLP805T/DMSP1000T dichroic mirrors are mounted on adjustable half-inch mirror mounts. The mirror mounts are pushed against a ledge to provide coarse guidance, while fine tuning is achieved with the adjustment screws. The 895 nm mount allows for better alignment of both beams to hit their respective 0.6 mm diameter photodiodes, while the 761 nm input and dichroic mirror mounts provide 2 degrees of freedom to better overlap the probe and control fields. For now, we avoid the use of epoxy and instead mounted the fiber inputs in kinematic mounts. More details on the dimensions of the board and design can be found in Appendix E.

4.2 Lock Stability

While current noise and vibrations may occur on the order of microseconds, the effects of environmental temperature and air pressure may manifest over minutes, leading to a central frequency drift. Ideally, the lock would stabilize the frequency indefinitely; however, more realistically, we aim for reliable locking over the course of many experimental cycles. In a similar but separate EIT setup shown in Figure 4.4(c), we lock the 761 DAVLL with a PID from the DLC Toptica control box, and we measure the central frequency stability of the T-P DAVLL over an extended duration by monitoring the EIT signal of a different probe. In the T-P DAVLL, the $6S_{1/2}, F = 4$ state is used as the ground state for the probe. In the lock stability experiment, a different 895 nm Vescent laser is frequency offset-locked and scanned across the $6P_{1/2}, F = 3$ transition from the $6S_{1/2}, F = 3$ ground state. The ladder configurations, using the different hyperfine structures to address the

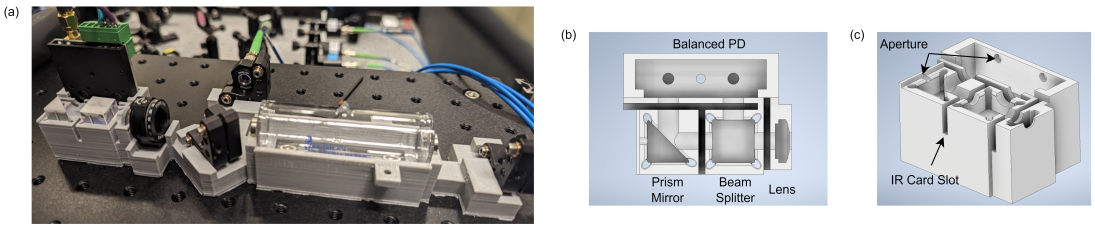


Figure 4.3: (a) Laboratory setup of the 3D printed push-fit board. Laser inputs are directed to the board using PM fibers. The Cs cell used in the setup is a standard 75mm length cell with no buffer gas. The board dimensions are 26cm × 7cm, and it is securely bolted onto an optics table with fasteners underneath the Cs cell. (b) Top view of the push-fit slot renders for the photodetector side. Components are provided with additional open space in sensitive locations, such as the active area and edges, to prevent damage. (c) Angled view of the render, highlighting the intermediate test points for sliding in IR cards and the apertures printed on the board to aid in alignment. The two apertures on the back of the balanced photodetector side align perfectly with the detectors.

two EIT setups, are shown in Figure 4.4(a) and Figure 4.4(b). A frequency change in the peak EIT signal measured in the probe would reflect an instability from the upper transition's lock; however, instabilities in the ground state lock with the CoSy module will also be daisy-chained to reflect in the T-P DAVLL. Finally, the probe spectrum is measured on superconducting nanowire single-photon detectors (SNSPD). While using SNSPDs are certainly overkill for this purpose, they were used out of convenience as this experimental setup was using sections of a separate four-wave mixing experiment that was already built.

The 895 nm probe is scanned from 8.500 GHz to 9.800 GHz. The transmission minimum of the EIT signal is expected to be at 9.192 GHz based on the fine structure splitting of the $6S_{1/2}$ state. The absorption spectrum of the probe is shown in Figure 4.5(a). Upon application of the control, the EIT signal becomes prominent in Figure 4.5(b). Such a spectrum is saved approximately every minute for 14 hours, and the position of the EIT peak is monitored to obtain lock stability.

Based on the time settings of the SNSPDs and scan range of the frequency offset lock, we can measure the drift of the EIT peak up to 8.75 kHz resolution. The result of the EIT peak tracking is shown in Figure 4.6. Over the course of 14 hours, the peak drifted over a total amplitude of 2.41 MHz and has a standard deviation of 0.41 MHz, which achieved an initial goal of being comparable to the natural linewidth of the transition given at 4.57 MHz [82]. The 0.41 MHz standard deviation of the 3D printed board is also comparable to the 0.36 MHz standard deviation observed in Becerra's results using traditional optical

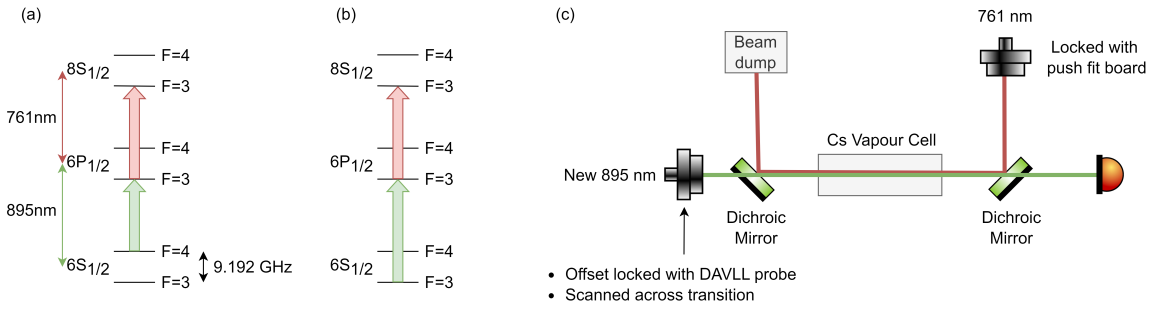


Figure 4.4: (a) Hyperfine splitting of the energy levels used in the T-P DAVLL lock. Here we use a probe locked between the $6S_{1/2}, F = 4$ to $6P_{1/2}, F = 3$ transition with the CoSy module. The T-P DAVLL locks the $6P_{1/2}, F = 3$ to $8S_{1/2}, F = 3$ transition. (b) In the stability test, the probe is frequency offset-locked to scan across the $6S_{1/2}, F = 3$ to $6P_{1/2}, F = 3$ transition. (c) Experimental diagram of the stability test. By monitoring the drift of the EIT signal from the scanning 895 probe, we obtain an estimate on the 761 nm lock stability.

mounts [52]. It may be possible to improve stability by more strategic positioning of the magnets. The current choice of magnets and their positions was designed and tested to maximize signal amplitudes and, consequently, to maximize locking duration. However, due to the size of the Cs cell, the magnets may appear more like point sources, resulting in a non-uniform magnetic field throughout the cell and not necessarily aligned with the wavevector of the lasers. By optimizing the magnet positions or using larger magnets, one may achieve a more uniform field at the cost of signal amplitude. Furthermore, over the course of 4 months, there has been little shift in the alignment of the 3D printed push-fit board, despite being in a non-temperature-regulated environment, and there is no visible degradation to the 3D printed PLA optics board.

4.3 Conclusion

Here, we demonstrate a miniaturized optical setup using a 3D printed push-fit-style board to lock lasers to the upper $6P_{1/2}$ to $8S_{1/2}$ atomic transitions using an EIT signal. Although observing EIT of two small beams on small photodetectors can be demanding in terms of alignment, the push-fit-style board maintained an error signal for 14 hours. In the design iterations of the push-fit board, some crucial design philosophies contributing to its success were the pre-aligned slots for non-alignment critical components, along with mirror mounts

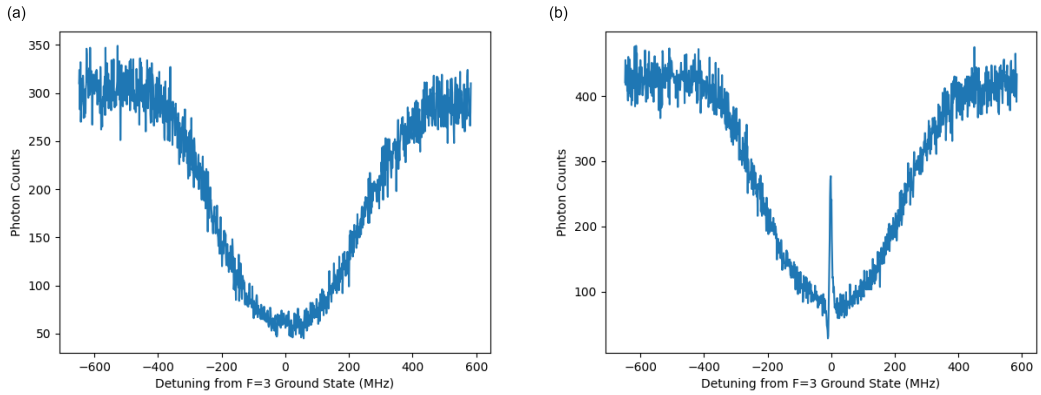


Figure 4.5: Resulting probe scans of EIT spectrum. (a) Probe transmission of the $6S_{1/2}, F = 3$ to $6P_{1/2}, F = 3$ transition as measured on SNSPDs. Probe detuning is centered to 0 by a 9.192 GHz offset corresponding to the fine structure splitting of the $6S_{1/2}, F = 3$ and $6S_{1/2}, F = 4$ ground states. (b) The same probe is now under the influence of a counterpropagating control beam at 761 nm, locked by the T-P DAVLL.

for the fiber inputs, as well as numerous intermediate test points for alignment, such as small apertures printed onto the board. At the time of writing this thesis, a new 3D printed T-P DAVLL was also setup for the 1469 nm transition, locking the $6P_{3/2}$ to $7S_{1/2}$ upper transition.

Further improvements to the design could involve a better implementation of a uniform magnetic field, achieved through more strategic magnet placements or the use of coils. The magnets used in the current setup are commercially available neodymium disc magnets typically intended for storage applications, so their magnetic fields and uniformity may be inconsistent. The push-fit board itself could be printed on a higher resolution 3D printer. The ones used for the current design have 13 μm positioning accuracy in all three dimensions, whereas many higher quality printers can achieve resolutions down to 6 μm . Our choice of a PLA printer was mainly due to accessibility; however, a resin-based board can be beneficial. Resin prints can offer higher resolution and smoother finishes, making them better for intricate and detailed prints such as the push-fit slots meant to hold delicate optical components. However, resin printers also typically have a smaller build volume, which constrained the current board's fabrication. They are more expensive and can have limited applications in certain wavelengths. For example, one must be cautious about the wavelengths used if a resin board were applied, as UV exposure may cause degradation.

The 3D printed optics boards offer an inexpensive, scalable, and highly customizable

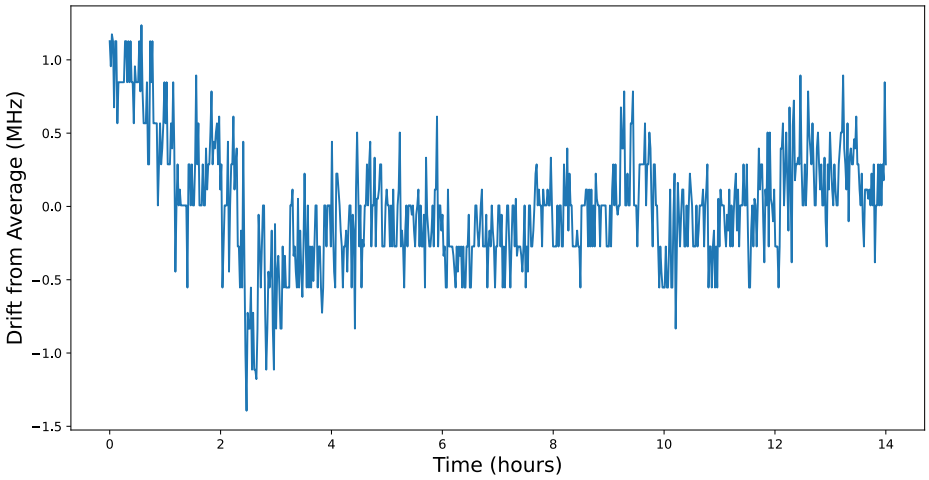


Figure 4.6: EIT peak drift monitored over the duration of 14 hours. The drift is centered around the average value of the EIT peak.

alternative to traditional free space optical setups. We envision numerous applications for this type of 3D printed board in any optical setup that requires miniaturization, such as various imaging setups and interferometry.

Chapter 5

Warm Atomic Memory

In Chapter 1, we outline the advantages of warm atomic memories, including their ease of implementation, on-demand accessibility, and prolonged storage durations due to long coherence times between energy levels. Although various protocols within warm atomic memories might appear similar initially, their underlying mechanisms are fundamentally distinct. Each protocol presents unique advantages and trade-offs regarding efficiency, fidelity, complexity, and storage durations [30]. In comparison, EIT memories offer a relatively long storage time for a straightforward and lower power setup [38]. These memories do not necessarily require cooling and can operate at lower powers due to near-resonance conditions. EIT memories are of particular interest for warm-atomic vapors as it is mostly insensitive to the single-photon detuning (Δ_p, Δ_c) of a given transition, so long as the two-photon detuning is zero ($\delta = \Delta_p - \Delta_c = 0$). Consequently, EIT memory protocols remain effective even in media with inhomogeneous broadening, such as a Doppler-broadened vapor cell [54].

This chapter of the thesis describes the constructed warm atomic memory setup in the lab. First, the protocol for an EIT memory is described and experimentally demonstrated. Subsequently, an investigation into various improvements aimed at extending storage time and enhancing efficiency is conducted. Finally, with EIT memory as the foundational mechanism, two additional experiments are introduced: a heralded EIT-memory scheme and lasing without inversion.

5.1 EIT Memory Protocol

Consider a Lambda system using the $6S_{1/2}$ hyperfine ground states of Cs and the $6P_{1/2}, F' = 4$ excited state, such as that in Figure 5.1(a). The protocol for an EIT memory is as follows: First, the strong control beam is sent through the atoms. The control pumps the atoms into the $6S_{1/2}, F = 4$ ground state and acts as a strong control for the EIT medium. After sufficient pumping duration, the probe (write) pulse is sent to the atoms. The probe enters the medium in the transparency window opened by the control and spatially compresses as it also enters a slow-light regime. Once the pulse has entered the medium, we remove the control field to trap the pulse in the atomic medium. The pulse is directly transferred to the spin coherence of the hyperfine ground states, often referred to as a spin wave in literature. At a later point, the stored information can be retrieved by reapplying the control beam to open the transparency window. For a given experimental cycle, two pulses should be expected on a detector filtered for the probe frequency. The first pulse matches in time with the write pulse; this is related to the storage efficiency and represents leakage of information that was not stored. The second pulse is the retrieved signal that matches in time with the start of the second control pulse. These are the photons that were successfully stored in the medium and recalled by the second control pulse. Ideally, for the same input, the first pulse should be minimized, indicating better storage efficiency, and the second pulse should be maximized for the highest retrieval efficiency. Such a pulse sequence and the expected detector peak timings are shown in Figure 5.1(b).

5.2 Experimental Setup for EIT Memory

The most recent experimental setup is shown in Figure 5.2. To begin, the control beam uses a Toptica 895 nm ECDL, frequency-locked to the exact transition of $6S_{1/2}, F = 3$ to $6P_{1/2}, F' = 4$ by saturation absorption spectroscopy with a CoSy module. The probe beam uses a Vescent 895 nm ECDL, frequency-locked to the $6S_{1/2}, F = 4$ to $6P_{1/2}, F' = 4$ transition with an offset phase lock from the Toptica as the master. The control beam pulses are generated through a fiber-coupled EOM, while the probe beam pulses are created by a free-space AOM. The exact pulse timings are synchronized with two function generators. Afterward, the beams are fiber-coupled to the memory setup using single-mode polarization-maintaining (PM) fibers. The control beam is sent through a 13 mm collimating lens to create a larger, approximately 2 mm diameter beam. In comparison, the probe beam is sent through a 4.5 mm collimating lens to achieve a 0.8 mm diameter beam. This ensures the probe beam travels through an EIT medium and that more atoms surround-

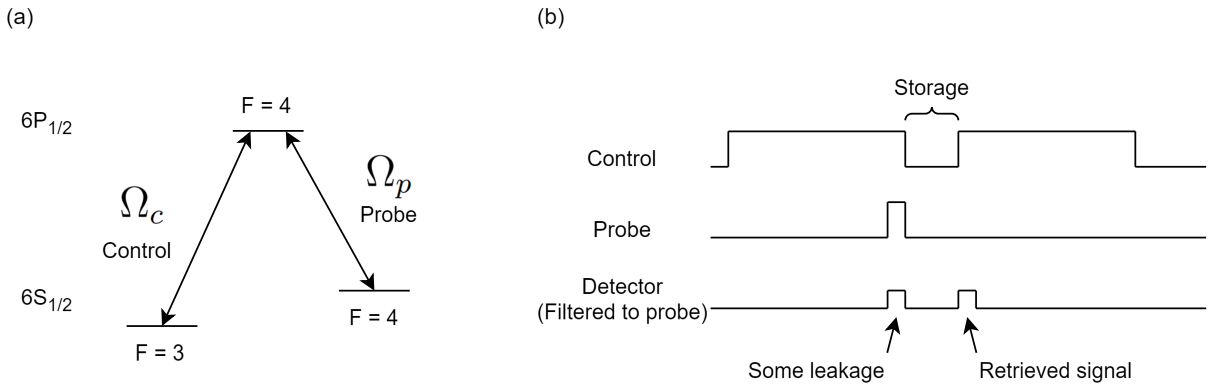


Figure 5.1: (a) Cs energy levels and hyperfine states used for Lambda EIT Memory. The strong control beam is resonant on $6S_{1/2}, F = 3$ to $6P_{1/2}, F' = 4$ transition, and the weak probe is resonant on $6S_{1/2}, F = 4$ to $6P_{1/2}, F' = 4$. (b) A typical pulse sequence for EIT storage that is aligned in time. The top two traces represent the pulses sent from their respective laser sources, while the bottom trace indicates the expected signal detected after storage, filtered to isolate the probe (i.e. the strong control beam is completely eliminated).

ing the probe beam are pumped. The pulse amplitudes of the control and probe beams are typically set to 2.5 mW and 1-10 μW, respectively. The two beams are combined at a PBS, and the alignment is adjusted to ensure they overlap spatially. The PBS serves to clean up the polarizations of the probe and control beams as they enter the atomic medium and provides an additional filtering option at the filtering stage. The combined beams then propagate through a Cs cell filled with 3 Torr neon buffer gas, placed inside a magnetic shield and oven to limit the Zeeman effect of stray magnetic fields and to control the OD. The signal is then fiber-coupled to the filtering stage. Throughout the various iterations of the EIT memory measurements, five different filters were tested to maximize the contrast and efficiency of the probe beam[1]. A table summarizing the performance specifications are shown in Table 5.1, and they are described in more detail in Appendix F. The most successful filter implementation is a double-pass etalon[2] and some additional polarization filtering. These two combined provide a filtering contrast of about 60 million and efficiency of 5%. At filtering, the signal from the memory passes through a PBS to remove some of the control beam, as the signal and control beams have orthogonal linear polarizations. The PBS also acts as a pick-off for the back-reflected signal beam through

[1]Filter efficiency is defined by probe transmission. Contrast is defined by the transmission ratio of probe vs. control.

[2]An etalon is essentially a Fabry-Perot cavity used as a very narrow bandpass filter.

the etalon. After the PBS, the beam passes through a half-wave plate (HWP) to rotate the polarization to match the etalon modes. The etalon further attenuates the control beam while maintaining a manageable transmission of the probe beam. Upon back-reflection, the beam passes through a quarter-wave plate (QWP) twice to rotate the polarization by 90 degrees, allowing it to reflect off the PBS and be fiber-coupled to sensitive detectors such as SNSPDs or avalanche photodetectors.

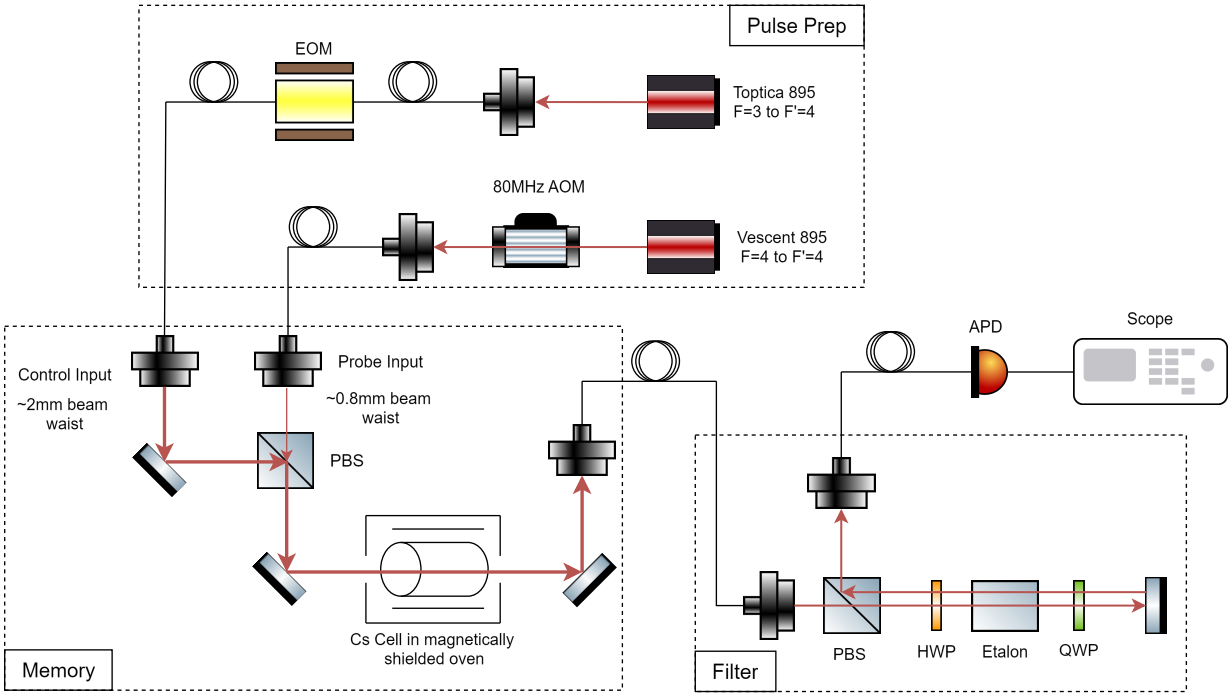


Figure 5.2: The experimental setup used for warm cell EIT memory. Broadly speaking separated into 3 main sections of laser pulse preparation, the atomic memory, and the filtering. These are all fiber coupled to each other through single-mode PM fibers. The pulse preparation is perhaps an oversimplification of the pick-offs after the laser head. It is just meant to indicate which tools are used to create pulses.

5.2.1 Magnetically Shielded Oven

In an effort to improve storage times and OD, we are implementing a custom-made magnetic shielding unit to protect the Cs cell from stray magnetic fields, integrated with a heating strip for temperature control. The setup uses two layers of a high-permeability

	852 nm		894 nm	
	Efficiency	Contrast	Efficiency	Contrast
852 Etalons (F=17 or 15 @ 852 nm)	25%	8000	50%	50
Monochromater	Not Tested (likely same)		5%	~100
Optical Pumping	80%	25	70%	20
894 Etalons (F=90 @ 852nm) - Single Pas	Not Tested		30%	1200
894 Etalons (F=90 @ 852nm) - Double Pa	35%	400	5%	600,000
Polarization	Not Tested (likely same)		98%	~100

Table 5.1: Summary of filter performances for the various setups to separate the two Cs hyperfine ground state transitions. F corresponds to the finesse of the Vitawave planar etalons as defined by their spec sheets at 852 nm.

magnetic material known as mu-metal to guide stray magnetic fields from the earth or surrounding electronics away from the Cs cell. Outside of the mu-metal sheets is a dual-heating tape that can provide temperature control comfortably up to 300°C. A cross-sectional diagram and build process is shown in Figure 5.3. The oven is structured using three aluminum tubes with diameters of 3.5", 2.5", and 1.5". The Cs cell is secured within the 1.5" tube by brass screws, and two alternating layers of insulator and mu-metal are wrapped around the outside of the 1.5" tube. The mu-metal comes in the form of thin, approximately 2 mm sheets, which are carefully wrapped around the insulating rings to prevent defects that degrade shielding performance. Each layer is secured by temperature-resistant Kapton tape and a metal zip tie on the final mu-metal layer. A heating strip is wrapped around the 2.5" layer and secured by Kapton tape. Finally, a 3.5" tube encloses all the components to retain heat. Each layer of shielding attenuates stray magnetic fields by a factor of 10 in both radial and axial directions, as measured with a gaussmeter. Two temperature probes are attached at the mu-metal layer and the heating strip to provide temperature feedback on experimental conditions. We commonly see about a 10°C difference between the heating strip and mu-metal layer, and perhaps can estimate another approximate 10°C different between the mu-metal and Cs cell. To minimize magnetic fields within the shield, an electronic temperature probe wasn't placed directly on the cell.

5.3 EIT Linewidth

Initially, we measure the linewidth of the EIT transmission window. This measurement serves to provide an initial estimate of critical experimental conditions, including decoher-

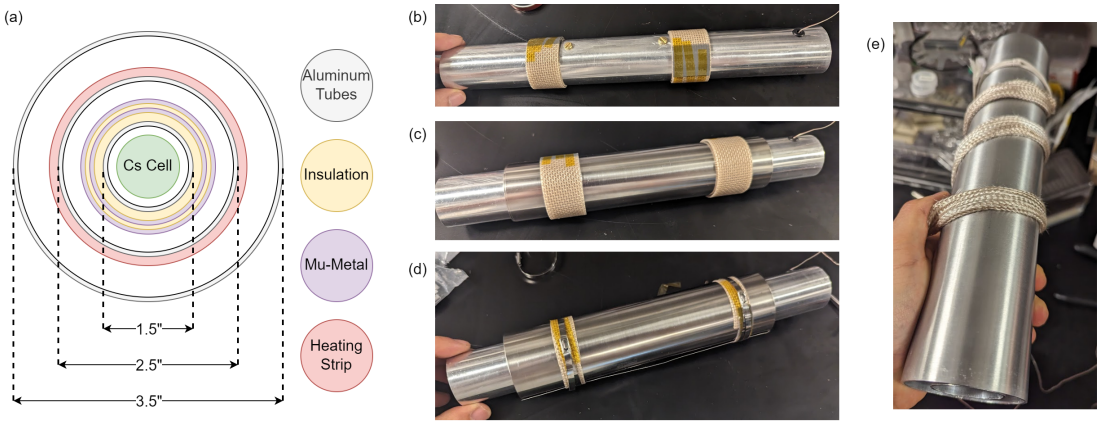


Figure 5.3: Diagram and assembly of magnetically shielded oven. (a) Cross-section of the magnetically shielded oven. (b) 1.5" tube with buffer gas cell mounted within by two brass screws. Two circular rings of insulating rubber are wrapped just beside the fasteners. (c) First layer of mu-metal shielding, and second insulating layer. (d) Second layer of mu-metal and metal zip-ties to secure all layers underneath. (e) 2.5" tube with heating tape wrapped around. The 1.5" tube with mu-metal and cell are inserted within.

ence rates and bandwidth. The typical transmission window peak is shown in Figure 5.4(a), where the FWHM of the transmission window is about 26 MHz when 15mW of control power is used. Another notable observation is the expected linear increase in bandwidth relative to the intensity of the control power [38]. Figure 5.4(b) shows with increments of ∼5mW control power, the spectral bandwidth also increases linearly as 5 MHz, 12MHz, 18MHz, 26MHz, scaling by roughly 1.4 MHz/mW.

5.4 Storage Time

Having established the appropriate filters and characterized the linewidth of the EIT, we proceed to conduct EIT memory measurements. Using the setup from Figure 5.2, we send two control pulses, each 1 μs long with a peak power of 2.5 mW, initially separated by 50 ns. Along with the first control pulse, we also send a 50 ns probe with a peak power of 3 μW to act as the write signal. The timing of this pulse sequence is illustrated in Figure 5.5(a). To further characterize storage, we increase the delay between the two control pulses. As expected, the delay of the retrieved signal follows the increase in control delay, as shown in Figure 5.5(b). Such series of plots are also used to characterize the storage

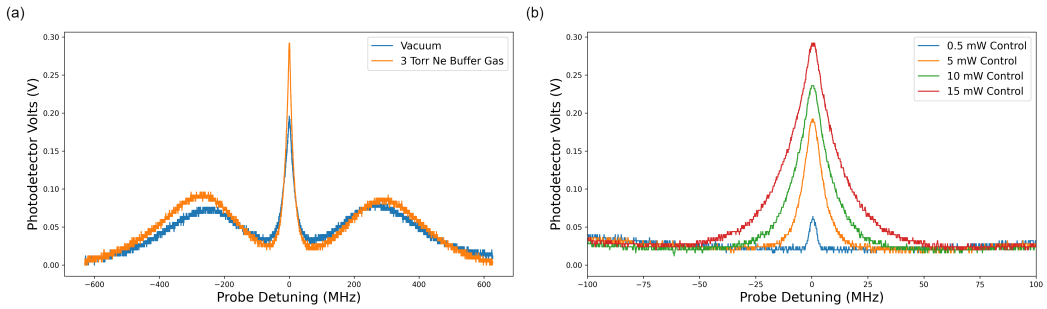


Figure 5.4: EIT 895 nm F=4 to F'=4 probe frequency scans with a resonant control beam. (a) Comparison of a Cs cell without buffer gas (blue) and a Cs cell with 3 Torr Neon buffer gas (Orange). (b) Transmission window changes with increasing control power in the buffer gas cell.

time for optical memories. The exact equation is determined by the time it takes for the total retrieved photon population A_{total} to reach 1/e of its maximum value, given by:

$$A_{total} = \int_{-\infty}^{\infty} A_{out}(t)\, dt \tag{5.1}$$

By fitting the total retrieved photon population vs. storage time to an exponential decay function, we obtain the storage time τ. An example of such fitting for the previously presented data is shown in Figure 5.6(a). In the first storage experiment, we only measured 60 ns of storage time. This was done with what could be considered the most basic setup possible for observing storage (a Cs cell without coatings or buffer gas, no magnetic shielding, no heating). In an effort to improve storage times, the vacuum cell was replaced with a cell containing 3 Torr of neon buffer gas. This improved the storage time to 90 ns. However, the most significant factor contributing to the improved storage time was the introduction of magnetic shielding. With just one layer of mu-metal, the storage time increased almost 7-fold to approximately 600 ns. Encouraged by this result, a second sheet of mu-metal was purchased, and the addition of the second layer further improved storage times to 1050 ns, approaching the commonly observed storage times in similar warm atom setups of 1-200 μs [34, 36]. These series of improvements in storage time are documented in Figure 5.6. Commercial magnetic shields typically employ three layers of mu-metal. While adding a third layer could potentially further enhance our storage time, we opted to prioritize improvements in storage efficiency for now.

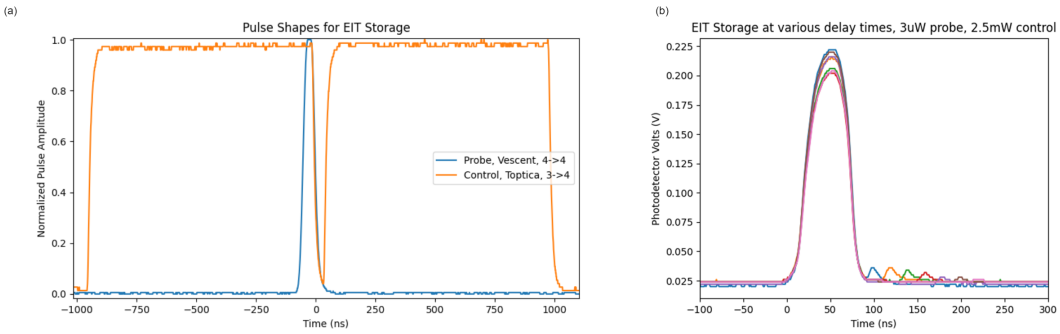


Figure 5.5: The typical EIT memory input pulse sequence as detected on an APD. (a) The input pulse sequence for a given experimental cycle: Two 1 μs, 2.5 mW peak power control pulses (orange) are separated by 50 ns. The 50 ns write signal (blue), with a peak power of 3 μW, is sent along with the first control pulse to store the signal. (b) Plot demonstrates the same experiment repeated at increasing delay times represented by the different colors, showing the characteristic decrease in retrieved pulse area as the storage time increases.

5.5 Memory Efficiency

As discussed in Section 1.1.1, memory efficiency is another critical metric for quantum memories. Overall efficiency is defined by the ratio of the total number of photons sent into the memory to the total number of photons retrieved. This measurement can be conducted by performing an EIT storage measurement for a given delay time to determine the total retrieved photon population, and then removing the cell to obtain the total number of photons initially sent into the memory. The results of such a measurement is shown in Figure 5.7. By integrating the pulse areas from Figure 5.7, we calculate a relatively low overall memory efficiency of 1.3%. The storage efficiency falls within an acceptable range at 80%; however, the retrieval efficiency is only 1.6%, indicating that decoherence during storage is the primary factor limiting our efficiency. In comparison to literature, Qunnect's Rb memory heated to 45°C has demonstrated a memory efficiency of 7% [36], while other similar setups have reported efficiencies ranging widely from 10% to 50% [38, 83, 84].

This low efficiency is likely from the low OD we observe from the atomic medium at room temperature. OD describes the maximum interaction of the probe with atoms, and for EIT memory schemes, it is desirable to have a large OD much greater than 1. From the same Figure 5.7, we observe that the OD for probe absorption alone is only 1.6. In warm atomic setups, higher OD is achieved by heating the vapor cell to temperatures commonly between 40 to 60°C. This is another reason why the oven was set up; however, testing and

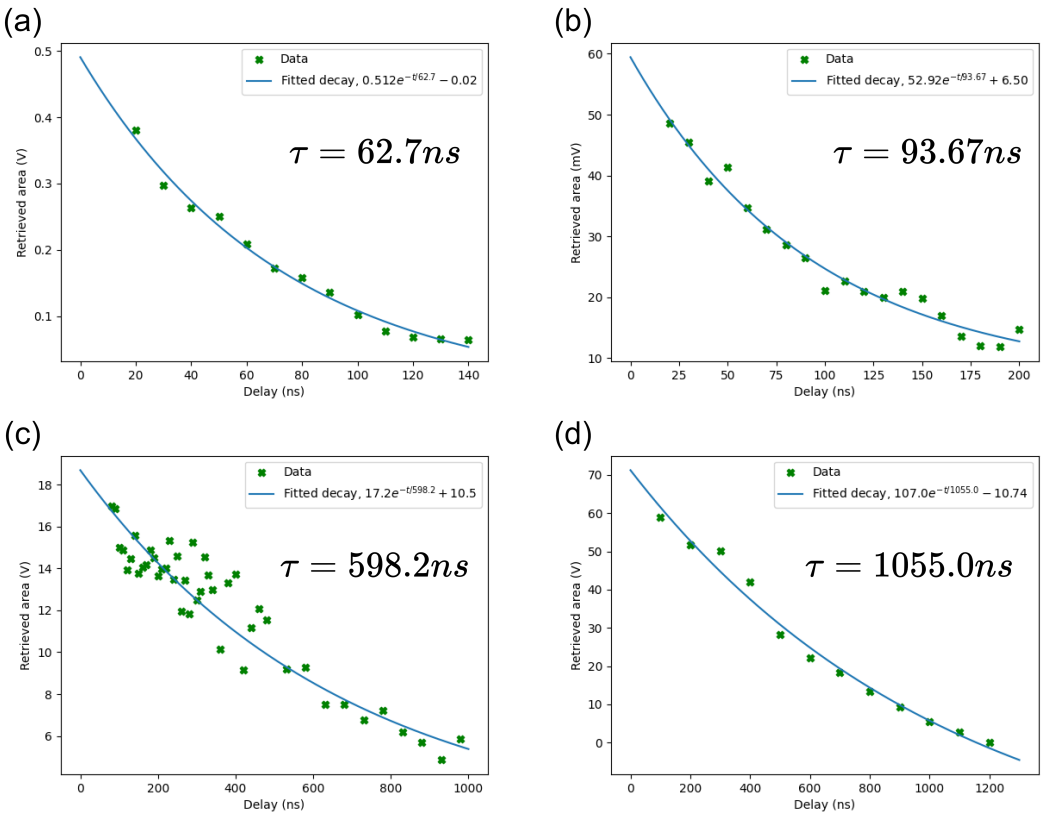


Figure 5.6: EIT storage total retrieved signal vs. storage delay time to obtain storage time τ. Each plot represents an improvement to the experimental setup. (a) Storage observed in vapor cell without buffer gas, optical pumping, or magnetic shielding. (b) Storage observed in vapor cell with 3 Torr Ne buffer gas and 100 μs optical pumping, but no magnetic shielding. (c) Storage observed in vapor cell with 3 Torr Ne buffer gas, 100 μs optical pumping, and only one layer of magnetic shielding. (d) Storage observed in vapor cell with 3 Torr Ne buffer gas, 100 μs optical pumping, and two layers of magnetic shielding.

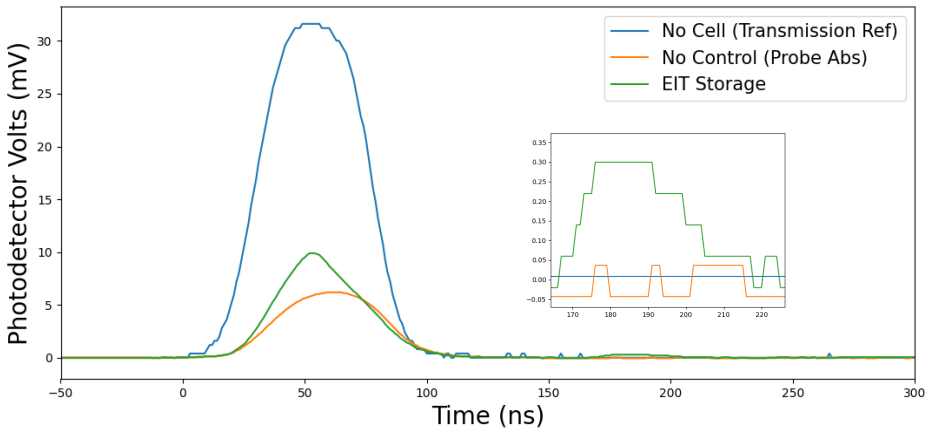


Figure 5.7: Probe signals detected on the APD in different configurations to measure storage efficiency. The blue curve, obtained by removing the Cs cell, provides a transmission reference for the probe and the total photon number sent into the memory. The orange curve represents typical probe absorption without the influence of EIT, from which the storage efficiency is determined. The green curve shows the EIT memory signal, and the retrieved pulse is used to calculate the retrieval efficiency and overall memory efficiency. Inset: a magnified view of the retrieval pulse.

optimizing the temperature controls remain an ongoing process, as we currently suffer from significant condensation of the atoms on the cell walls. This occurs when the increased vapor pressure causes the atoms to condensate in cooler areas of the vapor cell. Significant condensation leads to obstruction of the beam path with seemingly random deflection and transmission losses.

Another common approach to improve memory efficiency is through iterative pulse-shaping for the write pulse, as proposed by Gorschkov et al. [85] and experimentally demonstrated by Novikova et al. [83]. For a specific OD, there exists an optimal pulse shape to achieve maximum storage efficiency. The optimal pulse shape is found by initially sending a probe pulse of arbitrary shape (e.g., Gaussian), and then measuring the retrieved pulse. The retrieved pulse provides a more accurate representation of the optimal pulse shape for storage, so the time-reversed shape of the retrieved pulse is used as the write pulse in the next iteration. In Novikova's experiment, they found that after three iterations, the memory efficiency improved from 16% to 47%. We would also like to implement such a process, but there are limitations to probe pulse shaping on the tens of nanoseconds scale

due to the slow response of the AOM.

5.6 Summary of EIT Memory Results

In summary, we have implemented a warm Cs atomic memory and are progressing towards interfacing it with QD photons. By iteratively improving the vapor cell setup with magnetic shielding and introducing buffer gas, we have been able to extend storage times from 60 ns to 1 μs, although the efficiency remains relatively low at 1.3%. To further extend storage times, using a Cs cell coated with paraffin or specialized polymers to prevent dephasing from collisions with the cell wall may be beneficial. Additionally, adding another layer of magnetic shielding could further reduce dephasing caused by stray magnetic fields. The objective of improving efficiency remains an ongoing effort. The most direct method would be to increase the OD by raising the temperature using the newly built oven. Another option to enhance efficiency would be to implement iterative pulse shaping optimization, as described in Section 5.5. However, this approach would likely require redesigning the pulse generation system, given the current limitations of the AOM in performing high-resolution pulse shaping.

Note that Off-resonant Raman protocols follow an extremely similar experimental procedure, with the only difference being the amount of detuning, as it relies on stimulated Raman transitions. Off-resonant Raman moves into a far-off resonant regime, making it more compatible with the broadband ($\sim$GHz) photons received from QDs. Experiments have already demonstrated GHz bandwidth capabilities with Cs atoms [86]. A trade-off for this larger bandwidth is the requirement for a stronger control laser, necessary because we are operating far-off resonance, and a potentially shorter storage time due to the increased likelihood of four-wave mixing (FWM) caused by the strong control laser [38]. While off-resonant Raman memories show promise for future investigations in quantum dot integration, current laser limitations confine us to on-resonance fields to ensure zero two-photon detuning.

5.7 Further Experiments with Warm Atoms

Following the initial demonstration of an EIT memory, two other experiments emerged to advance the warm atom setup and facilitate experiments in support of the quantum repeater project. The fundamental mechanisms of these tasks are both related to EIT, they are: EIT-based single-photon generation and lasing without inversion (LWI). Attempts

were made to carry out these measurements; however, they yielded little success. While a detailed explanation of these topics may exceed the scope of this thesis, their general framework will be outlined to inspire future experiments with warm atoms.

5.7.1 EIT-based single-photon generation

There exists an alternative EIT memory protocol distinct from the previously discussed approach outlined in Section 5.1. Here, instead of co-propagating a strong control beam with the write signal, only the probe beam is sent into the medium. With a non-unitary probability, the probe induces an excitation and transition into another ground state. During this process, it emits a photon that heralds the storage event. Later, a control beam is applied to map the photon back onto the probe transition. The strong control beam also serves as the EIT control laser, opening a transparency window for the probe to propagate out of the atomic medium. An illustration is provided in Figure 5.8, and further elaboration can be found in Dr. Eisaman's thesis [87].

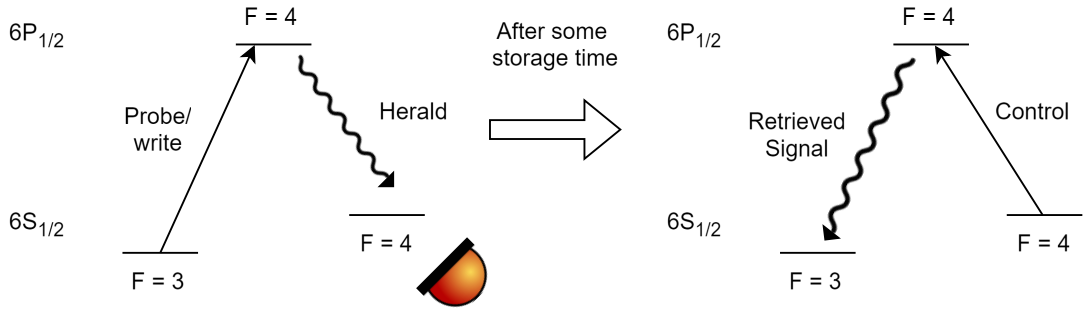


Figure 5.8: The protocol for a heralded memory based on EIT using the hyperfine ground states of Cs.

The primary distinction between the two cases lies in the heralding event, which is probabilistic but achieves exceptionally high storage and retrieval efficiency upon detection. Furthermore, the storage mechanism utilizes a transition to the excited state for storage, unlike the previously discussed EIT memory where the probe's coherence is mapped directly to the spin coherence of the ground states without inducing excitations.

During our own testing of this process, we encountered challenges in detecting any heralding events. The ability to detect heralded photons is primarily constrained by the small solid angle of collection into the fiber coupler. Additionally, when the OD is low,

the likelihood of detecting heralded photons decreases as heralding is directly related to absorption and spontaneous emission. We envision that introducing heating could enhance our ability to detect heralded photons and enable further exploration of this memory scheme.

5.7.2 Lasing without inversion

As we may be familiar, population inversion[3] is commonly required to achieve lasing. However, in a specific 3-level energy level structure such as the Lambda system, it is possible to achieve stimulated emission without a larger excited state population. This phenomenon, known as lasing without inversion (LWI), can act like a gain medium for weak signals. The fundamental mechanism resembles that of EIT, where the probability amplitudes for excitation interfere destructively to suppress absorption. For a detailed analysis of this topic, refer to Mompart and Corbalan [88].

This mechanism could potentially be applied to the quantum repeater to amplify weak signals, such as a single photon from the QD, or, if precise control over storage is achievable, it could potentially add another single photon to the QD's output. While we investigated this in our lab, we have yet to confidently demonstrate any form of gain medium. However, this also may become feasible with increased OD facilitated by a functional oven.

[3] In its simplest definition, population inversion occurs when the excited state has a larger population than the ground state

Chapter 6

Conclusion

The main projects in this thesis are all connected to the hybrid quantum repeater project in the lab. The overarching aim is to achieve a robust interface between atoms and quantum dot photon sources to establish a repeater node for a quantum network. In the past, our lab has focused on cold atomic setups and improving light interactions by loading atoms into hollow-core photonic crystal fibers. This thesis extends the investigation into quantum dot photon sources to facilitate their eventual deployment. Additionally, we explore and develop a newly constructed warm atom setup. Warm atoms offer many interesting applications as a standalone platform and can perform similar experiments to the cold atomic setup in a more easily tested, sandbox-like environment. This preliminary testing or benchmarking can occur prior to fully implementing an experiment within the more intricate, but potentially higher-performing, cold atom setups.

In Chapter 2 and Chapter 3, we examine the QD single-photon source, emphasizing the challenges associated with its excitation and the complexities in interfacing it with atoms. We present a newly built EOM bias controller using purely DC signals and a custom-made pulse generator to create consistent 100 ps, 30 dB optical pulses. These pulses were then used to perform above-band excitation of the quantum dot, achieving a $g^{(2)}(0) = 0.095 \pm 0.0082$. Furthermore, we investigate the frequency tuning of various quantum dots via gas injection and assess the potential of this technique to control some of the QD asymmetry, as both are influenced by applied local strain. In specific QDs, we observed a decrease in FSS, suggesting it may be possible to find a QD with a sufficiently small initial FSS to completely remove it through gas tuning.

Chapter 4 presents a method for mounting optics using 3D-printed push-fit style boards to frequency lock lasers to upper atomic transitions. This method benefits from many

traditional advantages of 3D printing, such as rapid prototyping and deployment, high degrees of customization, and low cost compared to traditional optical mounts[1]. The 3D-printed laser locking board was able to lock the $6P_{1/2}$ to $8S_{1/2}$ upper transition of Cs for up to 14 hours with a standard deviation of 0.41 MHz in frequency. Currently, there are two 3D-printed DAVLLs set up in the lab for the 761 nm and 1470 nm transitions, providing full access to the upper transitions in four-wave mixing schemes. It would be interesting to see a more streamlined version of this process. Imagine someone wanting to quickly test an optical setup. Instead of having to first find space on an optics table, order components, and tediously align them, they could simply design a beam path with the specified optics through a user interface. The software would then automatically design a push-fit board using the available online CAD files for optical components. Over lunch, a pre-aligned optics board could be prepared on a 3D printer and ready for a quick test. Instead of spending an entire day aligning optics, one would just need to pop components into these pre-designed beam paths. While this is perhaps an ambitious proposal based on the results presented in this thesis, it would be an extremely useful tool in many optics labs.

Finally, Chapter 5 presents the implementation of an EIT optical memory with warm Cs atomic vapor. The first challenge, filtering out the strong pump, was accomplished by installing a new etalon filter that can be temperature-tuned. Then, through iterative improvements to the vapor cell setup, such as including buffer gas and magnetic shielding, we achieved 1 μs of storage, although with relatively low efficiency. The efficiency can be improved by performing iterative pulse shaping and heating the vapor cell to about 50 degrees Celsius to increase OD. To do so, some improvements to the setup are likely needed, such as a more reliable pulse shaping setup. An initial version of the oven is built, but there is significant condensation of the vapor in the cell, and it should perhaps be redesigned to purposefully introduce a cold point on the cell so that condensation occurs out of the beam path. Further experiments enabled by such a setup include a heralded storage scheme and lasing without inversion to amplify weak signals. Another interesting scheme closely related to EIT memory is off-resonant Raman schemes, which could also be pursued for broader bandwidth operations and interfacing with the broadband photons from the QD.

[1]Each 3D printed DAVLL board costs about two dollars to print

References

[1] L. Zou, S. Gupta, and C. Caloz. A simple picosecond pulse generator based on a pair of step recovery diodes. *IEEE Microwave and Wireless Components Letters*, 27 (5), 2017.

[2] S. Wehner, D. Elkouss, and R. Hanson. Quantum internet: A vision for the road ahead. *Science*, 362, 2018.

[3] SH. Wei et al. Towards real-world quantum networks: a review. *Laser and Photonics Reviews*, 16, 2022.

[4] Jiajun Chen. Review on quantum communication and quantum computation. *J. Phys. Conf.*, 1865, 2021.

[5] S. Muralidharan, L. Li, J. Kim, N. Lutkenhaus, M. D. Lukin, and L. Jiang. Optimal architectures for long distance quantum communication. *Sci Rep*, 6, 2016.

[6] K. Azuma, S. E. Economou, D. Elkouss, P. Hilaire, L. Jiang, H.-K. Lo, and I. Tzitrin. Quantum repeaters: From quantum networks to the quantum internet. *Rev. Mod. Phys.*, 95, 2023.

[7] C. Couteau, S. Barz, T. Durt, T. Gerrits, J. Huwer, R. Prevedel, J. Rarity, A. Shields, and G. Weihs. Applications of single photons to quantum communication and computing. *Nat Rev Phys*, 5:326–338, 2023.

[8] Charles H. Bennett and Gilles Brassard. Quantum cryptography: Public key distribution and coin tossing. *Theoretical Computer Science*, 560:175–179, 1984.

[9] Phillip Kaye, Raymend Laflamme, and Michele Mosca. *An Introduction to Quantum Computing*. Oxford University Press, 2007.

[10] Qiao Ruihong and Meng Ying. Research progress of quantum repeaters. *J. Phys.: Conf. Ser.*, 1237 (5), 2018.

[11] D. Dieks. Communication by epr devices. *Physics Letters A*, 92, 1982.

[12] W. K. Wootters and W. H. Zurek. A single quantum cannot be cloned. *Nature*, 299, 1982.

[13] Koji Azuma, Kiyoshi Tamaki, and Hoi-Kwong Lo. All-photonic quantum repeaters. *Nat Commun.*, 6, 2015.

[14] M. Zukowski, A. Zeilinger, M. A. Horne, and A. K. Ekert. 'event-ready-detectors' bell experiment via entanglement swapping. *Phys. Rev. Lett.*, 71, 1993.

[15] S. L. Braunstein and A. Mann. Measurement of the bell operator and quantum teleportation. *Phys. Rev. A*, 51, 1995.

[16] L.-M. Duan, M. D. Lukin, J. I. Cirac, and P. Zoller. Long-distance quantum communication with atomic ensembles and linear optics. *Nature*, 414:413–418, 2001.

[17] Seung-Woo Lee and Hyunseok Jeong. Bell-state measurement and quantum teleportation using linear optics: two-photon pairs, entangled coherent states, and hybrid entanglement. *arXiv: Quantum Physics*, 2013.

[18] H. J. Briegel, W. Dür., J. I. Cirac, and P. Zoller. Quantum repeaters: The role of imperfect local operations in quantum communication. *Phys. Rev. Lett.*, 81 (26), 1998.

[19] S. Chen, Y.-A. Chen, T. Strassel, Z.-S. Yuan, B. Zhao, J. Schmiedmayer, and J.-W. Pan. Deterministic and storable single-photon source based on a quantum memory. *Phys. Rev. Lett.*, 97 (17), 2006.

[20] T. Li and F.-G. Deng. Heralded high-efficiency quantum repeater with atomic ensembles assisted by faithful single-photon transmission. *Scientific Reports*, 5, 2015.

[21] A. N. Craddock, Y. Wang, F. Giraldo, R. Sekelsky, M. Flament, and M. Namazi. High-rate subgigahertz-linewidth bichromatic entanglement source for quantum networking. *Phys. Rev. Applied*, 21, 2023.

[22] S. Buckley, K. Rivoire, and J. Vučković. Engineered quantum dot single-photon sources. *Rep. Prog. Phys.*, 75, 2012.

[23] N. Somaschi, V. Giesz, and et al. L. De Santis. Near-optimal single-photon sources in the solid state. *Nature Photon*, 10:326–338, 2016.

[24] M. Anderson, T. Müller, J. Skiba-Szymanska, A. B. Krysa, J. Huwer, R. M. Stevenson, J. Heffernan, D. A. Ritchie, and A. J. Shields. Gigahertz-clocked teleportation of time-bin qubits with a quantum dot in the telecommunication *c* band. *Phys. Rev. Appl.*, 13:054052, May 2020.

[25] M. D. Eisaman, J. Fan, A. Migdall, and S. V. Polyakov. Invited review article: Single-photon sources and detectors. *Rev. Sci. Instrum.*, 82, 2011.

[26] M. Hennrich, T. Legero, A. Kuhn, and G. Rempe. Photon statistics of a non-stationary periodically driven single-photon source. *New J. Phys.*, 6 (86), 2004.

[27] T Gaebel, I Popa, A Gruber, M. Domhan, F. Jelezko, and J. Wrachtrup. Stable single-photon source in the near infrared. *New J. Phys.*, 6 (98), 2004.

[28] M. E. Reimer and C. Cher. The quest for a perfect single-photon source. *Nature Photonics*, 13, 2019.

[29] R. K. Ramakrishnan, A. B. Ravichandran, I. Kaushik, G. Hegde, S. Talabattula, and P. P. Rohde. The quantum internet: A hardware review. *Journal of the Indian Institute of Science*, 103:547–567, 2023.

[30] Kai Shinbrough, Donny R. Pearson Jr., Bin Fang, Elizabeth A. Goldschmidt, and Virginia O. Lorenz. Broadband quantum memory in atomic ensembles. *Advances in Atomic, Molecular, and Optical Physics*, 72, 2023.

[31] Jean-Philippe Bourgoin, Evan Meyer-Scott, Brendon Higgins, Bassam Helou, Chris Erven, Hannes Huebel, B. Kumar, D. Hudson, Ian D'Souza, Ralph Girard, Raymond Laflamme, and Thomas Jennewein. A comprehensive design and performance analysis of low earth orbit satellite quantum communication. *New Journal of Physics*, 15, 2012.

[32] Y.-W. Cho and Y.-H. Kim. Atomic vapor quantum memory for a photonic polarization qubit. *Optics Express*, 18 (25), 2010.

[33] S. Jiang, X.-M. Luo, L.-Q. Chen, B. Ning, S. Chen, J.-Y. Wang, Z.-P. Zhong, and J.-W. Pan. Observation of prolonged coherence time of the collective spin wave of an atomic ensemble in a paraffin-coated 87rb vapor cell. *Phys. Rev. Applied*, 80, 2009.

[34] Lijun Ma, Oliver T. Slattery, Paulina S. Kuo, and Xiao Tang. Eit quantum memory with cs atomic vapor for quantum communication. *SPIE Optics and Photonics 2015 Proc.*, 9615, 2015.

[35] O. Katz and O. Firstenberg. Light storage for one second in room-temperature alkali vapor. *Nature Communications*, 9, 2018.

[36] Y. Wang, A. N. Craddock, R. Sekelsky, M. Flament, and Mehdi Namazi. Field-deployable quantum memory for quantum networking. *Phys. Rev. Applied*, 18, 2022.

[37] M. V. Balabas, K. Jensen, W. Wasilewski, H. Krauter, L. S. Madsen, J. H. Müller, T. Fernholz, and E. S. Polzik. High quality anti-relaxation coating material for alkali atom vapor cells. *Opt. Express*, 18 (6):5825–5830, 2010.

[38] Lijun Ma, Oliver Slattery, and Xiao Tang. Optical quantum memory based on electromagnetically induced transparency. *J. Opt.*, 19, 2017.

[39] S. Manz, T. Fernholz, J. Schmiedmayer, and J.-W. Pan. Collisional decoherence during writing and reading quantum states. *Phys. Rev. A*, 75, 2007.

[40] T. Yoon and M. Bajcsy. Laser-cooled cesium atoms confined with a magic-wavelength dipole trap inside a hollow-core photonic-bandgap fiber. *Phys. Rev. A*, 99, 2019.

[41] T. Yoon and M. Bajcsy. Simulating gravity-assisted loading of laser-cooled atoms into a hollow-core photonic-bandgap fiber. *J. Phys. B: At. Mol. Opt. Phys.*, 53, 2000.

[42] R. A. Maruf, S. Venuturumilli, D. Bharadwaj, P. Anderson, J. Qiu, Y. Yuan, B. Semnani, S. Malik, M. Zeeshan, D. Dalacu, P. Poole, M. Reimer, and M. Bajcsy. Widely tunable solid-state source of single photons matching an atomic transition. *Proc. SPIE*, 12016, 2022.

[43] S. E. Harris, J. E. Field, and A. Imamoglu. Nonlinear optical processes using electromagnetically induced transparency. *Phys. Rev. Lett.*, 64, 1990.

[44] M. Fleischhauer, A. Imamoglu, and J. P. Marangos. Electromagnetically induced transparency: Optics in coherent media. *Reviews of Modern Physics*, 77 (2):633–673, 2005.

[45] Jiepeng Zhang, Gessler Hernandez, and Yifu Zhu. Slow light with cavity electromagnetically induced transparency. *Optics Letters*, 33 (1):46–48, 2008.

[46] K. DeRose, K. Jiang, J. Li, L. Zhuo, S. Wenner, and S. Bali. Producing slow light in warm alkali vapor using electromagnetically induced transparency. *Am. J. Phys.*, 91:193–205, 2020.

[47] A. H. Safavi-Naeini, T. P. Mayer Alegre, J. Chan, M. Eichenfield, M. Winger, Q. Lin, J. T. Hill, D. E. Chang, and O. Painter. Electromagnetically induced transparency and slow light with optomechanics. *Nature*, 472:69–73, 2011.

[48] Yong-Chun Liu, Bei-Bei Li, and Yun-Feng Xiao. Electromagnetically induced transparency in optical microcavities. *Nanophotonics*, 6 (5):789–811, 2017.

[49] Na Liu, Thomas Weiss, Martin Mesch, Lutz Langguth, Ulrike Eigenthaler, Michael Hirscher, Carsten Sönnichsen, and Harald Giessen. Planar metamaterial analogue of electromagnetically induced transparency for plasmonic sensing. *Nano Letters*, 10 (4):1103–1107, 2010.

[50] G. Morigi, J. Eschner, and C. H. Keitel. Ground state laser cooling using electromagnetically induced transparency. *Phys. Rev. Lett*, 85 (21), 2000.

[51] C. F. Roos, D. Leibfried, A. Mundt, F. Schmidt-Kaler, J. Eschner, and R. Blatt. Experimental demonstration of ground state laser cooling with electromagnetically induced transparency. *Phys. Rev. Lett*, 85 (26), 2000.

[52] F. E. Becerra, R. T. Willis, S. L. Rolston, and L. A. Orozco. Two-photon dichroic atomic vapor laser lock using electromagnetically induced transparency and absorption. *J. Opt. Soc. Am. B*, 26 (7):1315–1320, 2009.

[53] Lijun Ma, Oliver Slattery, and Xiao Tang. Optical quantum memory and its applications in quantum communication systems. *Journal of research of the National Institute of Standards and Technology*, 125, 2020.

[54] Alexander I. lvovsky, Barry C. Sanders, and Wolfgang tittel. optical quantum memory. *Nature Photonics*, 3:706–714, 2009.

[55] D. A. Steck. *Quantum and Atom Optics*. University of Oregon, 2007.

[56] Ran Finkelstein, Samir Bali, Ofer Firstenberg, and Irina Novikova. A practical guide to electromagnetically induced transparency in atomic vapor. *New J. Phys.*, 25, 2023.

[57] Patrick Laferriere, Edith Yeung, Isabelle Miron, David B. Northeast, Sofiane Haffouz, Jean Lapointe, Marek Korkusinski, Philip J. Poole, Robin L. Williams, and Dan

Dalacu. Unity yield of deterministically positioned quantum dot single photon sources. *Scientific Reports*, 12, 2022.

[58] R. M. Stevenson, R. J. Young, P. Atkinson, K. Cooper, D. A. Ritchie, and A. J. Shields. A semiconductor source of triggered entangled photon pairs. *Nature*, 439, 2006.

[59] O. Benson, C. Santori, M. Pelton, and Y. Yamamoto. Regulated and entangled photons from a single quantum dot. *Physical Review Letters*, 84 (11), 2000.

[60] Jiawei Yang, Yan Chen, Zhixuan Rao, Ziyang Zheng, Changkun Song, Kaili Xiong Yujie Chen, Pingxing Chen, Chaofan Zhang, Wei Wu, Ying Yu, and Siyuan Yu. Tunable quantum dots in monolithic fabry-perot microcavities for high-performance single-photon sources. *Light: Science and Applications*, 13, 2024.

[61] S.M. Ulrich, A. Ulhaq, and P. Michler. Resonance fluorescence emission from single semiconductor quantum dots coupled to high-quality microcavities. *Quantum Optics with Semiconductor Nanostructures*, pages 3–45, 2012.

[62] L. Leandro, C. P. Gunnarsson, R. Reznik, K. D. Jöns, I. Shtrom, A. Khrebtov, T. Kasama, V. Zwiller, G. Cirlin, and N. Akopian. Nanowire quantum dots tuned to atomic resonances. *Nano Lett.*, 18 (11):7217–7221, 2018.

[63] J. Leng, Y. Xu, Y. Chan, P. Wang, S. Ryuzaki, K. Okamoto, and K. Tamada. Tuning the emission colors of self-assembled quantum dot monolayers via one-step heat treatment for display applications. *ACS Appl. Nano Mater.*, 3 (4), 2020.

[64] J. J. Dubowski, R. Stanowski, Dalacu D, and P. J. Poole. Precision tuning of inas quantum dot emission wavelength by iterative laser annealing. *Optics and Laser Technology*, 103:382–286, 2018.

[65] S. Sun, H. Kim, G. S. Solomon, and E. Waks. Strain tuning of a quantum dot strongly coupled to a photonic crystal cavity. *Appl. Phys. Lett.*, 103 (15), 2013.

[66] Tim Kroh, Janik Wolters, Andreas Ahlrichs, Andreas W. Schell, Alexander Thoma, Stephan Reitzenstein, Johannes S. Wildmann, Eugenio Zallo, Rinaldo Trotta, Armando Rastelli, Oliver G. Schmidt, and Oliver Benson. Slow and fast single photons from a quantum dot interacting with the excited state hyperfine structure of the cesium d1-line. *Sci. Rep.*, 9, 2019.

[67] Joel Q Grim, Allan S Bracker, Maxim Zalalutdinov, Samuel G Carter, Alexander C Kozen, Mijin Kim, Chul Soo Kim, Jerome T Mlack, Michael Yakes, Bumsu Lee, and Daniel Gammon. Scalable in operando strain tuning in nanophotonic waveguides enabling three-quantum-dot superradiance. *Nat. Mater.*, 9, 2019.

[68] R. A. Maruf, S. Venuturumilli, D. Bharadwaj, P. Anderson, J. Qiu, M. Zeeshan, B. Semnani, P. Poole, D. Dalacu, M. Reimer, and M. Bajcsy. Reversible tuning of nanowire quantum dot to cesium d1 line. *CLEO*, 2023.

[69] Christopher Palmer. *Diffraction Grating Handbook*. MKS Instruments, Inc., 2020.

[70] G. L. Li and P. K. L. Yu. Optical intensity modulators for digital and analog applications. *Journal of Lightwave Technology*, 21 (9), 2003.

[71] P. Anderson, D. Bharadwaj, R. A. Maruf, J. Qiu, Y. Yuan, B. Semnani, M. Reimer, and M. Bajcsy. Generating single photon pulses from a quantum dot using a continuous wave laser and an electro-optic modulator. *Conference on Lasers and Electro-Optics*, 2021.

[72] P. Michler. *Quantum Dots for Quantum Information Technologies*. Springer, 2017.

[73] T. M. Stace, G. J. Milburn, and C. H. W. Barnes. Entangled two-photon source using biexciton emission of an asymmetric quantum dot in a cavity. *Physical Review B*, 67, 2003.

[74] A. Fognini, A. Ahmadi, S. J. Daley, M. E. Reimer, and V. Zwiller. Universal fine-structure eraser for quantum dots. *Optics Express*, 26 (19), 2018.

[75] Thomas Lettner, Samuel Gyger, Katharina D. Zeuner, Lucas Schweickert, Stephan Steinhauer, Carl Reuterskiöld Hedlund, Sandra Stroj, Armando Rastelli, Mattias Hammar, Rinaldo Trotta, Klaus D. Jöns, and Val Zwiller. Strain-controlled quantum dot fine structure for entangled photon generation at 1550 nm. *Nano Lett.*, 21 (24):10501–10506, 2021.

[76] S. Seidl, M. Kroner, A. Hogele, K. Karrai, R. J. Warburton, a. Badolato, and P. M. Petroff. Effect of uniaxial stress on excitons in a self-assembled quantum dot. *Applied Physics Letters*, 99, 2006.

[77] K. L. Corwin, Z-T. Lu, C. F. Hand, R. J. Epstein, and C. E. Wieman. Frequency-stabilized diode laser with the zeeman shift in an atomic vapor. *Appl. Opt.*, 37 (15):3295–3298, 1998.

[78] H. S. Moon, W-K. Lee, L. Lee, and J. B. Kim. Double resonance optical pumping spectrum and its application for frequency stabilization of a laser diode. *Appl. Phys. Lett.*, 85 (18):3965–3967, 2004.

[79] S. C. Bell, D. M. Heywood, J. D. White, J. D. Close, and R. E. Scholten. Laser frequency offset locking using electromagnetically induced transparency. *Appl. Phys. Lett.*, 90, 2007.

[80] M. T. Hummon, S. Kang, D. G. Bopp, Q. Li, D. A. Westly, S. Kim, C. Fredrick, S. A. Diddams, K. Srinivasan, V. Aksyuk, and J. E. Kitching. Photonic chip for laser stabilization to an atomic vapor with 10e-11 instability. *Optica*, 5 (4), 2018.

[81] S.H. Madkhaly, L.A. Coles, C. Morley, C.D. Colquhoun, T.M. Fromhold, N. Cooper, and L. Hackermüller. Performance-optimized components for quantum technologies via additive manufacturing. *PRX Quantum*, 2, 2021.

[82] D. A. Steck. Cesium d line data. https://steck.us/alkalidata/. (revision 2.3.2, 10 September 2023). Accessed: 2024-05-30.

[83] I. Novikova, A. V. Gorshkov, D. F. Phillips, A. S. Sørensen, M. D. Lukin, and R. L. Walsworth. Optimal control of light pulse storage and retrieval. *Phys. Rev. Lett.*, 98, 2007.

[84] I. Novikova, R.L. Walsworth, and Y. Xiao. Electromagnetically induced transparency-based slow and stored light in warm atoms. *Laser and Photonics Reviews*, 6 (3), 2011.

[85] A. V. Gorshkov, A. André, M. Fleischhauer, A. S. Sørensen, and M. D. Lukin. Universal approach to optimal photon storage in atomic media. *Phys. Rev. Lett.*, 98, 2007.

[86] K. F. Reim, J. Nunn, V. O. Lorenz, B. J. Sussman, K. C. Lee, N. K. Langford, D. Jaksch, and I. A. Walmsley. Towards high-speed optical quantum memories. *Nature Photonics*, 4, 2010.

[87] Matthew D. Eisaman. *Generation, Storage, and Retrieval of Nonclassical States of Light using Atomic Ensembles*. PhD thesis, Harvard University, 2006.

[88] J. Mompart and R. Corbalan. Lasing without inversion. *Journal of Optics B Quantum and Semiclassical Optics*, 2 (3), 2000.

[89] Nicolas Sangouard, Christoph Simon, Hugues de Riedmatten, and Nicolas Gisin. Quantum repeaters based on atomic ensembles and linear optics. *Review of Modern Physics*, 83, 2011.

[90] H. J. Kimble. The quantum internet. *Nature*, 453, 2008.

[91] J. Sidhu, S. Joshi, and M. Gundogan. Advances in space quantum communications. *Quantum Communication*, 4:182–217, 2021.

[92] A. Ejlli, F. Della Valle, and G. Zavattini. Polarisation dynamics of a birefringent fabry–perot cavity. *Applied Physics B*, 124, 2018.

[93] K. Kowalik, O. Krebs, A. Lemaître, S. Laurent, P. Senellart, P. Voisin, and J. A. Gaj. Influence of an in-plane electric field on exciton fine structure in inas-gaas self-assembled quantum dots. *Applied Physics Letters*, 86 (4), 2005.

[94] W. Langbein, P. Borri, U. Woggon, V. Stavarache, D. Reuter, and A. D. Wieck. Control of fine-structure splitting and biexciton binding in ingaas quantum dots by annealing. *Phys. Rev. B*, 69, 2004.

APPENDICES

Appendix A

Gas Tuning

The cryostat and the nitrogen gas injection setup are shown in Figure A.1. Nitrogen gas is initially prepared into a Swagelok DOT-3E-1800 gas reservoir and injected into the cryostat by a Bronkhorst EL-FLOW Prestige FG-200CV digital gas flow controller connected to a lab computer.

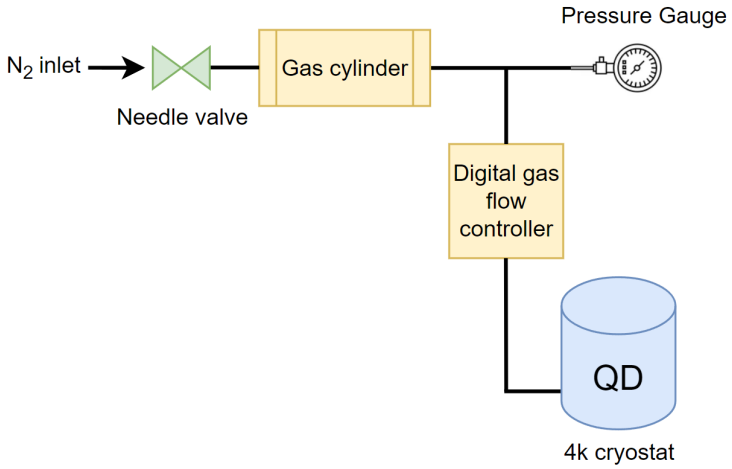


Figure A.1: Diagram of nitrogen gas flow setup.

A.1 Gas tuning procedure

This section aims to provide a brief outline on the gas tuning procedure:

1. To begin, save a spectrum of the QD. This is to provide an initial reference to the QD emission wavelengths.
2. In the EL-FLOW controller software, begin logging of the gas flow volume.
3. Prepare a stopwatch such as that on your phone
4. Set the gas flow rate to it's maximum of 0.7 mln/min, BUT DO NOT press enter yet to start the gas flow.
5. Start the gas flow by pressing enter AND starting the stopwatch at the same time.
6. Once gas injection has occurred over the desired duration, set the gas flow rate to 0, and stop logging. (We often inject gas for 0.5-3 minutes, and the longest duration was up to 10 minutes). You may also stop the stopwatch.
7. Obtain another spectrum of the QD to log the shift in wavelength.

Appendix B

EOM Bias Controller Circuit and Code

B.1 The Bias Controller Circuit

B.1.1 Symmetry Testing

The symmetry testing logic is based on using MOSFETs to split the signal into positive and negative peaks. An example input and resulting output of peak splitting is shown in Figure B.1.

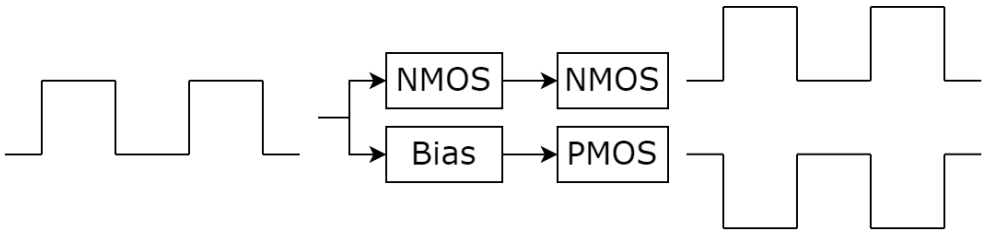


Figure B.1: Peak splitting.

The results from the peak splitting are then used to determine symmetry by the logic in Figure B.2.

The PCB schematics used for symmetry testing is finally shown in Figure B.3

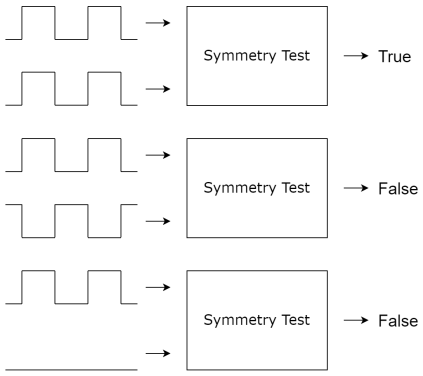


Figure B.2: Symmetry testing logic

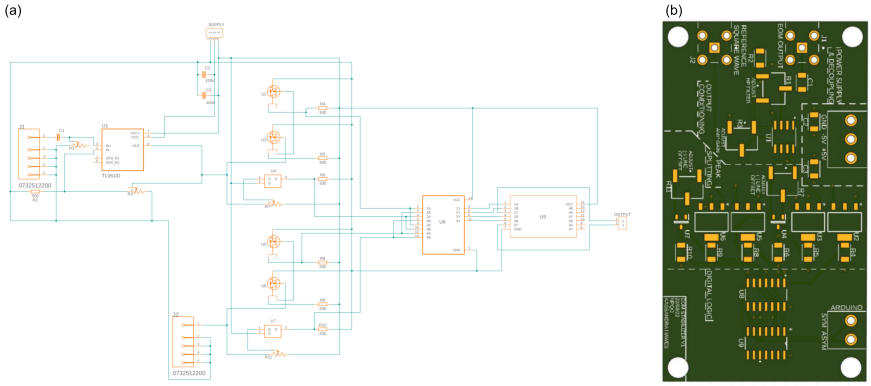


Figure B.3: PCB for symmetry testing, initially designed by Kassandra Hawes, then modified to fix some connections at the logic gates. (a) Schematic Diagram. (b) Resulting Board.

B.1.2 The Arduino and DAC Circuit

An Arduino's digital IO port was used to read out the symmetry logic, and the bias voltage was also continuously generated by the Arduino through an MCP4725 12-Bit DAC. The PCBs described above in Figure B.3 only contained the symmetry testing logic, so a separate board had to be made to combine the square wave dither and DAC signal. The circuit is shown in Figure B.4. A square wave ranging from 0V to 5V is directly generated by the Arduino. This signal is then converted into a -5V to 5V square wave using a comparator. A portion of the -5V to 5V signal is sent to the symmetry testing PCB, while another part is branched off into a voltage divider to create a small dither signal. Subsequently, a non-inverting summing amplifier combines the DAC signal and

dither signal to feed into the EOM DC port.

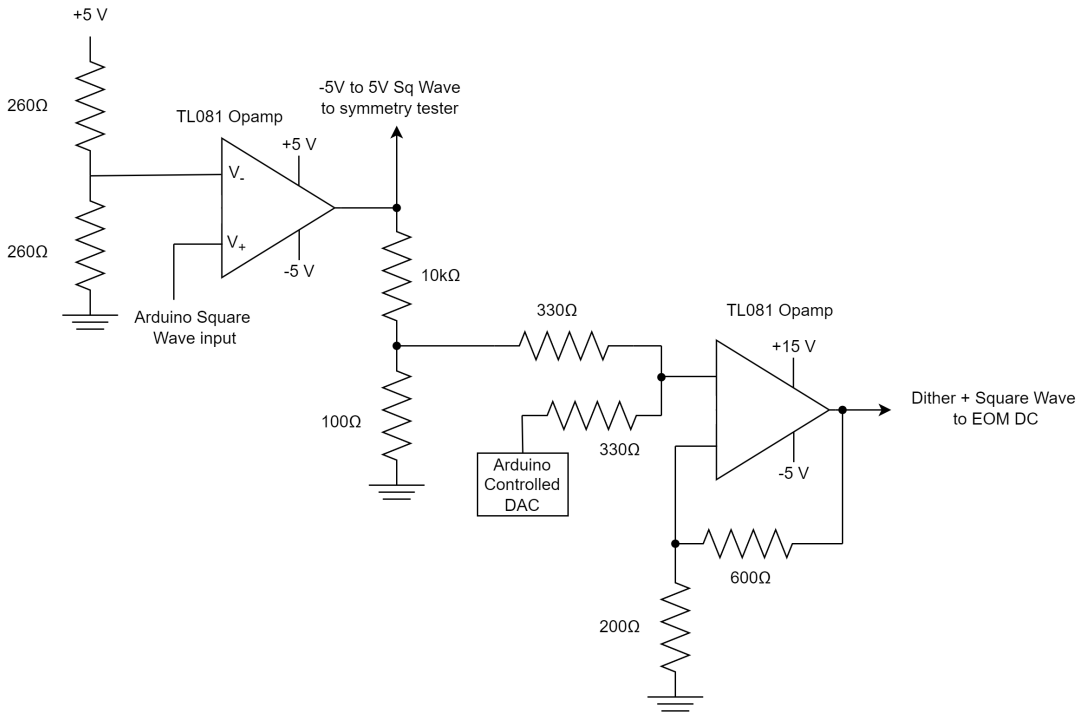


Figure B.4: Circuit to combine square wave dither and DAC.

B.1.3 The Enclosure

All the circuits are housed inside a 3D printer enclosure as shown in Figure 2.10(a). A diagram of the ports used for the enclosure is shown in Figure B.5. The front side of the enclosure includes all the inputs, such as the EOM's output signal as measured on a photodetector, and the square wave dither. Additionally, the front side contains the power supply inputs for the circuits. From left to right, the DC power supply provides mutual ground, 5V, -5V, and 15V DC for the op-amps. The bottom of the enclosure has openings for powering the Arduino via a barrel plug and for reprogramming the stabilization code through the Arduino USB port. The backside of the enclosure houses the output signals, including the dither generated from the Arduino and the output DC voltage for the EOM.

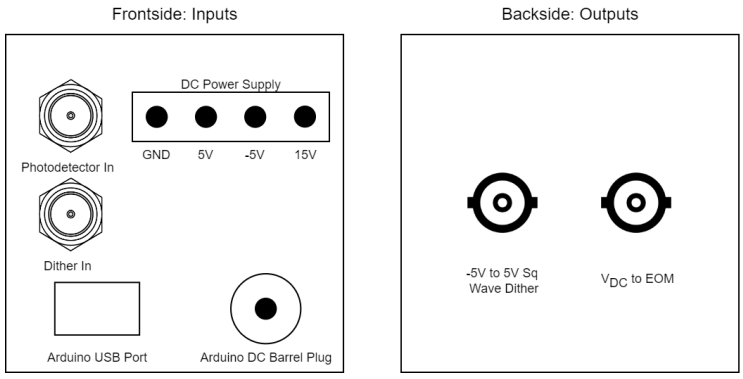


Figure B.5: Layout of front and backside electrical ports for the bias controller circuit.

B.2 Arduino Control Code

Below is the code used to determine the adjusted bias voltage. The initial voltage VDAC is set to around 3.06, determined by finding a rough minimum on a DC power supply. It then continuously checks for the results of symmetry testing and adjusts VDAC by 0.001 in each iteration.

```
#include <Wire.h>
#include <Adafruit_MCP4725.h>
#include <math.h>


// Define Pins
#define PWM_pin 6
int symmTestPin = 8;
int asymmTestPin = 7;
const int pin5V = 13;


int symmTestVal = 0;
int asymmTestVal = 0;

// Global Variables
float pid_increment = 0.001;  //Empirically determined, originally 0.01, for
end product use 0.001
int lockMinOrMax = 0;        // 0 = lock to min, 1 = lock to max
float V_DAC = 3.06;           //Voltage sent to DAC for correction factor,
Initial value empirically determined. Use 3.2 for min, 1 for max


Adafruit_MCP4725 dac;


void setup() {
  Serial.begin(9600);

  // Setup one output to 5v as the 5v on board supply is blocked by the protoboard
  in the enclosure
```

```
  pinMode(pin5V, OUTPUT);
  digitalWrite(pin5V, HIGH);

  // DAC Setup
  dac.begin(0x62);
  Serial.println("DAC began");

  // Create Square Wave on pin PWM_pin
  pinMode(PWM_pin, OUTPUT);
  float freq = 1 * pow(10, 3);  //Hz
  Serial.print("Frequency = ");
  Serial.println(freq);
  tone(PWM_pin, freq);  //creates square wave dither, works for 50Hz to 50kHz

  // Symmetry Test Pin Setup
  pinMode(symmTestPin, INPUT);
  pinMode(asymmTestPin, INPUT);


  // Set Initial Voltage
  setDACVoltage(V_DAC);
}

void loop() {
  //Use DAC to output a correction factor
  V_DAC = correctionFactor(V_DAC);

  setDACVoltage(V_DAC);  // Need to find 0.4 for max lock
  // setDACVoltage(3);

  delay(100);
  Serial.println("-------------------------------------");
}


void setDACVoltage(float V) {
  float setValue = (V)*4095 / 5;
  dac.setVoltage(setValue, false);  //analog value, if it should be stored for reset
```

```
  Serial.print("DAC V = ");
  Serial.print(V);
  Serial.print(", DAC sent ");
  Serial.println(setValue);
}

void setDACBit(float setValue) {
  dac.setVoltage(setValue, false);  //analog value, if it should be stored for reset
  float V = setValue * 5 / 4095;
  Serial.print("DAC V = ");
  Serial.print(V);
  Serial.print(", DAC sent ");
  Serial.println(setValue);
}


float correctionFactor(float currentVoltage) {
  float correctedVoltage;
  symmTestVal = digitalRead(symmTestPin);
  asymmTestVal = digitalRead(asymmTestPin);

  Serial.print("ASymm Test ");
  Serial.println(asymmTestVal);


  Serial.print("Symm Test ");
  Serial.println(symmTestVal);

  if (symmTestVal == 1 && asymmTestVal == 0) {
    correctedVoltage = currentVoltage - pow(-1, lockMinOrMax) * pid_increment;
    // - for min, + for max
    Serial.println("Right of Medium");

  } else if (symmTestVal == 0 && asymmTestVal == 1) {
    correctedVoltage = currentVoltage + pow(-1, lockMinOrMax) * pid_increment;
    Serial.println("Left of Medium");
```

```
  } else if (symmTestVal == 1 && asymmTestVal == 1) {
  // Error Catching
    Serial.println("Error, symm = asymm = 1");

  } else {
    correctedVoltage = currentVoltage;
    Serial.println("Good Correction");
  }

  // Catch edge cases where voltage excedes DAC bounds
  float upperBound = 4.9;
  float lowerBound = 0.2;

  if (correctedVoltage > upperBound) {
    correctedVoltage = upperBound;
    Serial.println("Error, DAC can't set voltage > upper bound");
  }

  if (correctedVoltage < lowerBound) {
    correctedVoltage = lowerBound;
    Serial.println("Error, DAC can't set voltage < lower bound");
  }

  return correctedVoltage;
}
```

Appendix C

Picosecond Pulse Generator Characterization

The effect of using three different resistors to control pulse lengths was tested; however, this approach is tedious and should be avoided if possible. The resistors are only 0603 in size and are housed in a sensitive and fragile enclosure. The initially used resistor was 50 Ω, as this was the value in the work by Zou et al. [1]. The 50 Ω resistor produced pulse widths of 260 ps. In an effort to decrease the pulse width to 100 ps, we replaced it with a 750 Ω resistor, and finally with a 1.5k Ω resistor. The pulse shapes for the same 120 MHz sine wave input are shown in Figure C.1.

In addition to the resistor value, there are several parameters that influence the resulting electrical pulse from the pulse generator, such as the repetition rate, trigger pulse amplitude, pulse shape, and DC bias of the trigger signal. Moreover, the optical pulse from the EOM also depends on the amplifier settings used to convert the pulse generator's output to a V_π amplitude of about 5V. With a 1.5 kΩ R2, a lookup table detailing the various achievable optical pulse shapes from the EOM is outlined below in Table C.1 and Table C.2.

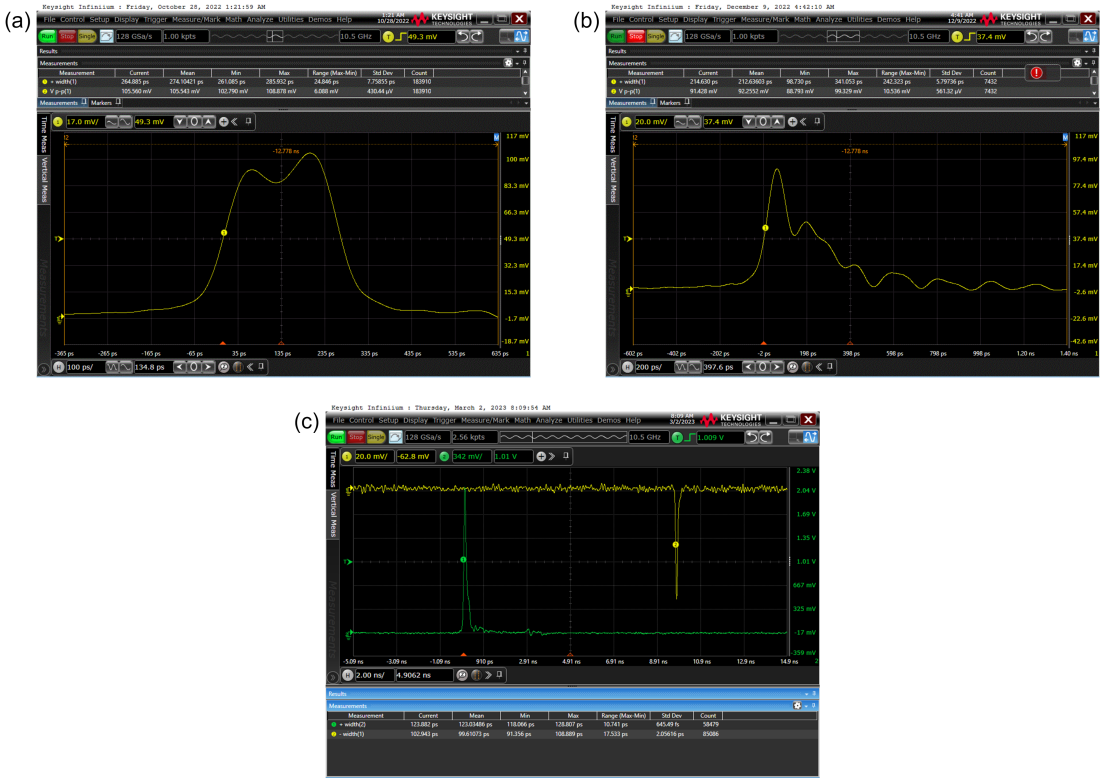


Figure C.1: Effects of changing R2 in Figure 2.11 on pulse widths: $R_2 = 50\ \Omega$ (a), 750 Ω (b), 1.5k Ω (c), resulting in pulse widths of 260 ps, 200 ps, and 100 ps, respectively. Panels (a) and (b) only show the electrical pulse from the pulse generator (yellow), whereas panel (c) also includes the derived optical pulse from the EOM (green).

Pico Pulse Generator				Amplifier				Output (To EOM)	
Funcion Generator Sine Input			DC Input						
Freq (MHz)	Amplitude (Vpp)	Offset (Vdc)	Vdc	Ch1 Voltage	Ch1 Current	Ch2 Voltage	Ch2 Current	Pulse Width (ps)	Pulse Amplitude (Vpp)
50	4	0	-3.5	0.43	0	12	0.284	225	1.23
50	5	0	-3.5	0.43	0	12	0.284	144	2.8
10	10	0	-3.5	0.43	0	12	0.284	241	4.05
20	10	0	-3.5	0.43	0	12	0.284	213	4.43
30	10	0	-3.5	0.43	0	12	0.284	185	4.46
40	10	0	-3.5	0.43	0	12	0.284	156	4.3
50	4	0.25	-3.5	0.43	0	12	0.284	159	2.26
50	5	0.25	-3.5	0.43	0	12	0.284	131	3.11
50	4	0.5	-3.5	0.43	0	12	0.284	131	2.65
50	5	0.5	-3.5	0.43	0	12	0.284	125	3.23
90	5	0.6	-3.5	0.43	0	12	0.284	101	1.91
100	5	0.6	-3.5	0.43	0	12	0.284	99	1.78
80	5	0.7	-3.5	0.43	0	12	0.284	104	2.5
50	4	0.75	-3.5	0.43	0	12	0.284	122	2.75
50	5	0.75	-3.5	0.43	0	12	0.284	116	3.2
50	5	0.8	-3.5	0.43	0	12	0.284	122	3.35
60	5	0.8	-3.5	0.43	0	12	0.284	111	2.96
70	5	0.8	-3.5	0.43	0	12	0.284	104	2.67
10	2	1	-3.5	0.43	0	12	0.284	Poor Signal	Poor Signal
20	2	1	-3.5	0.43	0	12	0.284	Poor Signal	Poor Signal
30	2	1	-3.5	0.43	0	12	0.284	Poor Signal	Poor Signal
40	2	1	-3.5	0.43	0	12	0.284	Poor Signal	Poor Signal
50	2	1	-3.5	0.43	0	12	0.284	Poor Signal	Poor Signal
60	2	1	-3.5	0.43	0	12	0.284	Poor Signal	Poor Signal
70	2	1	-3.5	0.43	0	12	0.284	Poor Signal	Poor Signal
80	2	1	-3.5	0.43	0	12	0.284	Poor Signal	Poor Signal
10	3	1	-3.5	0.43	0	12	0.284	Poor Signal	Poor Signal
20	3	1	-3.5	0.43	0	12	0.284	267	1.37
30	3	1	-3.5	0.43	0	12	0.284	212	1.7
40	3	1	-3.5	0.43	0	12	0.284	165	1.84
50	3	1	-3.5	0.43	0	12	0.284	122	1.73
60	3	1	-3.5	0.43	0	12	0.284	112	1.53
70	3	1	-3.5	0.43	0	12	0.284	106	1.31
80	3	1	-3.5	0.43	0	12	0.284	100	1.22
10	4	1	-3.5	0.43	0	12	0.284	343	1
20	4	1	-3.5	0.43	0	12	0.284	230	2.48
30	4	1	-3.5	0.43	0	12	0.284	180	3.03
40	4	1	-3.5	0.43	0	12	0.284	138	2.98
50	4	1	-3.5	0.43	0	12	0.284	116	2.69
60	4	1	-3.5	0.43	0	12	0.284	107	2.39
70	4	1	-3.5	0.43	0	12	0.284	102	2.09
80	4	1	-3.5	0.43	0	12	0.284	99	1.97
10	5	1	-3.5	0.43	0	12	0.284	290	1.81
20	5	1	-3.5	0.43	0	12	0.284	213	3.44
30	5	1	-3.5	0.43	0	12	0.284	170	3.58
40	5	1	-3.5	0.43	0	12	0.284	136	3.52
50	5	1	-3.5	0.43	0	12	0.284	117	3.25
60	5	1	-3.5	0.43	0	12	0.284	109	2.90
70	5	1	-3.5	0.43	0	12	0.284	103	2.55
80	5	1	-3.5	0.43	0	12	0.284	101	2.4
20	7	1.5	-3.5	0.43	0	12	0.284	198	4.2

Table C.1: Pico pulse generator characterization with a sine wave input.

Pico Pulse Generator					Amplifier				Output (To EOM)	
Funcion Generator Sq Input				DC Input						
Freq (MHz)	Amplitude (Vpp)	Offset (Vdc)	Duty%	Vdc	Ch1 Voltage	Ch1 Current	Ch2 Voltage	Ch2 Current	Pulse Width (ps)	Pulse Amplitude (Vpp)
20	5	2.5	50	-3.5	0.43	0	12	0.284	190	4.5
20	4	2.5	50	-3.5	0.43	0	12	0.284	156	4.3
20	3	2.5	50	-3.5	0.43	0	12	0.284	No Signal	No Signal
10	10	0	50	-3.5	0.43	0	12	0.284	225	4.4
30	5	2	50	-3.5	0.43	0	12	0.284	150	4.2
50	5	2.5	30	-3.5	0.43	0	12	0.284	143	4.4
50	5	2	30	-3.5	0.43	0	12	0.284	135	4
80	5	1.4	30	-3.5	0.43	0	12	0.284	113	2.9

Table C.2: Pico pulse generator characterization with a square wave input.

Appendix D

Fine Structure Splitting Data of 16 Quantum Dots

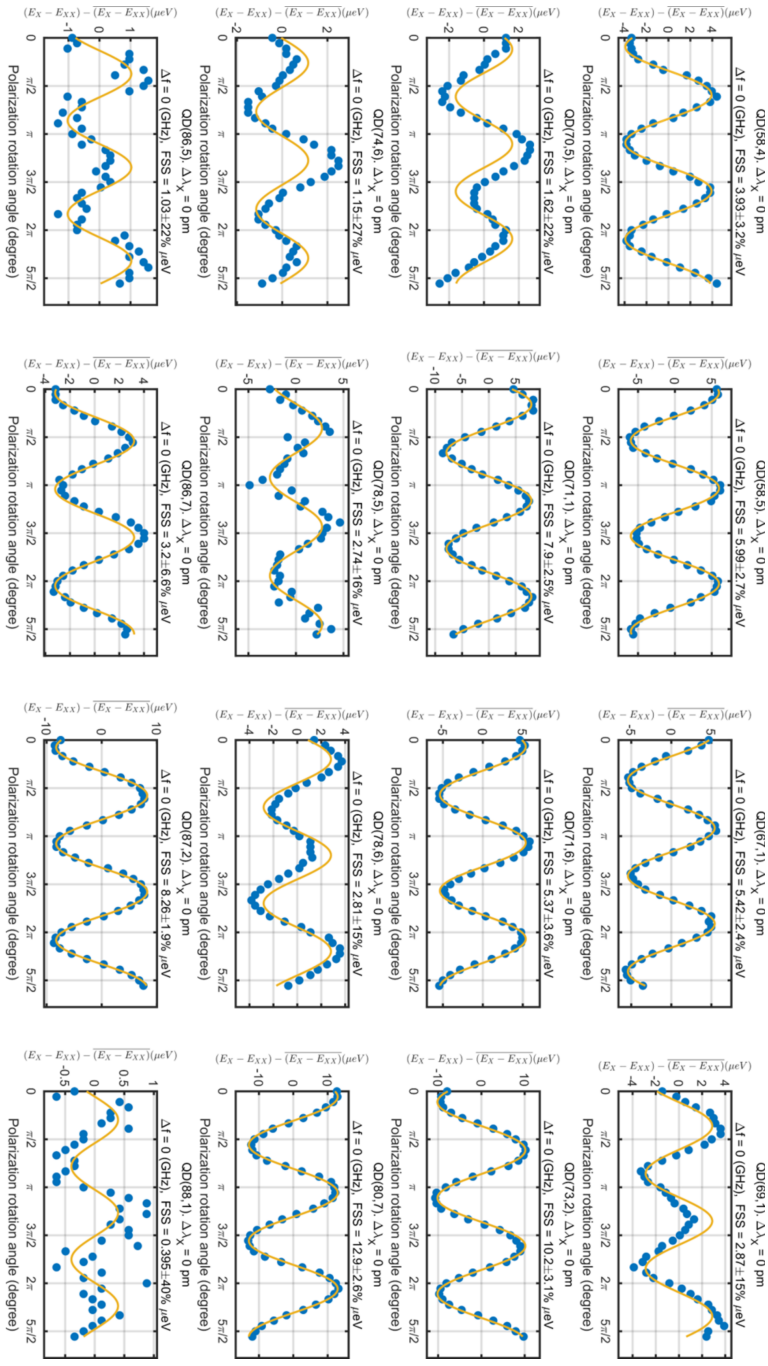


Figure D.1: FSS data of 16 Quantum Dots measured before gas tuning.

	0 min	6 min	12 min	18 min	24 min	30 min
58, 4	3.936481	3.735471	3.868337	3.638804	3.592724	3.680424
58, 5	5.998044	6.16657	6.276283	6.422154	6.258437	6.611689
67, 1	5.448979	5.410199	5.597354	5.496835	5.491174	5.232878
69, 1	3.649003	3.236517	2.557504	2.753438	2.520352	2.274348
70, 5	2.65438	2.507336	2.805575	2.82314	2.398932	3.06634
71, 1	7.903735	7.945758	7.937905	8.160827	7.657591	8.094058
71, 6	5.371174	4.281702	5.097334	4.892776	4.456708	4.209597
73, 2	10.1562	9.203502	9.554256	9.605671	8.962942	9.686877
74, 6	2.463692	2.394683	2.803712	2.304623	2.846069	2.547725
78, 5	3.1354	3.518122	2.79233	3.25382	3.751614	4.12876
78, 6	3.049908	2.900285	2.438899	1.898936	1.637812	1.380757
80, 7	12.94198	13.08102	12.54766	12.8961	13.58913	14.04621
86, 5	1.032506	1.094254	1.275341	1.767363	1.560276	1.657172
86, 7	3.236521	2.917981	3.071619	3.26149	3.593149	3.630801
87, 2	8.25712	8.206881	8.522704	8.818956	9.022398	9.15424
88, 1	0.448807	0.883039	0.88367	0.867801	0.936374	1.170883

Table D.1: FSS data from Figure 3.5 over all 6 stages of gas injection for 16 QDs. All data presented in μeV.

	0 min	6 min	12 min	18 min	24 min	30 min
58, 4	0	7.603082	40.4164	67.87814	97.368	120.8287
58, 5	0	3.49926	33.7916	70.4884	107.7203	131.3287
67, 1	0	8.456537	51.00763	85.55793	112.0651	135.955
69, 1	0	8.868367	39.38514	82.50142	118.7848	149.6977
70, 5	0	4.503394	18.1269	41.69854	64.03461	83.59519
71, 1	0	6.636633	33.18579	61.46452	90.08565	115.1472
71, 6	0	6.975709	24.26622	55.77629	93.22095	123.3553
73, 2	0	9.831279	51.1813	85.73473	113.5247	138.8502
74, 6	0	4.597456	14.05655	35.57704	66.90162	95.47956
78, 5	0	7.022316	28.7707	65.66632	97.24362	122.5928
78, 6	0	7.141625	12.54528	26.60315	48.78825	67.46077
80, 7	0	6.760528	18.8926	41.84453	59.08871	80.76856
86, 5	0	7.327547	22.47216	63.25291	96.93738	146.9502
86, 7	0	7.036779	13.92413	52.33376	82.25146	105.77
87, 2	0	11.7641	61.12219	109.1409	150.214	181.1759
88, 1	0	20.47762	91.13903	145.7189	194.6948	232.7012

Table D.2: Detuning data from Figure 3.5 over all 6 stages of gas injection for 16 QDs. All data presented in GHz.

Appendix E

DAVLL Push-fit Baord Design

E.1 DAVLL Board CAD Drawings

Below are the mechanical drawings of various parts of the DAVLL board, measured in millimeters (mm). All components are designed as modular parts, which are assembled by mate constraints along their edges and aligned to center on the optical axis defined by the fiber, together forming the final DAVLL board. Figure E.6 is an example showing the build-up of the module boards constrained to the optical axis. All DAVLL board CAD files will be stored on the main lab computer with the cold atom LabVIEW code, specifically in the folder `\Documents\DAVLL_CAD`. Note that the current push-fit slot tolerances are tuned to my personal 3D printer. If these parts are to be printed on a different 3D printer, the 0.01" tolerances may have to be adjusted, as the stepper motors will have different precision.

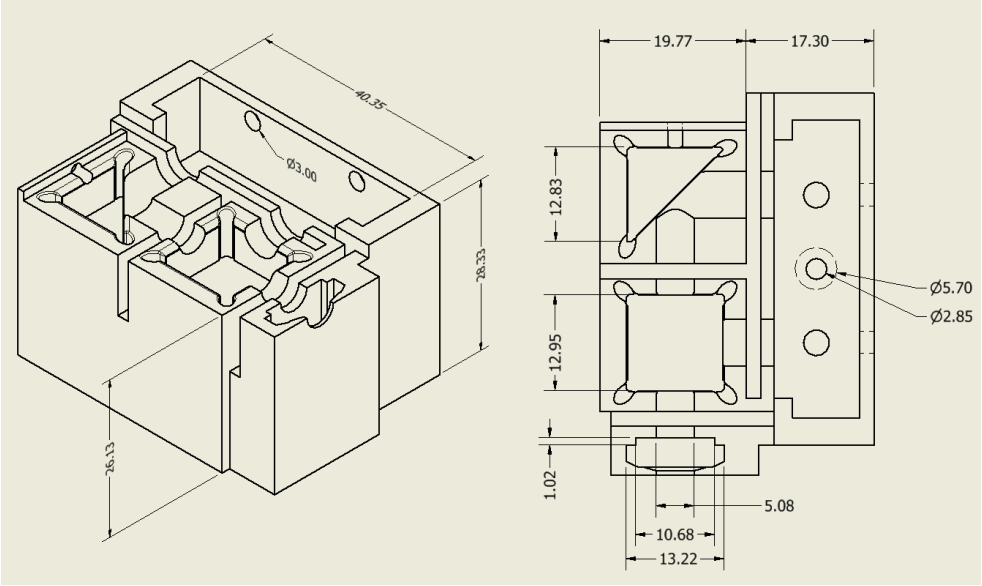


Figure E.1: Slot dimensions for balanced photodetector, polarizing beam splitter, prism mirror and focusing lens.

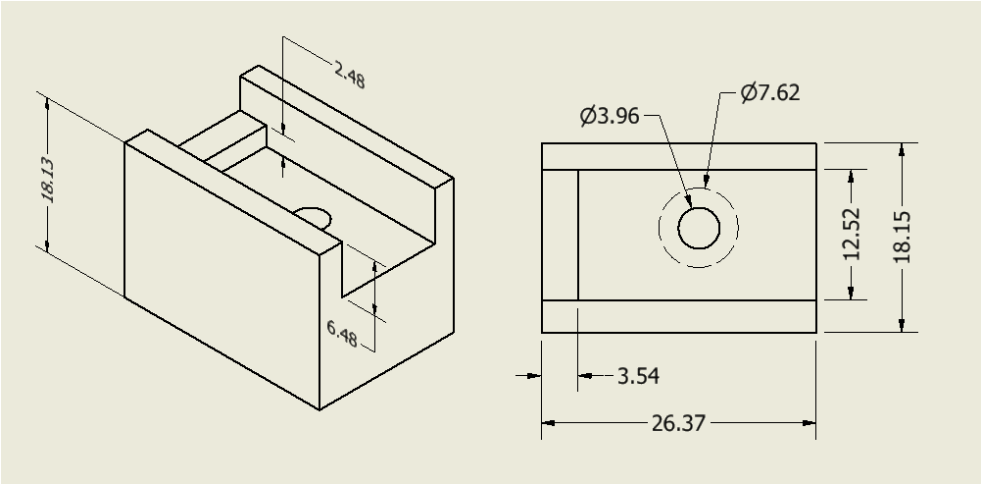


Figure E.2: Dimensions for QWP mount.

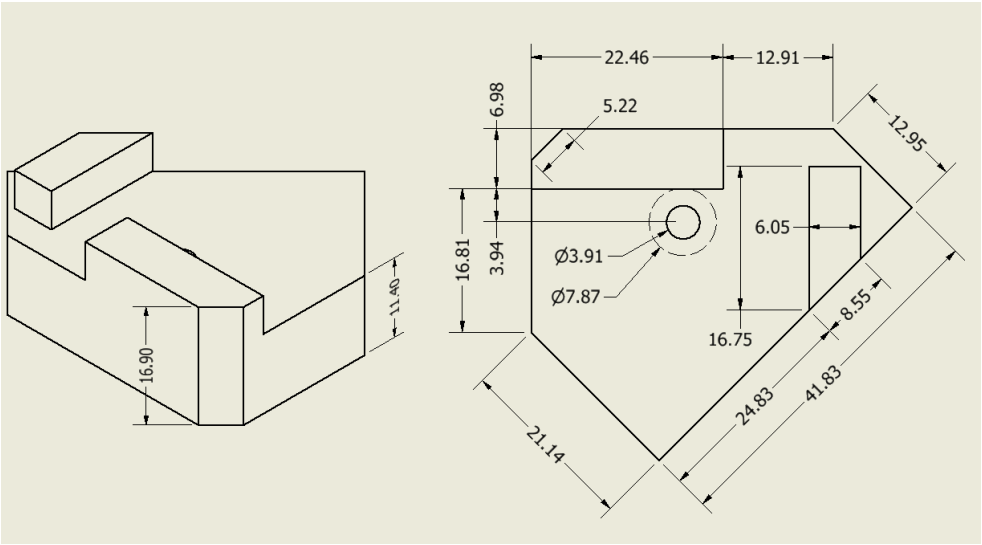


Figure E.3: Dimensions for dichroic mirror mount.

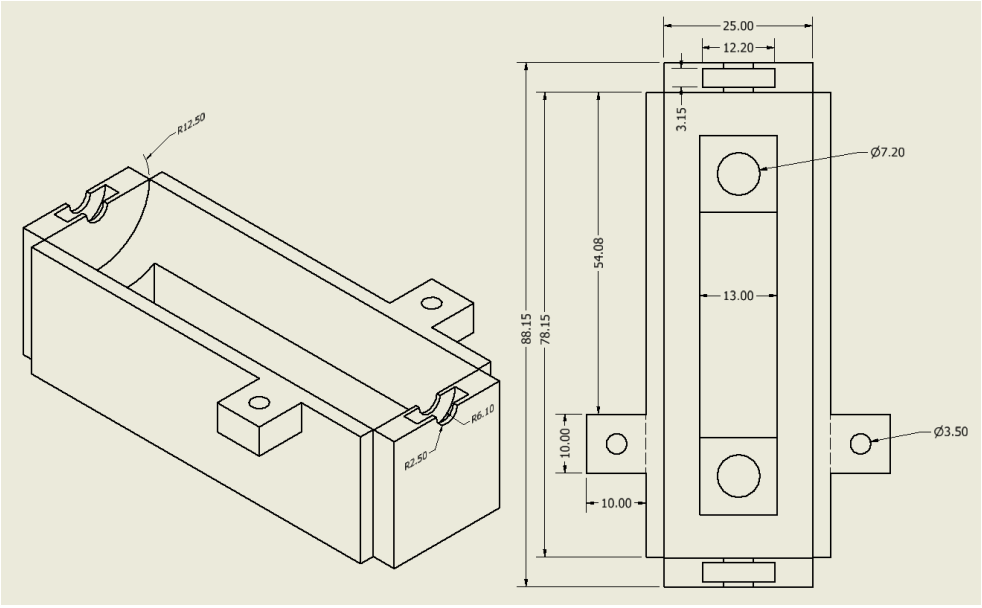


Figure E.4: Dimensions for Cs cell holder.

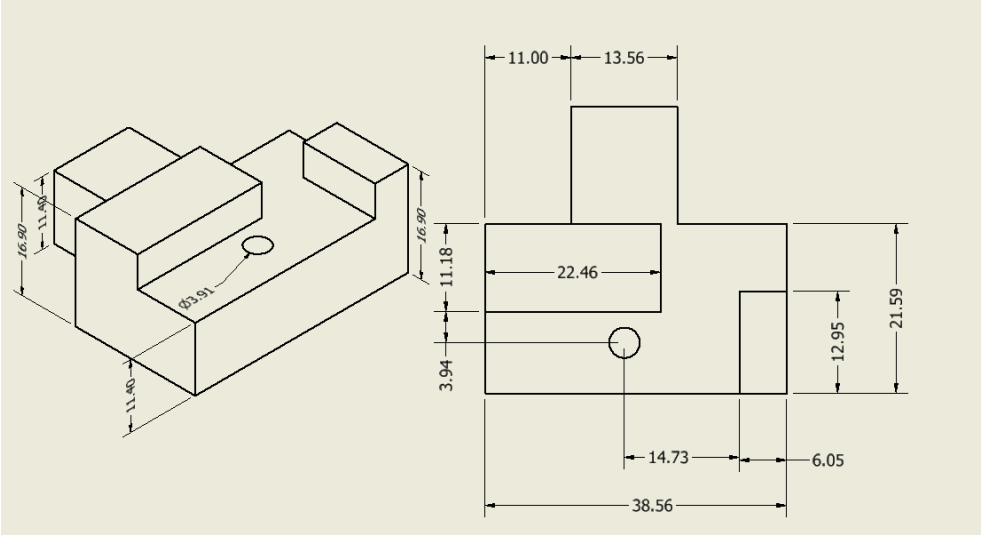


Figure E.5: Dimensions for fiber adapter mount.

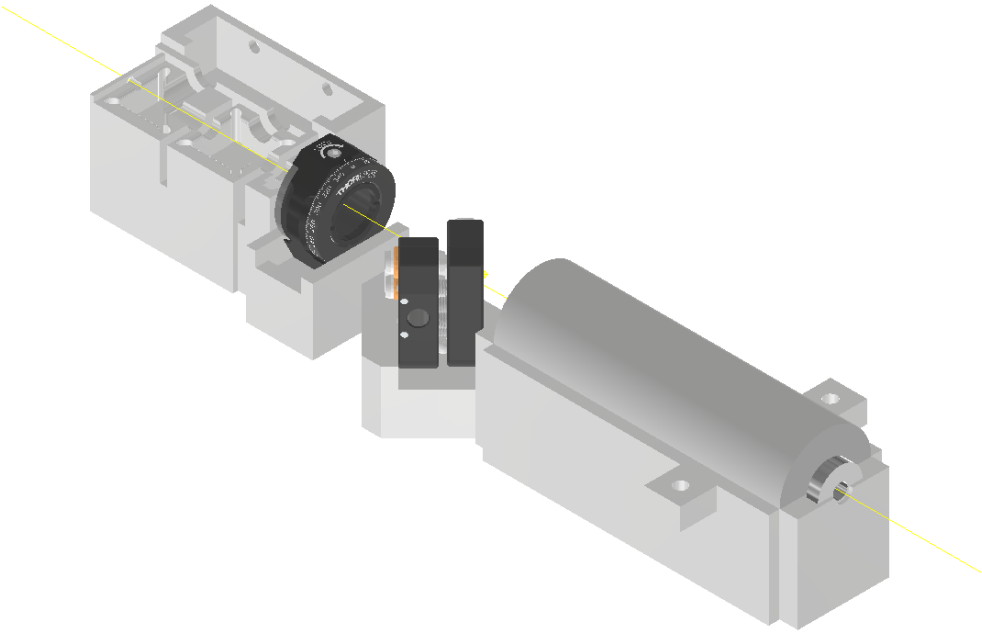


Figure E.6: The Koheron Photodetector module, QWP module, DM module and Cs cell holder module mated together by the optical axis (yellow line) and by their edges.

E.1.1 Push-fit Slots

Components such as the balanced photodetector, prism mirror and PBS are slotted directly into the 3D printed structures as shown in Figure E.7.

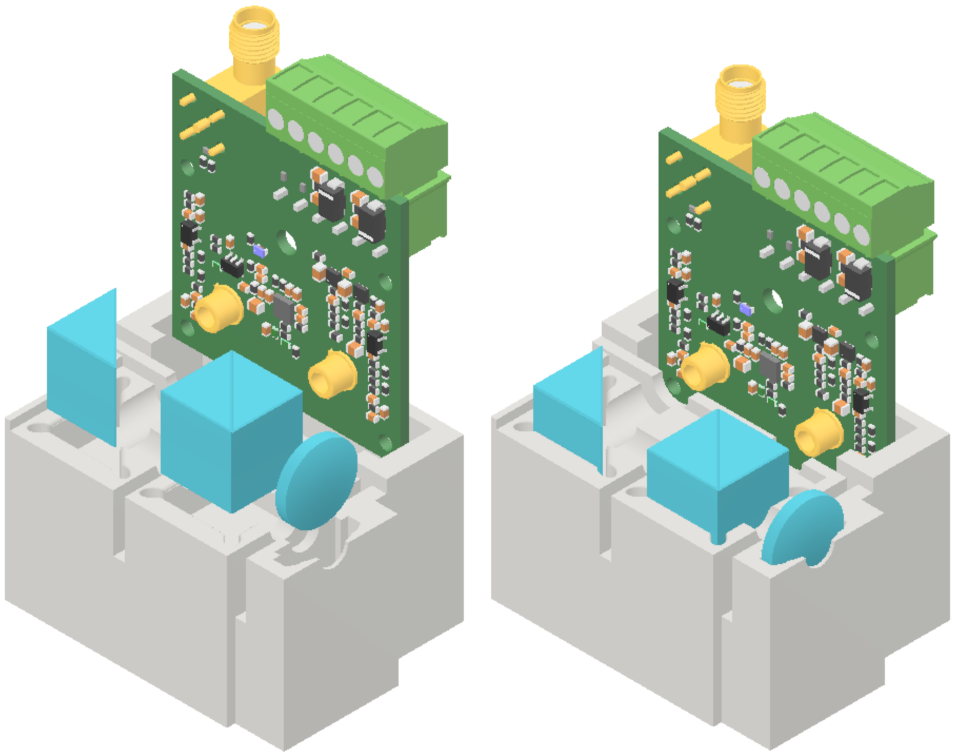


Figure E.7: Illustration of push-fit mechanism. These parts are meant to be secured by the 3D printed board itself.

E.2 Beam Focusing

A lens is used to focus the probe beam onto the photodetectors, with the additional goal of ensuring that the spot size at both detectors are the same. However, it was only towards the end of my degree that we noticed the current setup was incorrect. At the time of writing, a Thorlabs LA1289-B f=30 mm lens was selected to focus the beam midway between the PBS and PM. This now seemingly obvious mistake resulted in different beam sizes at the

detectors, as the focal point of the PBS path does not match that of the PM. The current setup is shown in Figure E.8(a). This difference in spot size was not noticeable visually, and we may have unknowingly compensated for it by adjusting the QWP angle. A correct setup is instead proposed in Figure E.8(b). By using a different Thorlabs LA1213-B f=49.8 mm lens and position, we designed the focal point to be 10 mm behind the detector aligned to the PBS, and 10 mm ahead of the detector aligned to the PM. This should correctly adjust the spot size at the two detectors.

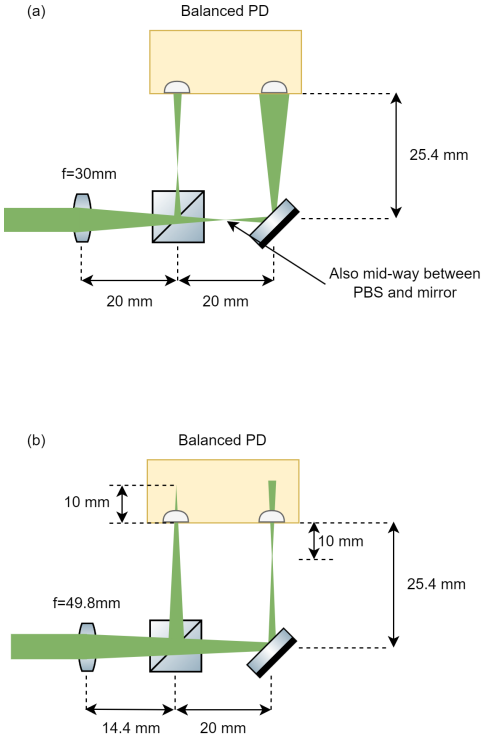


Figure E.8: (a) Illustration showing the current incorrect lens position and focal length, with the lens's focal point midway between the PBS and the prism mirror. (b) Proposed corrected setup using a 49.8 mm lens, with the focal point positioned 10 mm before and after the respective photodetectors. Note: beam sizes are not to scale.

Appendix F

Filters for Cs Hyperfine Transitions

As alluded to in Figure 5.1(b), for the EIT memory there is a need for a high-contrast filter to eliminate the control beam so that only the probe signal remains. This is especially crucial when experiments operate at single-photon levels, as any additional background noise from the strong control fields may overwhelm the signal and compromise measurement fidelity. Since the pump and control are separated by only 9 GHz, traditional frequency filtering methods such as dichroic mirrors or gratings typically cannot distinguish between the two frequencies. Throughout the EIT memory project, five different filters were tested; however, only the currently used double-pass 895 nm etalon provides sufficient contrast between the two ground states. These filters are mainly characterized by their efficiency, defined by probe transmission, and contrast, defined by the transmission ratio of probe to control.

The first filters immediately tested were a pair of pre-existing etalons used to separate the $6S_{1/2}$ hyperfine ground state transitions to the $6P_{3/2}$ state at 852 nm. Although these two etalons were technically designed for Rb at 794 nm, they also work decently at 852 nm. These are commonly used for the cold atom experiments in the lab, and the idea was to frequency tune the resonance to 894 nm by changing the piezo and temperature[1]. The beam diagram and experimental setup are shown in Figure F.1. Typically, when set to 852 nm, the transmission is $\sim$25% and the contrast is $\sim$8000. However, once moved to 894 nm, the contrast decreased to only 50. This decrease in contrast is likely due to a decrease in mirror reflection and finesse as we start to move far away from the central frequency of 794 nm. This contrast is too low, so other methods of filtering had to be investigated.

[1]The piezo changes the length of the FP cavity, while the temperature slightly modifies the refractive index of the material. Both shift the resonance by changing the effective optical path length of the cavity.

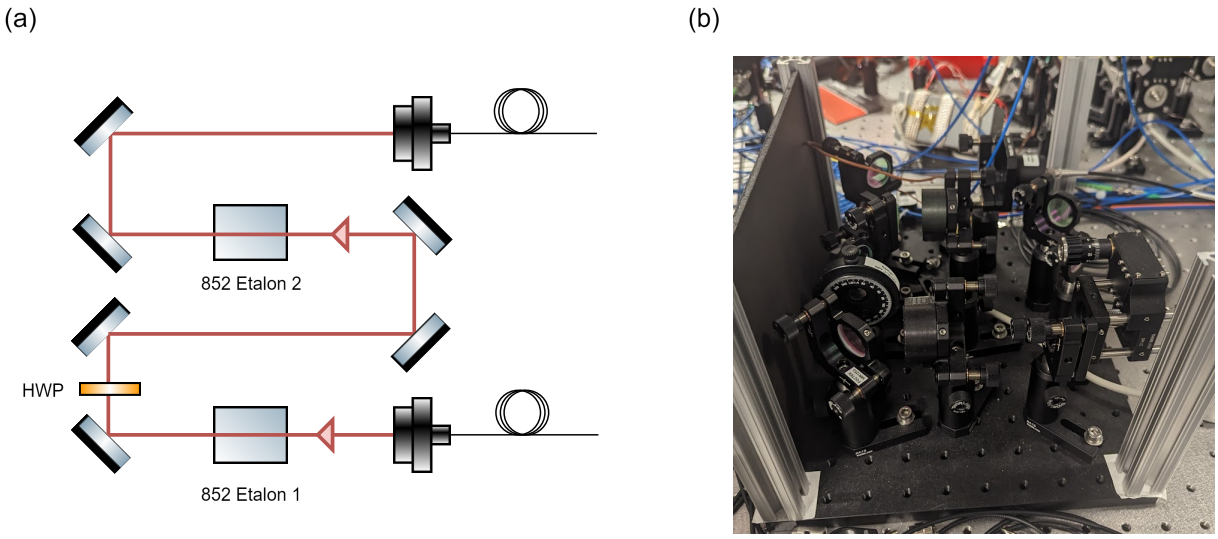


Figure F.1: Setup for 852 nm etalons. (a) Beam diagram showing signal passing through two Vitawave etalons at 852 nm. Etalon 1 has a finesse of F = 15 at 852 nm, while Etalon 2 has a specification of F = 17 at 852 nm. (b) Experimental setup in the lab.

A second option was to use the monochromator path in the QD spectrometer setup, as shown in Figure 2.6. This setup was designed to for dual purpose, and by removing a flip mount, a narrow frequency selection of light is fiber-coupled into a PM fiber to act as a monochromator. This setup supposedly gave a contrast of about 100. However, during testing, we found a steady 60 Hz noise at the output, completely overwhelming any signal that could be measured through the vapor cell. An example of the noise is shown in Figure F.2. The top plot shows the typical absorption spectrum of the 894 nm F=4 to F'=3 transition measured on SNSPDs, while the bottom plot shows the same signal sent through the monochromator before reaching the SNSPD. One would expect the bottom signal to be convoluted by the filtering of the monochromator; however, it appears as a DC line with steady 60 Hz noise, and the same absorption dip is not detected. Because the noise is so consistently at 60 Hz, it seems to be influenced by some sort of AC electrical signal from outlets. However, even when all electronics were shut off and disconnected, the noise remained. Mechanical vibrations were also tested by tapping the optics table and slightly pushing against the gratings and components, but no additional noise was detected. Stability was tested when the device was first set up many years ago, but this was only done with a power meter and may not accurately reflect the fluctuations observed at the single-photon level. While the source of the issue is still unknown, it became questionable

whether this would be a valuable pursuit, as it would only add an additional contrast of around 100 with extremely low efficiency of approximately 5%. At this point, we had exhausted the existing filtering options in the lab, so we set out to create a new filtering setup.

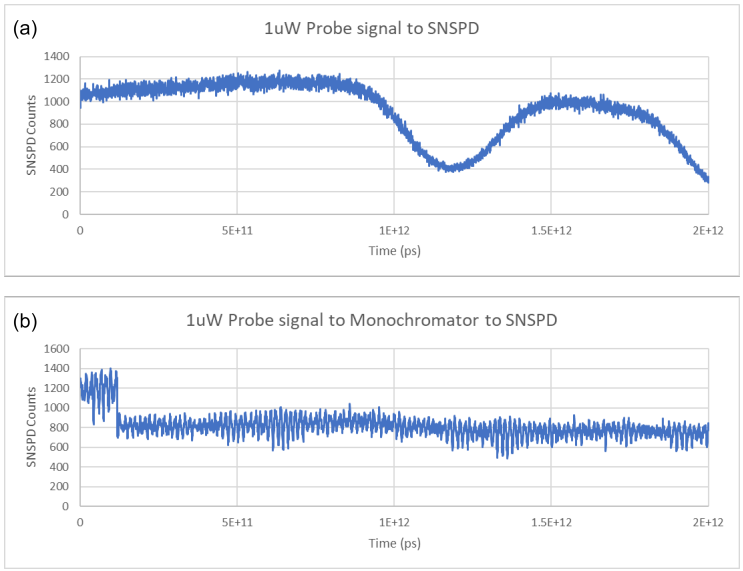


Figure F.2: Noise from monochromator. (a) A typical absorption spectrum of the $6S_{1/2}$, F=4 to $6P_{1/2}$, F'=3 transition. Directly measured on the SNSPDs after the Cs vapor cell. Also see the beginning of the $6S_{1/2}$, F=4 to $6P_{1/2}$, F=4 absorption dip. (b) The same absorption spectrum but now sent through the monochromator before SNSPDs.

A tested setup was to use a separate optically pumped cesium (Cs) cell as the filter. By preparing another Cs cell into a specific hyperfine ground state, we can induce higher absorption on the specific transition of the control beam, while allowing most of the probe beam to pass through. An example of such a scheme is presented in Figure F.3, where we again join two beam paths with a PBS. A strong pump beam from an 852 nm laser, 20-50 μs long, is sent approximately 5 μs before the signal beam. The 852 nm laser is locked to the $6S_{1/2}$, F=4 to $6P_{3/2}$, F'=4 transition to prepare the atoms in the F=3 ground state. The resulting change in the signal field's transmission is shown in Figure F.4. As expected, the transmission of the F=4 to F'=4 transition increased to 70.1%, while the F=3 to F'=4 transmission decreased to 2.2%. However, this only provides a contrast of 30, which is not sufficient. The low contrast, along with the increased experimental complexity of timing an additional pulsed laser and filtering the 852 nm pump beam, was determined to be not worth the effort. One final note is that if the 852 nm pump were switched to the F=3

to F'=4 transition instead, and the probe/control switched transitions, there was an even lower contrast of only 12.

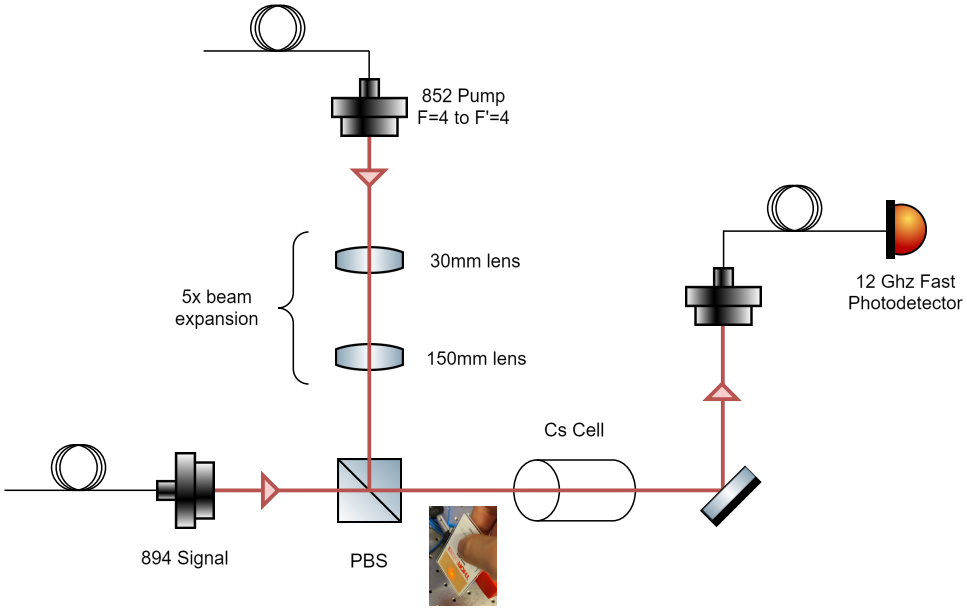


Figure F.3: Setup used for the optically pumped cell filter. The IR card shows the beam size difference of the pump (less intense, ∼1 cm diameter beam) and signal (bright, ∼mm yellow spot). During experiments, both lasers were frequency off-set locked to their respective transitions and pulsed by AOMs.

Another approach involved using new etalons closer to the specified wavelength of 895 nm. This required the machining of a structure to house the etalon and developing a method to tune the resonance frequency of the cavity. This was achieved by machining a circular opening on a smaller piece of aluminum to hold the etalon, and using a Peltier junction attached to a second, much larger aluminum piece, to control the temperature[2]. The metallic piece holding the etalon was also covered with Thorlabs black masking tape to prevent stray reflections off the metallic surface. The resulting mounted etalon is shown in Figure F.5(a). In a single-pass configuration, we observed a contrast of approximately 1300 and an efficiency of 30%. As we were willing to sacrifice efficiency for higher contrast, the filtering was instead set up in a double-pass configuration. However, there is an additional challenge due to the linear polarization rotating by 90 degrees upon reflection. From the

[2]A Peltier junction is a semiconductor-based device that can create a temperature difference across its two sides by an applied electrical current.

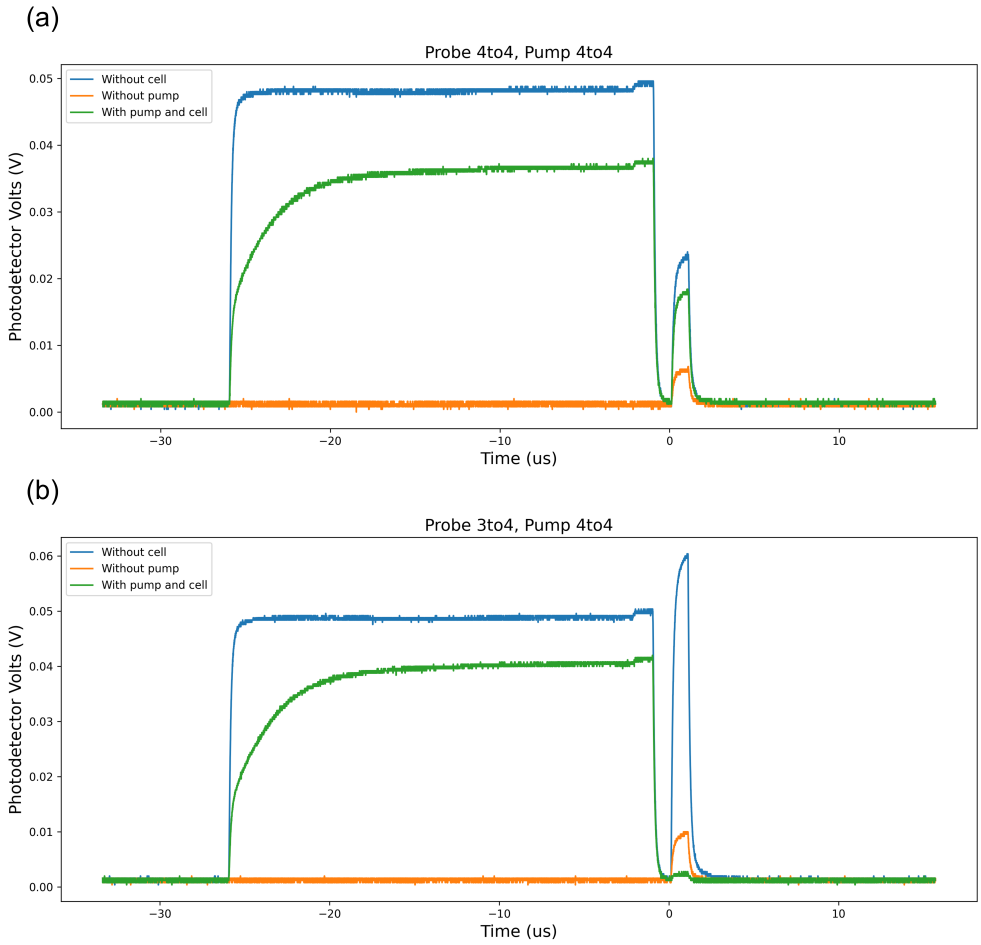


Figure F.4: Result of probe transmission after optical pumping. The first large peak of 25 μs is the pump pulse, and the second short 1 μs pulse is the signal. The blue curve represents a transmission reference for just the probe signal without the Cs cell in the beam path. The orange curve is the absorption profile of the probe signal without any optical pumping. The green curve is the resulting transmission after the cell has been pumped into the F=3 ground state. In the green curves, we also observe a characteristic "bleaching effect", where the transmission of the pump slowly increases over time as more and more of the atomic population is pumped to the other ground state. (a) For a probe signal on the $6S_{1/2}$, F=4 to $6P_{1/2}$, F=4 transition. (b) For a probe signal on the $6S_{1/2}$, F=3 to $6P_{1/2}$, F=4 transition.

inevitable birefringence of the cavity mirrors, high Q Fabry-Perot cavities tend to show slightly shifted resonances depending on the polarization [92]. Such polarization-dependent modes in the frequency scans of the cavity are shown in Figure F.5(b). This implies that achieving uniform transmission and contrast for both the first and second passes through the etalon will be challenging to optimize solely through temperature adjustments. For instance, if the etalons were optimized for polarization during the first pass, the back-reflection would occur at the edge of the cavity mode. However, a slight misalignment of the second pass relative to the first could potentially adjust the cavity length, thereby enhancing contrast and efficiency during the second pass, despite the etalon's prior optimization for first-pass polarization. In the second pass, we observed an additional contrast of 500 and efficiency of 15%, leading to an overall contrast of approximately 600,000 and efficiency of 5%. This, in addition to the rough contrast of 100 obtained from polarization filtering, pushed us to an acceptable magnitude of filtering, and we were able to observe our first lambda EIT linewidth with this setup, as discussed in detail in Section 5.3.

Although rare, one may also move to a ladder system for memory. Ladder systems remove the need for filtering as the pump is now counter-propagated to maintain two-photon detuning of zero, and achieve a faster switching protocol. However, this comes with the trade-off of shorter storage times due to the rapid decoherence of the excited state in a ladder system [36].

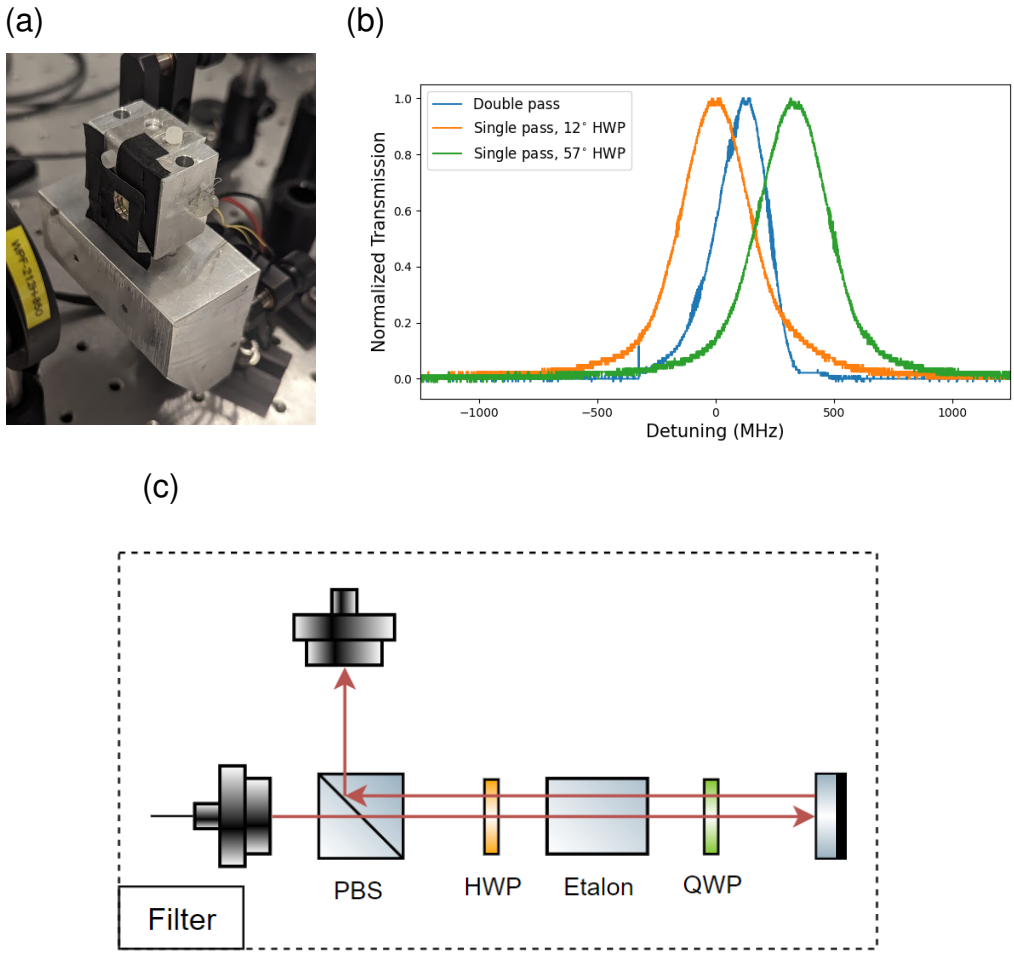


Figure F.5: The newly setup 895 etalons used as a narrow bandpass filter to control beam. (a) The mounted 895 nm etalon in a custom made heater. The temperature is stabilized with a temperature controller. Located on the side of the mount is a hole designed to house a temperature probe, which provides feedback to the temperature controller. (b) Normalized transmission profiles of the etalon filter. Blue represents the filtering when used in a double-pass configuration as shown in Figure 5.2, where the polarization in the first pass and second pass are both linear but orthogonal. The orange and green curves show the exact transmission frequencies for the two orthogonal polarizations indicated by a 45 degree difference in HWP setting. (c) Schematic of the double-pass configuration, using a Thorlabs PBS121 PBS, Foctek WPC212H HWP, and Foctek WPC212Q QWP.